Generation, Detection and Characterization of Photonic Quantum States

a Ph.D. thesis

by

Ivo Straka

Faculty of Science | Palacký University

Olomouc
2019

Abstract

This dissertation experimentally explores quantum properties of photonic states. The presented results compare quantum non-Gaussian properties of single-photon states produced by optical frequency conversion and radiative recombination in a quantum dot. The primary concern is resilience against optical loss that is inevitable in all real applications. Quantum non-Gaussianity is also measured using multiphoton states composed of multiple heralded single photons generated by frequency conversion. Another quantum property is genuine n-photon quantum non-Gaussianity, which is investigated using multiphoton states with respect to optical loss and added noise.

Furthermore, the thesis presents a method of programmable intensity modulation as a source of arbitrary classical photon statistics. The method includes calculation of the respective intensity distribution.

The procedures employed in the thesis include constructing a source of correlated photons based on frequency down-conversion. The source was used to obtain the results pertaining to multiphoton quantum non-Gaussianity. Next, a counting model of single-photon avalanche diodes is developed, both analytically and in simulation. These results were used in measuring arbitrary photon statistics.

Keywords: quantum optics, photon statistics, quantum non-Gaussianity

Title:	Generation, Detection and Characterization of Photonic Quantum States
Author:	Mgr. Ivo Straka
ORCID:	0000-0003-2675-6335
ResearcherID:	V-2610-2017
Advisor:	prof. Mgr. Jaromír Fiurášek, Ph.D.
Consultant:	RNDr. Miroslav Ježek, Ph.D.
Ph.D. programme:	Optics and Optoelectronics (full-time form)
Institution:	Department of Optics, Faculty of Science, Palacký University
Year:	2019
Pages:	96

Příprava, detekce a charakterizace kvantových stavů světla

disertační práce

Ivo Straka

Přírodovědecká fakulta
Univerzita Palackého

Olomouc
2019

Anotace

Cílem této práce je experimentální výzkum statistických vlastností kvantových stavů světla z hlediska generace i měření. Práce uvádí výsledky srovnávající kvantově negaussovské vlastnosti jednofotonových stavů produkovaných optickou frekvenční konverzí a zářivou rekombinací v kvantové tečce. Klíčovou vlastností je odolnost vůči ztrátám, jež jsou nevyhnutelnou součástí reálných optických aplikací. Kvantová negaussovskost je měřena i pro vícefotonové stavy složené z hlášených jednotlivých fotonů generovaných frekvenční konverzí. Jako další vlastnost je u těchto stavů zkoumána vícefotonová ryzí negaussovskost s ohledem na ztráty a přidaný šum.

Disertace dále uvádí metodu programovatelné intenzitní modulace jako zdroje světla s nastavitelným klasickým rozdělením počtu fotonů. Součástí je i výpočet odpovídajícího intenzitního rozdělení.

Postupy využité v práci zahrnují konstrukci zdroje korelovaných fotonů na bázi sestupné frekvenční konverze, jenž umožnil dosažení výsledků v oblasti vícefotonové kvantové negaussovskosti. Dále je prezentován model čítací odezvy jednofotonových lavinových diod, a to v numerické simulaci i analyticky. Tento výsledek byl uplatněn při měření obecné fotonové statistiky.

Klíčová slova: kvantová optika, statistika fotonů, kvantová negaussovskost

Název:	Příprava, detekce a charakterizace kvantových stavů světla
Autor:	Mgr. Ivo Straka
ORCID:	0000-0003-2675-6335
ResearcherID:	V-2610-2017
Školitel:	prof. Mgr. Jaromír Fiurášek, Ph.D.
Konzultant:	RNDr. Miroslav Ježek, Ph.D.
Studijní obor:	Optika a optoelektronika (prezenční forma)
Instituce:	Katedra optiky, Přírodovědecká fakulta, Univerzita Palackého
Rok:	2019
Počet stran:	96

Acknowledgements

I thank Miroslav Ježek for his invaluable mentoring, ideas, diligence, and for all his hard work put into the Quantum Optics Lab, its projects and its team. Without him, this thesis would never have been written. I am also grateful to Jaromír Fiurášek for his guidance and constant support during my studies. I thank Radim Filip for his ideas, discussions and for our common projects. I am thankful to the whole QOLO team for their help and for maintaining a friendly and open atmosphere; with special thanks to Martina Miková/Nováková for her unceasing assistance, support, and nourishment. I am grateful to all my senior colleagues in the department for their hard work and making sure that the possibilities the students have are constantly growing. I thank all the collaborators I have not yet named with special thanks to Ana Predojević for her work on onions, Quantera, and for keeping it real. I thank our administrative team for making everything work. I am especially grateful to all my friends I met at the department for their company and I thank the Derkach family for being so awesome. My special thanks belong to my friends the musicians and to the Lindy community who have kept me sane all these years and always relieved me of the work-related stress and guilt. A very special thanks goes to my family, to whom I owe more than I could say here.

Contents

Preface

This thesis is the result of my post-graduate studies at the Department of Optics, Faculty of Science, Palacký University. Its aim is to present new advances in witnessing quantum properties of light and generating arbitrary classical photon statistics. The thesis is based on four publications denoted in References under A1, A2, A3, and A4. The first three have been peer-reviewed and published, while the last one is under peer review at the time of writing. Here I aim to explain my involvement and contribution to the presented work.

The experimental research into quantum non-Gaussianity began during my master's studies under the supervision of Miroslav Ježek.[1] The subject of the thesis was building a down-conversion source, which was incidentally used to measure the data for the publication 2.

The research continued during the first year of my post-graduate studies under Miroslav, when I visited the group of professor Gregor Weihs. In the mutual collaboration of the theoreticians and experimentalists of our department in Olomouc, professor Weihs' group in Innsbruck and professor Glenn Solomon in Gaithersburg, quantum non-Gaussianity of multiple single-photon sources was evaluated.[A1] I was responsible for measuring the continuous-wave down-conversion data and during my stay in Innsbruck, I worked with Lorenz Butschek to measure the pulsed down-conversion data. I was also responsible for writing the appropriate parts, synthesis of the results, editing the manuscript and the submission process.

The project that followed is not included in this thesis. It was focused on bipartite entanglement localisation with respect to the temperature of an incoherent environment (I. Straka, M. Miková, M. Mičuda, M. Dušek, M. Ježek, R. Filip, Sci. Rep. 5, 16721, year 2015).

Lukáš Lachman and Radim Filip then developed a hierarchy of quantum non-Gaussian criteria that we experimentally tested on a new down-conversion source.[A2] My task was to construct the source, perform the measurement and process the data. I was also responsible for writing the appropriate parts, editing the manuscript and handling all submissions. The results are considered theoretical and experimental by equal part, with Lukáš and I being the graduate students

chiefly responsible for the respective parts.

The last work on genuine quantum non-Gaussianity utilized the same multichannel measurement scheme as the previous project.[A4] My contribution again concerned the source, measurement, data processing and writing the experimental part, while editing and submission of the manuscript was the responsibility of Lukáš.

The last presented project started as an idea of Miroslav Ježek that was developed by Jaromír Mika in his bachelor's and master's thesis under my supervision.[3] Afterwards, Miroslav and I continued the work to produce a publication.[A3] I was responsible for building the setup, developing the numerical and driving methods, formulating the detection model and calibrating the detectors, measuring and processing the data, and writing the chief part of the manuscript.

All of the presented work was supervised by Miroslav Ježek, who has been closely involved in all experimental and technical work, analyses of the data, discussions and writing. I feel that his invaluable work and close involvement with my contributions should be acknowledged here as well.

When writing the thesis, I focused on discussing my own results and the relevant principles; perhaps at the expense of a comprehensive theoretical introduction. There are, however, several textbooks cited for the reader to refer to, and where appropriate, articles that contain the necessary material. Therefore, known principles are rather stated and cited than explicitly derived. In Chapter 3 where the theoretical apparatus was derived by my colleagues—some of whom will doubtlessly be including their work in their own dissertation—I reduced the theory to a minimal explanation. I would refer any reader interested in the theory of quantum non-Gaussianity to the relevant publications.

At the time of writing I can be contacted via the electronic addresses below. I welcome any feedback or questions that the reader may have; if only for the joy of someone reading my thesis.

Olomouc
March 2019

Ivo Straka
ivo.straka@gmail.com
straka@optics.upol.cz

Chapter 1

Introduction

Photons are considered as particles of light, because they represent excitation quanta of the electromagnetic field. Generating particular quantum states that contain only one or several photons is needed for quantum computing, cryptography and metrology. The subject of current experimental research therefore includes both generation and detection of such states. This thesis presents advances in recognizing their quantum properties and in manipulating the photon statistics to match a predefined distribution.

First, methodological details are presented in Chapter 2. Section 2.1 elaborates on the parametric down-conversion technique of generating single photons and photon pairs. Section 2.2 describes the experimental realization of such a photonic source. Section 2.3 provides the description of single-photon avalanche diodes that are used as detectors. Their detailed description is needed particularly for verifying custom-generated photon statistics. Subsections 2.3.2 to 2.3.4 offer original results that address modelling the detectors' response to photon statistics. Finally, section 2.4 elaborates on some mathematical procedures that are used in the main chapters and require further discussion.

In Chapter 3, new methods are proposed that can recognize quantum non-Gaussian light. These detection methods utilize a measurement on a multiplexed detector that is able to distinguish the number of photons. Quantum non-Gaussianity (QNG) is a fundamental property of certain states of light that is only present in quantum physics. The most notable states that possess this property are the Fock states. These are energy eigenstates that contain a fixed number of photons. They represent essential resources for quantum optical protocols and recognizing the properties that are necessary for their existence is an important tool for the development of photon sources.

Section 3.2 focuses on single photons.[A1] A QNG depth is proposed to quantify the loss resilience of QNG. Multiple single-photon sources are measured and compared in a signal-noise space with an emphasis on tolerable optical attenuation.

Section 3.3 tests a new way of recognizing QNG that is optimized for multiphoton states.[A2] Using a heralded single-photon source based on parametric down-conversion, a multimode state containing several heralded photons is prepared. The results prove the QNG character of 1–9 heralded photons despite unfavourable optical loss and systematic noise.

Section 3.4 introduces a more specialized quantum property called *genuine* quantum non-Gaussianity that imposes even stricter criteria than QNG.[A4] Again, this property is demonstrated on a multimode state of 1–3 heralded photons.

Chapter 4 practically treats the problem of generating arbitrary photon statistics.[A3] Within the semi-classical view of the Mandel formula, the results demonstrate a very accurate generation of photon statistics that was defined by the user. The proposed generator is capable of preparing highly bunched light and statistics on an exceptionally wide range of photon numbers.

1.1 The context of the presented research

Photon-number states and their properties

Generating a definite number of photons and Fock states of light is essential for quantum information processing and quantum state engineering. Single-photon states are often required for photonic quantum computation, where they serve as information carriers or ancillas.[4] However, not only single-mode Fock states are important. With multiple separate photons, quantum entanglement can be harnessed in a number of protocols.[5] Two or more photons allow distributing the entanglement among multiple parties for the purposes of teleportation[6,7] or quantum cryptography.[8,9] The distribution may be aided by quantum repeaters that rely on multiple well-entangled photon pairs to distribute entanglement over distance.[10] The Fock states can be used to create superpositions of several photons called NOON states.[11] These states represent a step towards macroscopic superposition of multi-particle ensembles; they also enhance phase interferometric sensitivity.[12]

Experimental generation of Fock states still faces practical challenges.[13–15] They can be roughly summarized as purity and efficiency. The ideal source would generate the states deterministically and on demand. The main problem is optical transmission of the whole process, which may cause some photons to be lost randomly. For some sources, the limitation is mainly in the optical setup,[15] for others that collect radiation from a microscopic source, the main challenge is collection efficiency.[16] The purity means an overlap of the generated state with the corresponding ideal Fock state. To some degree, efficiency has an effect on purity, because optical loss shifts the photon-number probabilities to lower num-

bers. This is not a significant problem for those protocols that allow selecting only cases with a minimum number of detected photons.[4] The major issue with purity is extra noise. Especially single photon applications suffer with increasing multiphoton content; such as discrete-variable quantum cryptography[17] or quantum computing, where it introduces errors.[18] Both efficiency and purity affect the experimentally available Fock states in a non-trivial way. The deviation from an ideal state can be expressed by the reconstructed Wigner function or by measuring the photon-number statistics.[14]

The Fock states also possess certain fundamental quantum properties that can be experimentally observed. These properties include nonclassicality,[19,20] Wigner function negativity[21] and quantum non-Gaussian characteristics. The last property (QNG) is the focus of Chapter 3. It was formulated by Filip and Mišta as an extension of nonclassicality toward Gaussian mixtures.[22] Experimental observations followed for a down-converted single-photon state,[1,2] photon-subtracted squeezed vacuum,[23] single photons from a quantum dot,[24] and up-converted single photons.[25] QNG can be witnessed by estimation of photon-number probabilities using a Hanbury-Brown-Twiss setup.[2,26] Other proposed witnesses utilize phase-space variables.[27–29] This thesis reports on experimental QNG witnessing using a multichannel detector, which better suits multiphoton states.[A2,30] Additionally, the same technique is used to recognize *genuine* n-photon QNG, which is a generalization excluding Gaussian mixtures of lesser Fock states.[A4]

Among Fock states, single photons represent a prominent resource for quantum technology. There are various physical systems that can generate single photons. Two main principles are observed: generation of photon pairs and single-photon emission. Photon pairs rely on using one particle to herald the presence of the other. They can arise in nonlinear interaction processes such as down-conversion[31] or four-wave mixing.[32] Fast cascaded decays of electron excitations may also result in emitting a closely correlated photon pairs. These decays may be akin to four-wave mixing[33] or originate from electron-hole recombination[34] that may be tailored to achieve entanglement.[35] Single-photon emission is achieved by isolating only one particle that is physically allowed to emit only one photon at a time. These particles include excitons in semiconductor quantum dots,[36] crystal colour centres,[37] trapped ions,[38] and single molecules.[39]

Down-conversion

This thesis employs methods of generating correlated photon pairs using spontaneous parametric down-conversion (SPDC). It was first observed in a bulk nonlinear crystal as parametric fluorescence by Harris and colleagues in 1967.[40] Photon pairs produced by SPDC were shown to interfere by Hong, Ou and Mandel in the key article from 1987.[41] Such sources gained prominence in the nineties as

efficient generators of polarization-entangled photons.[42,43] Subsequently, periodically poled crystals were used to harness stronger nonlinearity and yield higher brightness.[44,45] Coupled with an interferometric Sagnac scheme, entangled photon pairs could be produced with superior brightness.[46,47] Periodically poled nonlinear waveguides offer significantly higher gain than bulk crystals, but their down-converted spectra contain side-peaks of other guided modes.[48]

SPDC can be used for generating spectrally entangled photons.[49] The spectra can be made uncorrelated[50,51] or even positively correlated.[52,53] An important factor is the pump; the sources are generally operated in either continuous-wave (cw) or pulsed regime. Pulsed pump enables producing single-mode states, as their temporal width is typically narrower than detector resolution, but the down-converted two-mode spectra are broader and photon indistinguishability needs to be controlled.[54] Since all pump power is concentrated into the pulses, the multiphoton contributions are higher than for the corresponding cw pump (discussed in section 3.2.6). Broome and colleagues showed that multiplexing the pump pulses leads to better signal-to-noise ratio that does not reduce the generation rate so much as decreasing the pump power.[55] Mendoza and colleagues demonstrated that pulsed sources can be actively switched to increase the single-photon probability.[56]

Classical photon statistics

For classical light, photon statistics is based on a semi-classical model formulated by Mandel.[B1,57] It considers the probability density of photon occurrence proportional to the intensity of light. Using this principle, one can stochastically modulate optical intensity to obtain the corresponding photon statistics.[58]

Classical light, namely coherent states, have been used in quantum science as well, for instance to simulate quantum walks[59] or to calibrate the response of photon-number-resolving detectors.[60–62] Light that exhibits photon bunching was shown to have several uses. Thermal light of a laser below threshold was shown to improve the efficiency of second-harmonic light generation;[63] superbunched light was produced to a similar effect.[64] Two-photon absorption can also be enhanced by bunched light.[65] Thermal light was shown to increase interferometric phase resolution after subtracting one photon[66] and enable observation of sub-wavelength interference fringes.[67] It can aid photon-number resolution when used as a probe.[68] Bunched light can be also used for ghost imaging[69] – a protocol enabling the imaging of an object by a non-resolving 'bucket' detector if an imaging detector is applied on a second beam. The correlations between the two beams can be produced either by quantum entanglement or photon-number correlations (bunching).[70] Superthermal or superbunched light has been investigated for its heavy-tailed statistical properties that manifest as rare high-intensity

phenomena.[71,72]

The conventional method to generate pseudo-thermal light is to use a rotating glass disk.[73] This approach was used in some of the work already mentioned.[66–68] It is used for ghost imaging techniques as well.[74,75] By using multiple disks, photon superbunching can be generated.[76–78] Other methods of generating bunched light include interference in multi-mode fibres[79] or disordered lattices.[80,81]

Classical photon statistics is derived from the stochastic nature of light intensity by means of an integral transform.[B1] The inverse problem is ill-posed mainly because of the classicality condition, but there have been a few methods published on its solution. In 1967, Bédard formulated a series of Laguerre polynomials that mathematically invert Mandel's formula.[82] However, a finite expansion of the series suffers from negativity and the overall convergence may be rather slow. Consequently, approximative methods have been devised to obtain the intensity distribution. Byrne and colleagues published an algorithm working with a prior basis in intensity distributions[83] and later also proposed expectation-maximization as a solution for discrete compound Poisson cases.[84] Earnshaw and Haughey proposed a least-squares fit of cubic splines to match the photon-number distribution.[85]

The problem of Mandel's formula inversion in this thesis is aimed experimentally. Since only discrete intensities are available and known beforehand, solution proposed in reference 85 could be used. However, such case is essentially a linear-equations-set fit. If a strictly zero residual is required, then a simple least-squares fit is sufficient (section 4.2). This requirement is chosen because the source photon-number distribution is not represented by a finite set of measured counts as in reference 85, but accurately specified by the user.

Single-photon detectors

To recognize photon statistics—either by counting photons or by witnessing nonclassical properties—adequate means of detection are required. Lately, detectors operating at cryogenic temperatures have become more available.[B2] These include superconducting nanowires that feature better parameters than SPADs,[86] but due to the cryogenics they typically require investment that is higher by an order of magnitude. Transition-edge sensors is another technique that utilizes the resistance transition curve at the edge of material superconductivity to measure the number of incident photons. While these sensors possess photon-number resolution, they suffer from cross-talk and easier saturation.[B2,86]

Although cryogenic detection represents the current cutting edge in many regards, this thesis utilizes single-photon avalanche diodes (SPADs)[B3] that are more common and affordable. The characterization and optimization of their

behaviour is still a subject of ongoing research. Parameters like detection efficiency[87,88] and afterpulsing[89,90] require careful calibration. Analytical representations of afterpulsing are approximate and based on different decay models, assuming a series of exponentials[91] or a modification with hyperbolic sine.[92] Recent work even challenged the general assumption that the temporal distribution of afterpulses only depends on the time of the last detection.[93,94] There have been efforts optimizing the quenching circuit to reduce afterpulsing altogether; or focusing on performance in cryptography.[95,96] Even though SPADs do not possess photon-number resolution, they can be used for that purpose in multiplexed schemes: silicon photomultipliers,[97,98] temporal multiplexing[99–101] or spatial multiplexing.[102]

This thesis utilizes photon counting by a single SPAD to reach very high dynamic ranges that would be otherwise unattainable. The necessary model of the SPAD response generalizes both current Monte-Carlo[103] and analytical approaches. The currently accepted theoretical counting models (equation (7.13) in reference B3, reference 104) are approximative and consider a perfect detector with a dead time. The exact mathematical model of a dead-time-influenced detector was derived by Müller in 1973.[105] This thesis introduces an analytical generalization in section 2.3.3 that includes afterpulsing.

Chapter 2

Methods

2.1 Spontaneous parametric down-conversion (SPDC)

The work on quantum non-Gaussianity presented in Chapter 3 is experimentally based on heralded sources of single photons. The source that is the subject of this thesis is based on frequency conversion of light in a nonlinear crystal. This section briefly summarizes the important physical aspects of SPDC and their significance for constructing an SPDC source. Full theoretical treatment can be found in the supplied references.

2.1.1 Main principles

Frequency down-conversion is a phenomenon in nonlinear optics where a light signal propagating through an optically nonlinear environment becomes coupled with other modes of light that have lower frequencies.[B1,B3] A spontaneous parametric process assumes a strong beam (pump) entering the environment, while the other modes begin in a vacuum state. After the interaction, these modes become weakly excited and mutually entangled.

In this work, a particular collinear degenerate type-II scheme is used, where three waves interact in a nonlinear anisotropic crystal. In uniaxial crystals, the polarization eigenmodes correspond to extraordinary and ordinary polarizations determined by the direction of the crystal axis; in biaxial crystals, the terms can be used by convention, as technically all waves are extraordinary.

The pump is set to extraordinary linear polarization and two weak beams of light are down-converted, commonly referred to as signal and idler. One has ordinary, the other extraordinary polarization, while their spectra and spatial

modes are entangled. The signal that is collected is collinear with the propagation of the pump and is spectrally degenerate; each beam is of half the pump frequency. The practical meaning of this process is that photons in both beams are tightly correlated in time, and can be therefore used as a source of photon pairs – or a source of heralded single photons.

The physical aspects of SPDC in their full breadth are quite complex, so it is necessary to understand them and eliminate unnecessary considerations when designing an SPDC source. The main problem is called phase matching, which is commonly understood as a condition on wave vectors of all planar waves involved in the frequency conversion. It involves the properties of the light as well as of the crystal. Since the pump is neither monochromatic nor a planar wave, and since the crystal is anisotropic, the down-converted radiation exhibits a complex structure.

2.1.2 Interaction of three waves

SPDC is a process akin to difference-frequency generation or parametric amplification in classical nonlinear optics.[B4] However, classical differential equations for down-converted wave amplitudes require that at least one of the fields has non-zero amplitude at the beginning. In SPDC, both amplitudes are zero; only the pump signal enters the nonlinear medium. Therefore a quantum optical treatment of frequency conversion is necessary.

The quantum picture is obtained by writing down a classical energy-density Hamiltonian of three waves in a quadratic medium using quantum field operators.[B1,106] The approximation of a strong pump beam is used, which safely neglects any depletion of the pump. The nonlinear susceptibility tensor $\chi^{(2)}$ gives rise to an interaction term in the Hamiltonian that covers all possible modes of light, particularly in terms of wavelength, spatial and polarization modes. This Hamiltonian is then applied via an evolution of the initial state, which contains only the pump signal of angular frequency ω_0. The evolution gives rise to two modes of radiation, each comprising of a complex superposition of frequency, planar-wave and polarization eigenmodes.[106] Each mode exhibits Bose-Einstein statistics of photons due to full expansion of the evolution operator and the creation operator terms present in the interaction Hamiltonian.

Approximately, the polarization eigenmodes of all planar-wave components are equal to polarization eigenmodes of the crystal in the direction of the pump. Therefore, down-converted modes have mutually orthogonal linear polarizations. The state can be further approximated by assuming a weak interaction factor and considering only the first two terms, which is sufficient in the case of continuous-wave pump. In the basis of Fock states of planar waves parametrized by

wavevectors $\mathbf{k}_1$ and $\mathbf{k}_2$ inside the nonlinear medium, the down-converted state is (leaving out the strong pump)

$$|\text{SPDC}\rangle \approx |\text{vac.}\rangle + \iint_{\mathbf{k}_1,\mathbf{k}_2} \Psi(\mathbf{k}_1,\mathbf{k}_2) a^\dagger_{\mathbf{k}_1} a^\dagger_{\mathbf{k}_2} |\text{vac.}\rangle\,. \tag{2.1}$$

The complex amplitude Ψ, sometimes called gain, is a function of wavevectors and thus depends on the optical frequency, on the direction of propagation and on the index of refraction of each wave. This gives rise to so-called *phase-matching* conditions that determine the properties of down-converted waves. The conditions can be simplified to

$$\omega_0 = \omega_1 + \omega_2, \tag{2.2}$$
$$\mathbf{k}_0 = \mathbf{k}_1 + \mathbf{k}_2. \tag{2.3}$$

Equation (2.2) binds the frequencies of the generated waves assuming a monochromatic pump of frequency ω_0 and long interaction time. Equation (2.3) assumes a planar wave in an infinite medium and it binds the directions of the waves with respect to refractive indices and respective frequencies.

These simple conditions are usually used to find basic experimental conditions for a successful down-conversion. For example, one may specify the desired central wavelengths of all three waves in accordance with (2.2), postulate the direction of all waves and seek the set of refractive indices that would allow such generation. Alternatively, the indices may be fixed and one obtains the spatial profile of a signal given specific wavelengths. The means of phase matching include temperature tuning of refractive indices,[40] using birefringence by tilting the medium,[107] or collecting light in particular directions.[42]

The first step to a more detailed analysis is usually the assumption of a finite thickness L of the nonlinear medium, which makes the gain proportional to

$$\Psi \propto \frac{\sin\left(\frac{1}{2}\Delta k\, L\right)}{\frac{1}{2}\Delta k\, L}, \tag{2.4}$$

where $\Delta k = (\mathbf{k}_0 - \mathbf{k}_1 - \mathbf{k}_2) \cdot \mathbf{n}_a$ is a projection of the wavevector mismatch onto the direction of the optical axis $\mathbf{n}_a$ (assuming the other projections are zero).[106] This is usually needed for spectral analyses, such as calculating the emitted bimodal spectrum or optimizing the thickness L with respect to the spectrum of the pump.

An approach that calculates the Hamiltonian using Gaussian beams reveals that SPDC gain may be maximized using focusing, which was first indirectly shown by Boyd and Kleinman,[108] and subsequently generalized by Bennink.[109]

2.1.3 Quasi-phase-matching in a periodically poled medium

Periodically poled materials solve the problem of optimally utilizing the nonlinearity of a medium. The SPDC gain is proportional to the product of the second-order susceptibility tensor $\chi^{(2)}$ and the interacting waves. As a tensor product, this quantity varies with the orientation of the medium relative to the configuration of the waves and their polarizations. However, due to the first-order susceptibility tensor $\chi^{(1)}$, the phase mismatch Δk varies as well, which limits the gain optimization. Periodically poled materials offer effective elimination of Δk; thus giving freedom to optimize the effective nonlinearity. The nonlinear medium contributes to the amplitude of the down-converted modes (2.1) with a phase-oscillating term $e^{i\Delta k\, z}$, where the coordinate z integrates through the medium. This results in the top term in (2.4), which oscillates more rapidly as Δk grows. Imagining the waves entering the medium with an initial phase difference of zero, the nonlinear contribution is amplified between $z = 0$ and $z = \pi/\Delta k$ and then reduced until $z = 2\pi/\Delta k$; and so on. This behavior may be altered by introducing a phase flip of π to the contributing term periodically so that the amplitude keeps increasing.[110] A nonlinear susceptibility inversion that introduces the phase flip can be achieved by applying external voltage on periodic domains.[111] From the relations above follows that the spatial poling period Λ must satisfy $\Delta k - 2\pi/\Lambda = 0$, which gives rise to an additional phase-matching term. This method is referred to as quasi-phase-matching and is used for the SPDC source used in section 3.3 and described in the section 2.2.

2.1.4 Some considerations when designing an SPDC source

The pump laser represents the primary factor of an SPDC design. Nonlinearity, dispersion and absorption are spectrally dependent, so the central wavelength itself and the wavelengths of down-converted waves influence the choice of the material. The pump spectrum then determines the optimal thickness (or length) of the crystal.

Suppose that for a central pump frequency ω_0, phase-matching is fulfilled and $\Delta k = 0$. For other frequencies in the pump spectrum, Δk becomes nonzero and the sinc-dependence (2.4) lowers the efficiency of down-conversion. That means the pump frequency range, for which SPDC takes place, is limited and determined by the crystal length L. If the pump power is spectrally distributed outside of such range, the effective power taking part in the conversion is lower.

On the other hand, increasing crystal length also increases SPDC brightness – for interacting Gaussian beams, the power $|\Psi|^2$ grows linearly with L.[109] The crystal length that yields the most photon pairs per second is therefore dependent on the spectral width of the pump. For narrow-band continuous-wave lasers, long crystals such as >10 mm may be used, whereas for pulsed pumping, shorter crystals are needed.

Birefringent walk-off is another factor that is present mainly in angular phase-matching. In such cases, the waves usually do not propagate along any principal crystal axis. As a result, the energy of extraordinarily polarized waves flows in a different direction than their wavevectors. Particularly, in a collinear type-II process, the pump is e-polarized, but one of the down-converted modes is o-polarized. This leads to a convolution of the transversal beam profile and reduces the subsequent efficiency of single-mode coupling.[1] This effect is also proportional to crystal length, but it reduces collection efficiency rather than generation rate.

2.2 SPDC source of photon pairs

This SPDC source was used in the experiments described in section 3.3 and published in references A2 and A4. Moving this source to a mobile breadboard, including reassembling and alignment, was the subject of a bachelor's thesis by M. Neset.[112]

2.2.1 Phase-matching and crystal configuration

The source is based on collinear type-II down-conversion in a periodically poled $KTiOPO_4$ crystal (ppKTP). The crystal is 6 mm thick and comprises of three poling domains, each approximately 1×1 mm wide. The poling periods are 9.900, 10.000, and 10.075 μm. The middle domain is used, as it offers optimal temperature tuning for the pump at 405 nm.

The configuration is shown in Figure 2.1. Light propagates along the x-axis and the pump is vertically polarized (along the y-axis). The phase-matching calculations were published by Fedrizzi and colleagues for a Sagnac configuration[47] and require Sellmeier equations for KTP[113] and thermal dispersive coefficients.[114,115]

The optimal crystal temperature was observed to be around 30.0 ℃, although the calculations predict a value 48.7 ℃ based on a vacuum wavelength of the pump 404.99 nm. This could be caused by a different poling period having been manufactured. Preliminary measurements were made to determine which poling

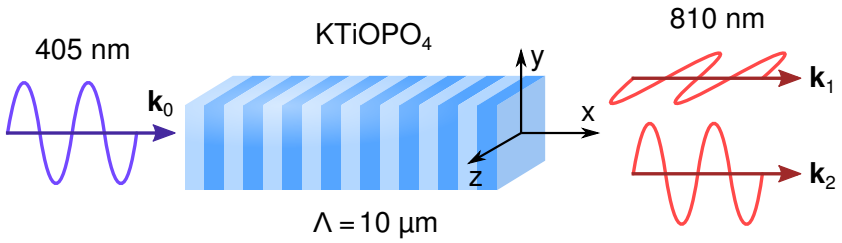

Figure 2.1: Down-conversion scheme showing crystallographic axes, polarizations and wavelengths. Only one poling domain of the crystal is shown.

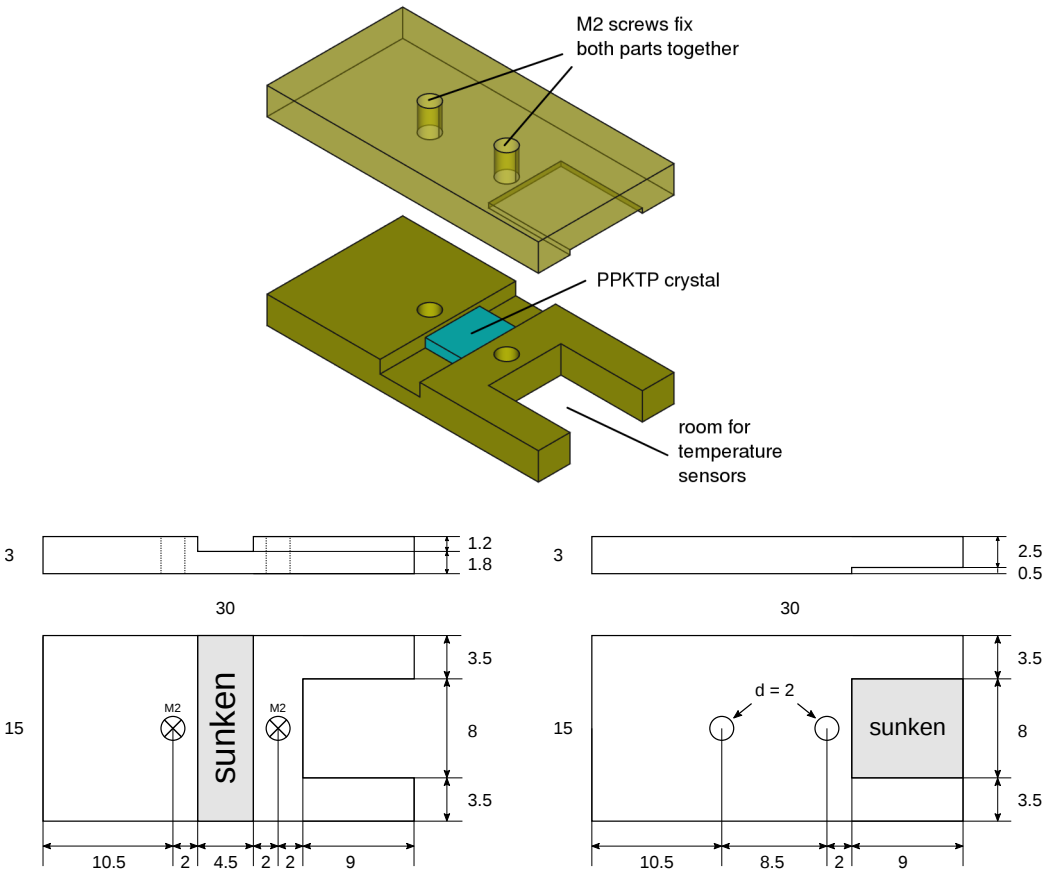

Figure 2.2: Brass crystal housing. The top image shows an orthographic projection of both parts; the lower schematics show side and top views of both parts with specified dimensions.

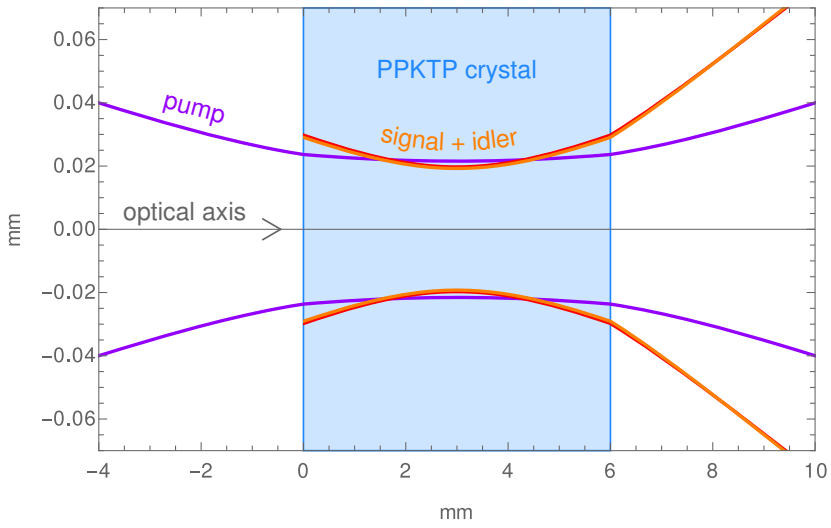

Figure 2.3: Gaussian beam widths are plotted for all beams interacting in the crystal. The pump profile is based on the lenses before the crystal. Signal and idler profiles represent the optimal modes to be coupled with maximum efficiency.[109] Both dimensions are in millimetres, but are not drawn to scale; the beam divergences appear much larger than in reality. The crystal is positioned between 0 and 6 mm marks. Note that signal (red) and idler (orange) beams slightly differ due to different indices of refraction. The respective waist diameters of the pump, signal and idler are 43 µm, 39 µm, 38 µm, and the respective angular spreads outside of the crystal are 12 mrad, 26 mrad, 27 mrad.

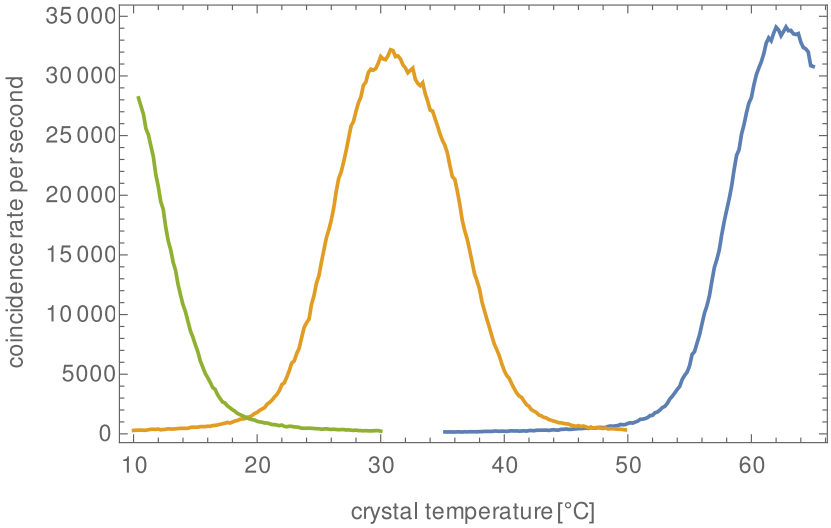

Figure 2.4: The dependence of detected pair rate at 810 nm on crystal temperature. Three poling domains are shown for the same pump wavelength. Estimated optima are at 7 ℃, 31 ℃, 63 ℃. The shapes of the curves depend on the spectral transmission of the band-pass filter that was used (see section 2.2.2).

domain should be used (see Figure 2.4). Although the data were not obtained using an optimally aligned optical setup, the temperature dependence clearly distinguishes three different poling periods. Ideally, the dependence should be approximately squared-sinc-shaped, because Δk depends approximately linearly on small changes in temperature and equation (2.4) holds. The main reason why the curves in Figure 2.4 look different is that the the collected photons are not monochromatic and their spectra depend on the band-pass filter that is used. Therefore the resulting pair rate is a product of the biphoton spectrum and the spectral profile of the band-pass filter.

The next step in phase-matching calculations includes focusing of the interacting beams. As all modes are coupled from/to single-mode step-index fibres, the beams may be considered approximately Gaussian. The methodology published by Bennink[109] works with focal parameters of the beams, which are defined $\xi = \frac{L}{kw^2}$ with L being the crystal length, k the wavenumber and w the Gaussian waist radius inside the crystal. The optimal value is $\xi = 2.84$ for all beams, which means that the spot size of the pump inside the crystal would be 17.2 µm. In the presented source, a 100-mm lens focuses the pump into an estimated spot of 43 µm, which reduces the peak spectral brightness to approximately 65 % of the theoretical maximum. This does not pose a significant restriction, because the overall gain with respect to pumping laser power is still high. Moreover, stronger focusing using conventional lenses increases spherical aberration, which reduces the overlap of the beams. So, the theoretical maximum would not be reachable in reality. The optimal focusing would require a 30-mm lens, which would also place the focusing and collimating lens too close to the crystal. For practical reasons, a weaker focusing was chosen in the presented source. The interacting beam profiles are shown in Figure 2.3.

The crystal dimensions are 1×4×6 mm and it needs to be maintained at the phase-matching temperature by a Peltier module. The brass housing for the crystal is shown in Figure 2.2. The top and side gaps between the crystal and the housing are filled with stripes of a thermally conductive sheet. Both faces of the crystal are sunken in the housing groove, which prevents dust deposition. That needs to be prevented because the focused pump power density is quite high in the crystal; dust particles could be scorched and stuck onto the faces, obstructing the beams.

The bottom part of the housing contains a cut-out part where thermal sensors are attached using a thermally conductive glue. One of the sensors is a thermistor that is used for temperature stabilization in a PID loop. It has a fast response, but its absolute accuracy is only about 0.5 K. The other sensor is a platinum thermometer that has a considerably slower response, but is calibrated more precisely.

Both parts of the housing are then screwed together and glued on a 30×15-

mm Peltier module. This system is placed on a tip-tilt and translation stages that allow precise adjustment of the angle of incidence, transversal positioning, and beam waist location inside the crystal. The Peltier current is controlled by a proportional-integral-derivative (PID) stabilization unit TED4015 manufactured by Thorlabs. The PID loop parameters were set to $P = 0.250$ A/K, $I = 0.100$ As/K, $D = 0.170$ A/Ks, osc. period = 7 s.

2.2.2 Components and setup

The pump is provided by a frequency-stabilized diode laser (Ondax SureLock LM405) operating at 405 nm. The laser features frequency stabilization using volume holographic grating with a specified linewidth of 160 MHz and wavelength stability of 1 pm. The output is a linearly polarized beam with an elliptical transversal profile.

The pump is delivered into the SPDC source through a single-mode optical fibre. This provides excellent repeatability in case the laser needs to be replaced. In such a case, one would only need to couple the new laser into the fibre and the SPDC source itself would require no realignment.

The coupling involves some beam shaping to achieve reasonable coupling efficiency. The setup is shown in Figure 2.5. In theory, beam ellipticity is compensated by a pair of cylindrical lenses. The setup uses only one cylindrical lens and a subsequent expander consisting of spherical lenses, which gives sufficient results. The laser might be damaged if any reflected light enters its cavity; for that purpose, a Faraday isolator (Qioptiq FI-405-55V) is present that attenuates any reflected light by 27 dB.

To maintain performance stability, the pump laser diode is operated at 70 mA driving current. Pump power is adjusted using a rotational attenuator that reflects a portion of the pump into a wavemeter (Moglabs Mogwave) that monitors the spectrum with a 12-pm resolution. As the expected linewidth is much narrower than the response of the wavemeter, the main information obtained is the central wavelength. The laser exhibits modes that are separated in wavelength by approximately 30 pm and operate within about 1 ℃of laser diode temperature. This temperature range shifts significantly in the order of hours and so the temperature needs to be occasionally adjusted between 21–23 ℃ to maintain single-mode emission.

The wavemeter was calibrated by a mercury lamp. The reported vacuum wavelength for the spectral line of 404.770 nm[116] was 404.752 nm. Assuming a constant calibration error for any laboratory temperature, atmospheric pressure, or close wavelengths, the pump vacuum wavelength is estimated to be 404.99 nm. Apart from mode hopping, any observed drift of the central wavelength is

smaller than the accuracy of the wavemeter.

The schematic of the SPDC source and its basic description are shown in Figure 2.6. Apart from the pump, a probing signal at 810 nm is used for aligning the components. Initially, both beams are mixed and aligned using a dichroic mirror and two irises. The fibre couplers are put in a tilting mount like the mirrors, which grants all the necessary degrees of freedom. The pump beam must be collimated to match the waist size and position in the crystal. Then, the HWP, lenses and the crystal are put in the optical path. They do not need to be tilted too much with respect to the beam, because there is very little chance the reflection would be coupled back into the single-mode fibre. The approximate longitudinal positions of the lenses and the crystal with respect to each other need to be calculated. In principle, the position of the crystal may be optimized by beam width measurements of the pump, but the position of the collimating lens depends entirely on the generated signal and cannot be precisely aligned beforehand.

The main portion of the pump is cut off by a reflective filter placed immediately after the crystal so that the pump light is not scattered by the coating of the collimating lens (Semrock BLP01-635-25, optical density OD6). The tilt of the filter should not be too great, but enough for the reflected beam to go back through the crystal and be blocked by the coupler mount.

To assemble the rest of the setup, the probe beam is used. If the lenses are centred on the optical axis and the crystal is not too tilted, the probe beam should be very close to the generated signal. As a kick-start measure, multi-mode fibres may be used on the coupling end to find the down-converted signal more easily. In this case, it is best to screw on cut-off filters on the couplers to filter out background light from the laboratory.

After collimation, it is necessary to introduce further spectral filtering. The residual strong pump could be coupled in the fibres along with the signal, so another OD6 filter is used. A band-pass filter is also used to ensure spectrally degenerate operation and proper spectral tuning of the probe (Semrock LL01-810-12.5, 3 nm bandwidth).

The PBS (Melles Griot) transmits horizontal polarization and reflects vertical. It is optimized for s-polarization reflectivity, which means the extinction ratios are 40 dB in the transmitted port and 18 dB in the reflected port. A HWP and an additional PBS in the reflected port are sometimes used to clean up the polarization.[1] Here a QWP at 45° and a mirror are used to flip the polarization and take advantage of clean transmission through the PBS in the empty port. This part is also used as a delay line by mounting the mirror on a motorized linear stage (Newport MFA-CC). The alternative would be to use two PBSes and a trombone delay line using two mirrors in one of the ports. The advantage of the employed solution is that fewer components and less space are needed, and that the back-reflection is easier to align.

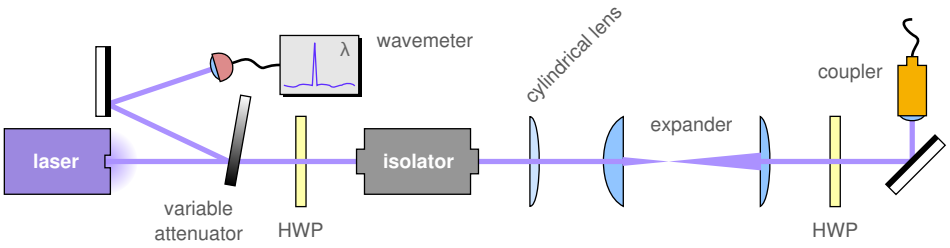

Figure 2.5: Coupling of the laser (405 nm). A rotational reflective attenuator serves for adjusting pump power, while the reflected beam is coupled into a wavemeter. An isolator prevents any reflections from entering the laser. A half-wave plate (HWP) rotates the polarization to match the isolator and maximize transmission. Ellipticity of the beam is corrected using a 200-mm cylindrical lens and two spherical lenses that serve as an expander (50 mm and 125 mm). Before coupling, a HWP rotates the polarization so that it matches the slow axis of a polarization-maintaining fibre.

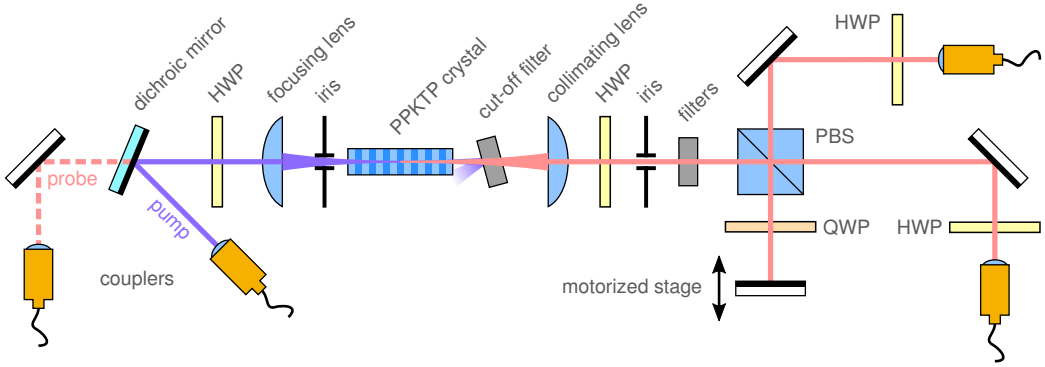

Figure 2.6: The optical setup of the SPDC source. All optical inputs and outputs are coupled in single-mode polarization-maintaining fibres. All components before the crystal are designed and coated for the pump wavelength 405 nm; all components afterwards are for 810 nm (the faces of the crystal are dual-band AR-coated). A dichroic mirror allows a probing beam at 810 nm to enter the setup. The linear polarization of the pump is rotated using a half-wave plate (HWP) onto a vertical polarization. A 100-mm lens provides focusing into the nonlinear crystal. Afterwards, a cut-off filter removes most of the pump. The down-converted signal and idler are collimated using a 150-mm lens. A HWP is used for alignment and to match the frame of reference of the crystal to the polarizing beam splitter (PBS). Further cut-off and band-pass filtering is carried out using additional filters. The PBS separates signal and idler into two arms. One of them goes through a delay line, where a motorized mirror serves as a back-reflector. A double pass through a quarter-wave plate (QWP) makes sure that the delayed beam is transmitted through the PBS into the top arm. HWPs in front of the fibre couplers serves to match the linear polarizations with slow-axis modes of the fibres.

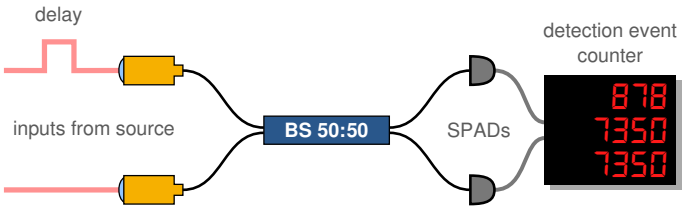

Figure 2.7: Measurement setup used for alignment and observing Hong-Ou-Mandel interference. Both outputs of the source are connected to a balanced fibre beam splitter (BS). Then, single-photon avalanche diodes (SPADs) detect the rates of incident photons and their simultaneous detections (coincidences).

2.2.3 Alignment

The initial alignment was performed with multi-mode fibres and aimed to find the SPDC signal and coincidences (simultaneous detections). The crystal temperature and pump polarization were roughly optimized. Then, polarization-maintaining (PM) single-mode fibres were put in place and the corresponding HWPs were rotated into correct positions.[117]

Final optimization of all factors was done using the weak SPDC signal on a single-photon level using the following method. First, the constraint of collinearity of the coupled modes needs to be applied. This method requires the measurement setup depicted in Figure 2.7. First, the HWP before the PBS is rotated by 22.5°. This splits each generated signal evenly into both arms. Then, to align the coupling in a signal or idler arm, the other arm is blocked. The coupled light is split on a beam splitter and coincidences are detected; they come from the photon pairs coupled in the same spatial mode by a single coupler. Alignment is done with respect to coincidences. After both arms are done, the HWP is rotated back. This method was routinely used to correct for misalignment and proved to be effective with respect to optimizing count rate, coupling efficiency and interference visibility. It proved superior even in the case of a angle-phase-matched BBO source than a similar technique described in reference 1.

The measurement setup in Figure 2.7—with both arms unblocked and signal and idler separated—is an established measurement technique of the photons' interference with each other. First presented by Hong, Ou and Mandel,[41] this technique serves as a measure of quality for photon pairs. It ensures that the generated photons are indistinguishable in all degrees of freedom (except for the spatial modes that interfere). This is essential for confirming spectral degeneracy of the photons.

The Hong-Ou-Mandel effect is usually measured with respect to a variable delay introduced to one of the photons (delay line in Figure 2.6). Non-interfering photon pairs can cause a coincidence event on the two SPADs. If the photons in-

terfere perfectly, they bunch into a superposition of two pairs ($|11\rangle \rightarrow [|20\rangle + |02\rangle]/\sqrt{2}$), which causes a drop in the coincidence event rate. Plotting the coincidence rate with respect to the time delay is called a Hong-Ou-Mandel (HOM) dip.[1,B3] Its shape is determined by the temporal/spectral properties of the photons.[41] The measured data are shown later in Figure 2.8. HOM visibility is defined as the ratio of the drop in coincidences and the maximum coincidence rate. Any alignment should maximize it towards 100 %.

Coming back to alignment, the HOM visibility can be measured immediately after adjusting both arms, because the BS is already in place. This is practical for verifying major alignment steps. Using the alignment method, it is first necessary to establish the crystal temperature that maximizes coincidence rate. Then, the longitudinal position of the crystal and collimating lens are varied so that the overall coincidence rate is maximized. The coincidence rate is a product of an overall SPDC gain (photon pair generation rate) and the coupling efficiencies of both arms. In theory, these variables should have a common maximum, although in practice, a change in a non-ideal alignment may result in an opposing behaviour. For a heralded single photon source, the crucial variable is the coupling efficiency.

2.2.4 Mutual coherence and spectrum

The spectral and temporal properties of the down-converted biphotons are necessary to understand the modal structure and statistics of the signal. The joint spectral amplitude $\phi(\omega_1, \omega_2)$[41] is basically a normalized projection of the spatial-spectral superposition profile Ψ (2.1) onto the measured modes.[106]

The joint spectrum determines the effective width of a single mode for heralded single photons, which manifests in Hong-Ou-Mandel two-photon interference. Considering the condition (2.2), we can work with an angular frequency shift $\Delta\omega$ in $\phi(\omega_0/2 + \Delta\omega, \omega_0/2 - \Delta\omega)$. The relevant spectrally degenerate case means that $\phi(\Delta\omega)$ is symmetric and peaked at $\Delta\omega = 0$. The HOM interference then depends on a cross-correlation of a Fourier transform of the spectral amplitude ϕ.[41] Let the Fourier transform be

$$G(t) = \int_{-\infty}^{\infty} \phi(\Delta\omega)\, e^{-i\Delta\omega t}\, \mathrm{d}\Delta\omega. \tag{2.5}$$

For real and symmetric ϕ, $G(t)$ is also real. Its normalized cross-correlation is

$$\widetilde{d}(\tau) = \frac{\int_{-\infty}^{\infty} G(t)\, G(t+\tau)\, \mathrm{d}t}{\int_{-\infty}^{\infty} G^2(t)\, \mathrm{d}t}. \tag{2.6}$$

The number of coincidences in the dip is then $d(\tau) = C(1 - V \cdot \widetilde{d}(\tau))$. The parameters are the coincidence rate C with no interference, and visibility V.

The HOM dip was measured using the setup shown in Figure 2.7 and the data are presented in Figure 2.8. The plot shows the dependence of coincidence detections relative to the temporal delay between the two photons. The FWHM is 1.0 ps, which is considered as the effective width of a single down-converted mode. The sub-unity visibility is mainly attributed to temporal resolution of the detectors, an imbalance in BS splitting ratio and imperfect polarization overlap.

Since the relation between the joint spectral amplitude and the HOM dip is known, the spectral profile can be numerically calculated based on HOM data without any direct spectrography.[118] The data show systematic fluctuations in the overall rate, which results in an asymmetry in the edges of the HOM dip. The data show reasonable symmetry between ±1 ps delay (light-blue region), so these points were used as numerical data $\{d_r = d(\tau_r)\}_{r=0}^{n-1}$, where the number of samples n is odd and τ_r goes symmetrically from -1 to 1 ps with a step of $\delta\tau$. The coincidence level C at the edges is 45000. Then $\widetilde{d}_r = C - d_r$, which may be padded by zeroes on each side to control sampling. Using a standard definition of a discrete Fourier transform

$$\mathrm{DFT}(f)_s = \sum_{r=0}^{n-1} f_r e^{-2\pi r s/n}, \tag{2.7}$$

the cross-correlation (2.6) is inverted by

$$\widetilde{D}_s = \mathrm{DFT}\left(\widetilde{d}_r\right) e^{-\pi i \frac{n-1}{n} s} \delta\tau, \tag{2.8}$$

$$G_r = \mathrm{DFT}^{-1}\left(\sqrt{|\widetilde{D}_s|}\right) \frac{1}{\delta\tau}. \tag{2.9}$$

More details on discrete Fourier transforms, sampling and mathematical caveats can be found in section 2.4.1. Finally, the joint spectral amplitude is obtained by

$$\phi_s = \mathrm{DFT}^{-1}\left(G_r\right). \tag{2.10}$$

The corresponding values $\Delta\omega_s$ are separated by $2\pi/(n \cdot \delta\tau)$. The amplitude is not normalized and exhibits periodicity, but it can be rescaled to meet any discrete analogue of the condition $\int |\phi|^2 = 1$.

The result is shown in Figure 2.9, where signal wavelength is used instead of angular frequency deviation. Errors and irregularities in the input data result in numerical artefacts that are most visible on the sides of $|\phi|$. The final estimate of ϕ interpolates the absolute values of the central peak and setting everything else to zero. This estimate is then compared to the measured data by applying (2.5) and (2.6) to the interpolation; the corresponding red dashed line is shown

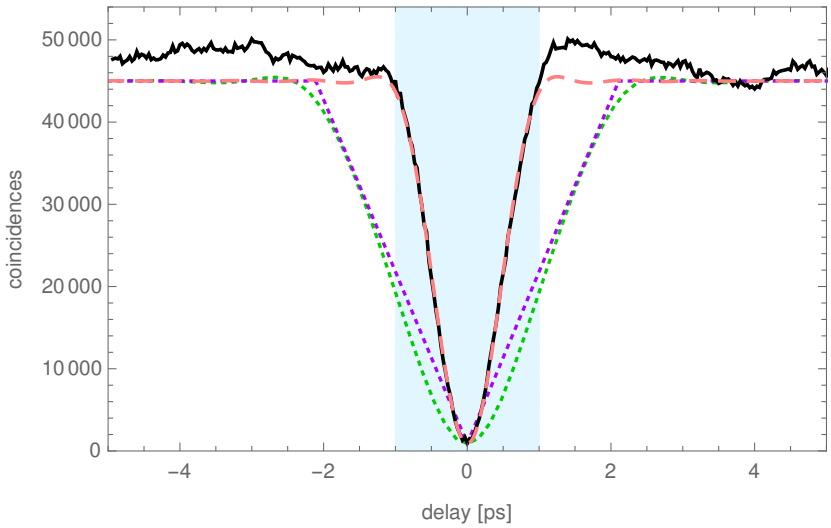

Figure 2.8: The Hong-Ou-Mandel dip. The black curve represents the data and their statistical error. The drift comes from systematic errors, most likely pump stability. HOM visibility = 98.9 ± 0.2 % from data; the best fit of the models is 98 %. A perfect sinc-spectrum dip is shown by the triangular purple dotted curve. Further augmentation by a band-pass filter is estimated by the green dotted curve. The red dashed curve represents the numerical model based on the interpolated spectral profile presented in Figure 2.9. The light-blue region designates the data range that was the basis of the numerical model.

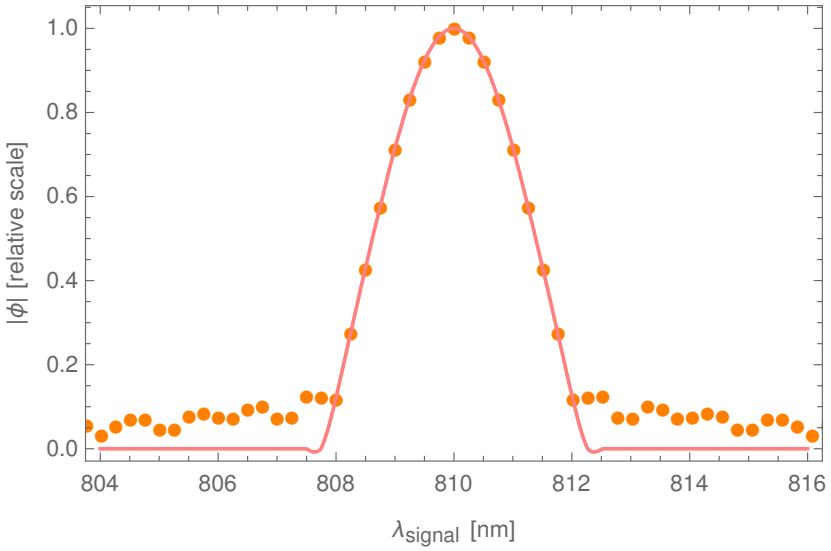

Figure 2.9: The joint spectral amplitude numerically calculated from the HOM data. The relation (2.2) binds the frequencies of signal and idler; the wavelengths are approximately $(\lambda_{\text{signal}} + \lambda_{\text{idler}})/2 \approx 810$ nm. Orange dots are the numerical result and the red line is the interpolation of the central peak with side-artefacts cleaned up.

in Figure 2.8. The FWHM of joint spectral intensity $|\phi|^2$ is 2.0 nm, which means that the phase-matching is roughly comparable to the FWHM of the band-pass filter. If the filter was as narrow as 3.1 nm (a typical value claimed by the manufacturer), the joint spectral intensity FWHM would be 2.6 nm. This differs significantly from the theoretical expectation. Considering Gaussian beams and the material data, the profile should be approximately the same as for planar waves – sinc-shaped (2.4). The ideal FWHM without any filtering would be 0.9 nm. The widening could be due to possible irregularities in the poling pattern that could result in an effectively wide distribution of poling periods. Spherical and other aberrations of the lens could also contribute a different phase-matching shape than for ideal Gaussian beams.

2.2.5 Statistical properties

The quantitative measure of an SPDC source is the rate of detected photon pairs. This depends on the SPDC overall gain and optical loss in the path towards detection. It is somewhat ambiguous to decide where the division between the source and detection is. The convention used here assumes that even detection efficiency is a part of the overall loss of the source so that there is no need for data correction.

As the $\chi^{(2)}$ nonlinear process represents an interaction of three waves, any signal generated from vacuum represents a photon pair – a simultaneous excitation of two modes, even though the superposition of such modal pairs is quite complex.[B1] Coupling and detection is multimode, primarily in terms of time and spectrum. Even though each generated mode has a different overlap with the detection modes, all the factors and their complexity can be reduced to two efficiencies η_s, η_i; they represent the effective transmittance of each photon.

The initial statistics of photon pairs in a single mode is Bose-Einstein (follows a geometric series).[B1] However, one mode is about 1 ps wide, as shown in the previous section. The width of the detection mode is of the order of nanoseconds, usually 2 ns. Summing such a high number of independent modes results in Poisson statistics. The generation rate also allows us to work in the single-pair approximation (2.1). The probability of n_1, n_2 photons in the respective detection modes is then

$$P^{\text{init}}_{n_1,n_2} = \begin{cases} \frac{\gamma^n}{n!} e^{-\gamma} & n_1 = n_2 = n \\ 0 & n_1 \neq n_2 \end{cases} . \tag{2.11}$$

The gain factor γ represents the projection of $|\Psi|^2$ times the effective number of

modes. The optical loss introduces the transformation

$$P_{n_1,n_2} = \sum_{k=n_1}^{\infty} \sum_{l=n_2}^{\infty} \binom{k}{n_1} \binom{l}{n_2} \eta_1^{n_1} \eta_2^{n_2} (1-\eta_1)^{k-n_1} (1-\eta_2)^{l-n_2} P_{k,l}^{\text{init}}. \tag{2.12}$$

The transformation is written in a general form, although in this case, the indices k, l may be joined into one. This model can be simplified and various terms neglected if the time window is short and $\gamma \ll 1$, which is commonly true for continuous-wave SPDC.

The quantitative measures of SPDC that can be obtained from detecting photons in each arm are the rates. The coincidence rate R_c is the number of simultaneous detections per time unit; a coincidence occurs if detectors in signal and idler arms both register a photon within a time window τ_c. The rate of detections on individual detectors are R_1, R_2.

If there was no optical loss, there would be only photon pairs present so that $R_c = R_1 = R_2$. The effect of the transmittances on the pair generation rate $\mathcal{R} = \gamma/\tau_c$ is $R_1 = \eta_1 \mathcal{R}$, $R_2 = \eta_2 \mathcal{R}$, and $R_c = \eta_1 \eta_2 \mathcal{R}$. A common parameter to characterize efficiency is their geometric mean $\eta = \sqrt{\eta_1 \eta_2}$. So, the data can be used to establish

$$\eta = \frac{R_c}{\sqrt{R_1 R_2}}, \tag{2.13}$$

$$\eta_1 = \frac{R_c}{R_2}, \tag{2.14}$$

$$\eta_2 = \frac{R_c}{R_1}, \tag{2.15}$$

$$\gamma = \frac{R_1 R_2}{R_c} \tau_c. \tag{2.16}$$

Using 1 mW of pump power and two SPAD modules Excelitas SPCM CD3543H with a specified 70% efficiency and $\tau_c = 1.6$ ns, the measured rates are $R_c = 146$ kcps, $R_1 = 357$ kcps, $R_2 = 371$ kcps (thousands of counts per second). The efficiencies are $\eta_1 = 39.3\%$, $\eta_2 = 40.9\%$, $\eta = 40.1\%$, where number 1 corresponds to the transmitted arm and number 2 is the delayed arm (Figure 2.6). The gain factor would be $\gamma = 1.5 \times 10^{-3}$.

Considering a single-photon source, these parameters are essential for the quality of the heralded single-photon state. One of the arms is designated as the trigger arm and it conditions a single-photon state in the other arm (signal arm) by detection. The statistics of the conditioned state can be calculated from (2.12)

by $p_{n_s} = \sum_{n_i=1}^{\infty} P_{n_s,n_i}$. If $\gamma \ll 1$, which is usually the case, then

$$p_0 \approx 1 - p_1 - p_2, \tag{2.17}$$
$$p_1 \approx \eta_s, \tag{2.18}$$
$$p_2 \approx \frac{1}{2}\gamma\eta_s^2(2-\eta_t), \tag{2.19}$$
$$p_{n>2} \approx \gamma^{n-1} \approx 0. \tag{2.20}$$

Even though $p_2 \ll p_1$, the term is not neglected, because it represents the dominant error contribution. The above statistics can be optimized by the means of experimental parameters, but the optimization depends on the application or definition by the user. It is generally good to optimize efficiencies, as the gain in p_1 outweighs any gain in error. As $\gamma = \mathcal{R}\tau_c$, it is necessary to avoid excessively wide coincidence windows. The lower limit is the detector jitter (see section 2.3.1), so further narrowing of the window would result in losing some signal beside the noise. There are some metrics, where the time window can be optimized (see section 3.2.5). Of course, generation rate $\mathcal{R}$ can be lowered by reducing pump power, which is the most convenient way of arbitrarily reducing gain and the multi-photon contribution. However, if this could be referred to as an increase in quality, it is accompanied by a decline in quantity, as the rate of generating such heralded states decreases. The suitable trade-off usually depends on practical limits in the experiment such as available time and background noise.

The most common quantity that is measured is the $g^{(2)}(\tau)$ temporal correlation function that is the quantum analogue of intensity cross-correlation from classical optics.[20,B5,B6] Its fundamental significance is that for classical light, the value $g^{(2)}(0) \geq 1$. Single-photon light in particular should exhibit $g^{(2)}(0) \ll 1$. In terms of photon-number probabilities, it is

$$g^{(2)}(0) := \frac{\langle n(n-1)\rangle}{\langle n\rangle^2} \approx \frac{2p_2}{p_1^2} \approx \mathcal{R}\tau_c(2-\eta_t). \tag{2.21}$$

The value scales linearly with gain (pump power) and the time window, but does not depend on optical loss in the signal. Using the presented values, the estimate is $g^{(2)} = 2.3 \times 10^{-3}$.

The standard way of directly measuring $g^{(2)}(0)$ is by Hanbury-Brown-Twiss measurement.[1,119] The scheme is shown in Figure 2.10. Trigger detections with rate R_t condition any detections in the signal arm. Conditioned detections on the two SPADs are effectively two-fold coincidences with the trigger; the rates are R_{s1}, R_{s2}. Undesirable two-photon events manifest by all detectors registering a signal with rate $R_{s1,s2,t}$. Then, an anticorrelation parameter may be calculated

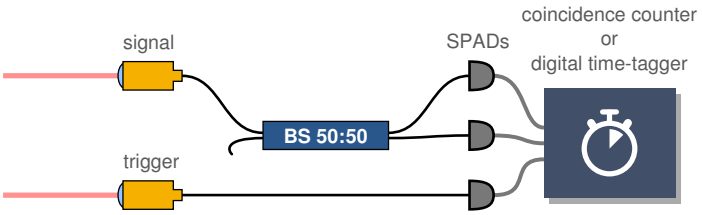

Figure 2.10: The Hanbury-Brown-Twiss measurement used to establish $g^{(2)}(0)$. The heralded signal is split into two channels and the detection electronics evaluates the rates of all combinations of single/coincidence detections.

that is approximately equal to $g^{(2)}(0)$,[20]

$$g^{(2)}(0) \approx \frac{R_{s1,s2,t}R_t}{R_{s1}R_{s2}}. \tag{2.22}$$

This value can be determined by measurements in Chapter 3. The lowest measured value for the discussed SPDC source comes from data presented in Figure 3.12 and is $g^{(2)}(0) = (1.8 \pm 0.2) \times 10^{-4}$.

It should be noted that the $g^{(2)}(0)$ value itself serves primarily for proving that the single-photon state is nonclassical. It cannot be considered a metric by itself, as there are many possible ways of quantifying multiphoton content in single-photon states. One of them—quantum non-Gaussianity—is the subject to which Chapter 3 is devoted.

2.3 Single-photon avalanche diodes (SPAD)

2.3.1 General description

This section provides a general description of single-photon avalanche diodes and their known properties.[B3]

SPADs are semiconductor avalanche diodes operated with a reverse voltage that is above the breakdown voltage. Upon an absorption of a photon, an electron-hole pair may be excited in the p-n junction of the diode. The carriers are accelerated by the reverse voltage and kinetically excite more carriers in an avalanche. Because the voltage is above breakdown, the current avalanche needs to be quenched before it damages the SPAD. An electronic quenching circuit is designed to bring the voltage to zero upon a successful detection, so that the current breaks off and the SPAD is reset to its initial state. Then, the reverse voltage is applied again and the SPAD becomes sensitive to incident light. The time between the avalanche and the reapplication of the reverse voltage is called

recovery time; in this work it is denoted by τ_R and its typical value is in the order of tens of nanoseconds. During recovery time, the detector is unable to register any new photons.

The work presented in this theses utilizes silicon SPADs, which have optimal efficiency in the visible spectrum. All detected signals were at 810 nm, where the typical efficiency of detecting a photon is 50–70 %.

Important aspects of SPADs include their temporal properties. A response time is the time between the incidence of an optical signal and the emission of an electronic pulse by the SPAD. The response time itself is not of importance in the presented experiments; one only needs to keep the SPAD outputs synchronized relatively to each other.

The relative time uncertainty of the output signal is called jitter, which is commonly defined as a FWHM of the detection-to-output time distribution. When a photon excites carriers in the detector, their location and the dynamics of the avalanche can vary. This is the primary cause of inherent jitter. Additional factors may include noise in the amplification circuit and the accuracy of the detection-processing electronics. The reason is that a detection is recognized by the location of the leading edge of the SPAD output signal, so any electronic noise contributes to jitter as well. Typical values for detectors in this work are in the order of fractions of a nanosecond.

Dark counts represent the ocurrence rate of background detections present without any incident signal. These are caused by thermal excitation of carriers and are influenced by the quality of the diode material, temperature and bias voltage. Values depend on the type of the SPAD and its age, in this work typically 10–500 counts per second.

Another type of false counting arises from carriers trapped in energy levels close to the conduction band that represent impurities in the material. After quenching and recovery, these carriers may cause an avalanche by themselves, resulting in a so-called afterpulse. Afterpulsing is expressed by a probability of occurrence p_a and a temporal distribution. Photons arriving during recovery time also contribute to afterpulsing, because the carriers they excite may cause an avalanche immediately after the reverse voltage is applied. This adds to p_a a factor that grows linearly with the incident light intensity. In the literature, these events are referred to as twilight pulses.

The significance of the above-mentioned parameters and imperfections varies depending on the measurement. Finite detection efficiency effectively translates into additional optical loss, which may be an issue in quantum information processing or secure quantum communication.

The effect of recovery time results in detector saturation and affects its linearity, which needs to be corrected in metrological applications, where the real event rate needs to be determined. In this case, a correction for afterpulsing

needs to be applied as well. The correction formula (2.24) is derived in the following section.

Timing jitter mainly affects the amount of background noise collected in experiments with closely correlated photons. Since simultaneous detections need to be recognized, the coincidence time window defining a coincidence event cannot be much shorter than the jitter. Otherwise, signal would be lost. On the other hand, the amount of random signal increases with the width of the coincidence window.

Dark counts present a typical signal-to-noise ratio problem. Usually, they are subtracted from the number of detections along with the overall background. In experiments where only correlated photons matter, the contribution of dark counts is usually negligible.

There are several trade-offs related to the parameters of SPADs. The thickness of the junction defines many operational characteristics, including jitter, efficiency and afterpulsing.[94,120] Increasing the bias voltage may increase detection efficiency at the cost of dark count rate and afterpulsing. SPADs are also commonly Peltier-cooled, because lower operating temperature decreases dark counts. Afterpulsing can be suppressed by lowering the avalanche charge and slightly extending recovery time beyond mere quenching so that a sufficient amount of trapped carriers has enough time to decay. However, the trapped carrier lifetime increases with lower temperatures, so that afterpulsing needs to be balanced against dark count elimination.

2.3.2 Counting model

The following three sections presents modelling the probability distribution of the number of detections in a fixed time window; usually referred to as counting statistics. Two approaches are presented – numerical and analytical. This section establishes the stochastic process (2.23) and derives a rate correction formula (2.24). Section 2.3.3 presents an analytical model that is derived from a simplified stochastic model of recovery time and afterpulsing. Section 2.3.4 describes the numerical simulation that was used to model the process (2.23) as well as check the analytical formula. All three sections represent original results.

Let us consider the overall efficiency of the detector as a separate attenuation process that only scales the apparent incident intensity, but has no other effect. The basis of the model is therefore a homogeneous Poisson point process[B7] that is modified by considering basic detector imperfections – recovery time and afterpulses.[B3]

Let us work with interarrival time Δt, which is the time interval between two successive detections. Each measurement results in a series of detections

distributed in time. Equivalently, the data can be considered a series of interarrival times. Each interval is a particular realization of a stochastic process. An important assumption is that only a single process is considered, which means that after each detection, the detector is reset to the same state and individual interarrival times are independent variables. Although this assumption is sufficient for the experiment in Chapter 4 and is widely used in the community, it has been only recently found not to be entirely true for all detectors.[93,94]

The objective of the model is to find the probability density function (PDF) of interarrival time $p(\Delta t)$. In the case of a perfect detector illuminated with constant intensity, the detections would exhibit a uniform temporal density λ and interarrival times would be exponentially distributed. For a homogeneous process, this distribution holds with respect to any point in time, so recovery time τ_R can be simply incorporated by a shift: $p_{\text{rad}}(\Delta t) = \lambda e^{-\lambda(\Delta t - \tau_R)}$ for $\Delta t > \tau_R$, zero otherwise. As no signal can arrive earlier than τ_R, let $t = \Delta t - \tau_R$ and the PDF component representing radiation is $p_{\text{rad}}(t) = \lambda e^{-\lambda t}$. Here, λ contains the incident photon flux times the overall detection efficiency, and background (dark counts) as well.

The next step is to incorporate afterpulsing. An electronic afterpulse occurs with a fixed probability a and arrives at a certain time that is distributed with PDF $p_{\text{AP}}(t)$. Then there are so-called twilight pulses that always arrive just after detector recovery ($p_{\text{TwP}}(t) = \delta(t)$, a Dirac delta distribution) and their probability is proportional to the incident rate by a factor of α. In the case when an electronic afterpulse is going to happen, a detection at time t can occur either due to afterpulsing or a radiation detection before the afterpulse arrives. The first case is conditioned by no radiation detection occurring before t and an afterpulse arriving at t, which results in probability $e^{-\lambda t} p_{\text{AP}}(t)$. The second case is vice versa. No afterpulse before t can be denoted by $(1 - \widetilde{p}_{\text{AP}}(t))$, where the primitive function $\widetilde{p}_{\text{AP}} = \int_0^t p_{\text{AP}}$. The resulting PDF in an event of an afterpulse is $p_{\text{r-AP}}(t) = e^{-\lambda t} p_{\text{AP}}(t) + (1 - \widetilde{p}_{\text{AP}}(t))\lambda e^{-\lambda t}$.

Finally, all contributions are summed with the respective probabilities $p(t) = \alpha\lambda p_{\text{TwP}}(t) + a p_{\text{r-AP}}(t) + (1 - a - \alpha\lambda) p_{\text{rad}}(t)$. After all substitutions, the result is

$$\begin{aligned} \Delta t &= \tau_R + t, \\ p(t) &= \alpha\lambda\delta(t) + a\left[e^{-\lambda t}\, p_{\text{AP}}(t) + (1 - \widetilde{p}_{\text{AP}}(t))\lambda e^{-\lambda t}\right] \\ &\quad + (1 - a - \alpha\lambda)\lambda e^{-\lambda t}. \end{aligned} \tag{2.23}$$

This model can be used to numerically simulate data for any event rate λ (see section 2.3.4). It was used to provide all theoretical predictions of photon-number distributions that are used in Chapter 4.

The model also establishes an analytical correction for saturation of the detector due to afterpulsing and dead time. Conventionally, the rate correction for recovery time is $\lambda_{\text{det}} = \lambda/(1+\lambda\tau_R)$ and for afterpulses $\lambda_{\text{det}} = (1+a+a\lambda)\lambda$.[121] Multiplicating both contributions can serve well for small corrections, but does not treat the interaction between both phenomena. The formula (2.23) accounts for both recovery time and afterpulsing correctly up to the accuracy of the assumed mechanisms. These mechanisms can be modified, generalized or simplified at the discretion of the experimentalist, depending on the required accuracy of the detection model. This would result in different forms of $p(t)$. From equation (2.23), one can compute the mean detection rate $\lambda_{\text{det}} = \langle \Delta t \rangle^{-1}$,

$$\lambda_{\text{det}} = \left(\frac{1}{\lambda} - \frac{a}{\lambda} \int_0^\infty p_{\text{AP}}(t)\, e^{-\lambda t}\, \mathrm{d}t + \tau_R - \alpha \right)^{-1}. \tag{2.24}$$

The required parameters τ_R, a, α and $p_{\text{AP}}(t)$ can be established by direct measurements.

2.3.3 Analytical counting model

Commonly used counting models for non-paralyzable Geiger-mode detectors only take into account saturation due to recovery time. Some models simply subtract the overall recovery time from the time interval,[121] others calculate the respective point process, but assume that the detector is unblocked at the start of each counting interval.[B3,122] The exact formula describing recovery time was published by Müller.[105] This formula is generalized here.

Using the point process approach, one can derive an analytical formula that also incorporates afterpulsing, although not in the scope considered in the previous section. The assumption is that after each recovery time of length τ_R, another detection may immediately take place with probability p_a. Any model that would assume more complicated phenomena, such as afterpulse decay time statistics, needs to be simulated by Monte Carlo methods. For silicon SPADs, the dominant portion of afterpulsing takes place very soon after the end of recovery time, which justifies the approximation.

The model is formulated for a constant incident rate λ as a probability density function (PDF) for interarrival time $\Delta t = \tau_R + t$, where the stochastic part t has a PDF

$$p_{\text{inter}}(t) = p_a \delta(t) + (1 - p_a)\lambda e^{-\lambda t}, \quad t \geq 0. \tag{2.25}$$

It is therefore a combination of an afterpulse and a homogeneous Poisson point process. λ is an incident event rate that incorporates background counts as well as overall SPAD efficiency, which are phenomena that add up to a Poisson process

that subsequently becomes distorted by recovery time and afterpulsing. $\delta(t)$ is the Dirac delta distribution.

Let us work with the temporal PDFs of the 1st, 2nd, ..., n^{th} detection. First, let us consider the case when the detector is free (not recovering) at time zero. The probability of no detection up to time t is $P_0^{\text{free}}(t) = \exp(-\lambda t)$. The PDF of the first detection is simply $p_1^{\text{free}}(t_1) = \lambda \exp(-\lambda t_1)$. Then, recovery time follows, so that the time of the second detection $t_2 \geq t_1 + \tau_R$. The PDF of the second detection integrates over all possible times t_1 of the first detection:

$$p_2^{\text{free}}(t_2) = \int_0^{t_2-\tau_R} p_1^{\text{free}}(t_1) p_{\text{inter}}(t_2 - (t_1 + \tau_R)) \mathrm{d}t_1, \quad t_2 \geq \tau_R. \tag{2.26}$$

By extension, the PDF of each detection is always a convolution of the PDF of the previous detection and PDF of the interarrival time,

$$p_n^{\text{free}}(t) = \int_{(n-2)\tau_R}^{t-\tau_R} p_{n-1}^{\text{free}}(t') p_{\text{inter}}(t - t' - \tau_R) \mathrm{d}t', \tag{2.27}$$

$$\begin{aligned} p_n^{\text{free}}(t) = {} & \lambda e^{-\lambda[t-(n-1)\tau_R]} \\ & \times \sum_{k=0}^{n-1} \binom{n-1}{k} p_a^{n-1-k} (1-p_a)^k \lambda^k \frac{[t-(n-1)\tau_R]^k}{k!}, \end{aligned} \tag{2.28}$$

where $t \geq (n-1)\tau_R$. Now, let us consider the probability of n detections in a time window between zero and T. This means that the n^{th} detection happens at time $t < T$ and no more detections happen afterwards. If recovery time goes beyond the time window, $t + \tau_R > T$, then no further detections can take place. In the other case, if $t \leq T - \tau_R$, then the probability of no further detections occurring is the product of no afterpulsing and no detections afterwards, which is equal to $(1-p_a)\exp(-\lambda(T-\tau_R-t))$. Both cases are possible if $n \leq \lfloor T/\tau_R \rfloor - 1$. If we denote the maximum amount of recovery times that fit inside the detection window $N \coloneqq \lfloor T/\tau_R \rfloor$, then the maximum amount of detections is $N+1$. Considering the time requirements of both cases, the probability of n detections is

$$\begin{aligned} P_{n\leq N}^{\text{free}}(T) = {} & (1-p_a) \int_{(n-1)\tau_R}^{T-\tau_R} p_n^{\text{free}}(t) e^{-\lambda(T-\tau_R-t)} \, \mathrm{d}t \\ & + \int_{T-\tau_R}^{T} p_n^{\text{free}}(t) \, \mathrm{d}t. \end{aligned} \tag{2.29}$$

$$P_{N+1}^{\text{free}}(T) = \int_{N\tau_R}^{T} p_N^{\text{free}}(t) \, \mathrm{d}t. \tag{2.30}$$

Let us now abbreviate $M_n \coloneqq \lambda(T - n\tau_R)$, which could be interpreted as an ideal mean number of detections in the time window reduced by n recovery times. Also, let $Q_k(x) = \exp(-x)\sum_{m=0}^{k-1} x^m/m!$ be the regularized upper incomplete Gamma function, which in this special case of $k \in \mathbb{N}^0$ represents the probability of a Poissonian variable with mean x to be less than k (note that $Q_0(x) = 0$). Then, the resulting probability is

$$P_0^{\text{free}}(T) = e^{-M_0}, \tag{2.31}$$

$$\begin{aligned} P_{1\le n\le N}^{\text{free}}(T) = &\sum_{k=0}^{n-1}\binom{n-1}{k} p_a^{n-1-k}(1-p_a)^k \\ &\times\left(Q_{k+1}(M_n) - Q_{k+1}(M_{n-1}) + (1-p_a)\frac{M_n^{k+1}}{(k+1)!}e^{-M_n}\right), \end{aligned} \tag{2.32}$$

$$P_{N+1}^{\text{free}}(T) = 1 - \sum_{k=0}^{N}\binom{N}{k} p_a^{N-k}(1-p_a)^k Q_{k+1}^N \tag{2.33}$$

where the terms $Q_k(M_n)$ can be viewed in terms of the interpretations mentioned above. These equations give a counting model assuming the detector is free at the beginning. However, if the detector is recovering at $t = 0$ and keeps inactive for a certain initial time $\tau_i < \tau_R$, then the initial detection has the PDF

$$p_1^{\text{rec}}(t_1, \tau_i) = p_a\delta(t_1 - \tau_i) + (1-p_a)\lambda e^{-\lambda(t_1-\tau_i)}. \tag{2.34}$$

Like before, multiple convolutions result in the n^{th} detection PDF

$$\begin{aligned} p_n^{\text{rec}}(t, \tau_i) = &a^n\delta\left(t - (n-1)\tau_r - \tau_i\right) + e^{-\lambda[t-(n-1)\tau_R-\tau_i]} \\ &\times\sum_{k=1}^{n}\binom{n}{k} p_a^{n-k}(1-p_a)^k\lambda^k\frac{\left[t-(n-1)\tau_R-\tau_i\right]^{k-1}}{(k-1)!}, \end{aligned} \tag{2.35}$$

where $t \ge (n-1)\tau_R + \tau_i$. By integration analogous to (2.29), the probability of n detections in a time window T then is

$$P_0^{\text{rec}}(T, \tau_i) = (1-p_a)e^{-\lambda(T-\tau_i)}, \tag{2.36}$$

$$\begin{aligned} P_{1\le n<N}^{\text{rec}}(T, \tau_i) = &(1-p_a)p_a^n e^{-\lambda(T-n\tau_R-\tau_i)} \\ &+ (1-p_a)e^{-\lambda(T-n\tau_R-\tau_i)} \\ &\times\sum_{k=1}^{n}\binom{n}{k} p_a^{n-k}(1-p_a)^k\lambda^k\frac{(T-n\tau_R-\tau_i)^k}{k!} \\ &+ \sum_{k=1}^{n}\binom{n}{k} p_a^{n-k}(1-p_a)^k \\ &\times\left[Q_k(\lambda(T-n\tau_R-\tau_i)) - Q_k(\lambda(T-(n-1)\tau_R-\tau_i))\right], \end{aligned} \tag{2.37}$$

which is similar to (2.32), except for the first term and the τ_i contribution. The first term is kept separate intentionally for consistent analytic integration in the subsequent step.

However, if $n = N$, then the initial time τ_i determines whether the final recovery time will be inside or outside the detection window. The border value is $\tilde{\tau}_i = T - N\tau_R$. Therefore we need to split the two cases, while for $n = N + 1$ the final recovery time always goes beyond the detection window and no more detections are possible.

$$P_N^{\mathrm{rec}}(T, \tau_i < \tilde{\tau}_i) = P_{1\le n<N}^{\mathrm{rec}}(T, \tau_i)\Big|_{n=N}, \tag{2.38}$$

$$P_N^{\mathrm{rec}}(T, \tau_i > \tilde{\tau}_i) = \int_{(N-1)\tau_R+\tau_i}^{T} p_N^{\mathrm{rec}}(t, \tau_i)\,\mathrm{d}t, \tag{2.39}$$

$$P_{N+1}^{\mathrm{rec}}(T, \tau_i < \tilde{\tau}_i) = \int_{N\tau_R+\tau_i}^{T} p_{N+1}^{\mathrm{rec}}(t, \tau_i)\,\mathrm{d}t, \tag{2.40}$$

$$P_{N+1}^{\mathrm{rec}}(T, \tau_i > \tilde{\tau}_i) = 0. \tag{2.41}$$

Now both cases P_n^{free} and P_n^{rec} need to be combined. In a measurement run, measurement intervals are periodically distributed with a fixed length T, while detections follow the probabilistic point process (2.25). So, in a long measurement, these two become uncorrelated and one can assume that the distribution of window beginnings with respect to detection events is completely random. Therefore, the proportion of 'free' windows to 'rec' windows is equal to the proportion of time periods when the detector was free and blocked, respectively, $\langle t\rangle : \tau_R$. Additionally, the distribution of τ_i is uniform between zero and τ_R. Taking both of these into account, the overall probability of n detections becomes a mixture

$$P_n(T) = \frac{\langle t\rangle}{\langle t\rangle + \tau_R} P_n^{\mathrm{free}}(T) + \left(1 - \frac{\langle t\rangle}{\langle t\rangle + \tau_R}\right) \frac{1}{\tau_R} \int_0^{\tau_R} P_n^{\mathrm{rec}}(T, \tau_i)\,\mathrm{d}\tau_i. \tag{2.42}$$

This mixture needs to be evaluated separately for the cases of $n = 0$, $n < N$, $n = N$, and $n = N+1$, because the probability distributions differ and the integration needs to be split to accommodate the piecewise definitions. After integration, renumbering of the summation indices and using the property $Q_0(x) = 0$, the probability of n detections during a time T is

$$P_0(T) = \frac{1-p_a}{1-p_a+\lambda\tau_R} e^{-M_1}, \tag{2.43}$$

$$\begin{aligned} P_{0<n<N}(T) = {} & \frac{1}{1-p_a+\lambda\tau_R} \\ & \times \sum_{k=0}^{n} \binom{n}{k} p_a^{n-k}(1-p_a)^k \Big[(k+1-p_a)\mathcal{Q}_{k+1}^{n+1} \\ & - M_{n+1}\mathcal{Q}_k^{n+1} - \Big(2k + (1-k/n)(1-p_a)\Big)\mathcal{Q}_{k+1}^{n} \\ & + (p_a k/n + 2M_n)\mathcal{Q}_k^n + k\,\mathcal{Q}_{k+1}^{n-1} - (k/n + M_{n-1})\mathcal{Q}_k^{n-1} \Big], \end{aligned} \tag{2.44}$$

$$\begin{aligned} P_N(T) = {} & \frac{1}{1-p_a+\lambda\tau_R} \Bigg\{ -M_0 \\ & + \sum_{k=0}^{N} \binom{N}{k} p_a^{N-k}(1-p_a)^k \Big[(p_a k/N + 2M_N)\mathcal{Q}_k^N \\ & - \Big(2k + (1-k/N)(1-p_a)\Big)\mathcal{Q}_{k+1}^{N} + k\,\mathcal{Q}_{k+1}^{N-1} \\ & - (k/N + M_{N-1})\mathcal{Q}_k^{N-1} \Big] \Bigg\} + N + 1, \end{aligned} \tag{2.45}$$

$$\begin{aligned} P_{N+1}(T) = {} & \frac{1}{1-p_a+\lambda\tau_R} \Bigg\{ M_0 \\ & + \sum_{k=0}^{N+1} \binom{N+1}{k} p_a^{N+1-k}(1-p_a)^k \Big[k\mathcal{Q}_{k+1}^{N} \\ & - \left(\frac{k}{N+1} + M_N\right)\mathcal{Q}_k^N \Big] \Bigg\} - N, \end{aligned} \tag{2.46}$$

where the terms M and $\mathcal{Q}$ are

$$M_n \coloneqq \lambda(T - n\tau_R), \tag{2.47}$$

$$\mathcal{Q}_k^n \coloneqq Q_k(M_n) = \begin{cases} 0 & \text{if } k = 0 \\ e^{-M_n} \sum_{i=0}^{k-1} M_n^i / i! & \text{if } k \geq 1 \end{cases}, \tag{2.48}$$

using parameters λ (incident rate), p_a (probability of an afterpulse) and τ_R (recovery time). The number of detections where the analytical expression changes is $N = \lfloor T/\tau_R \rfloor$.

In the limit of $p_a \to 0$, or $p_a \equiv 0$ if one postulates $0^0 := 1$, the relations are reduced to the form published by Müller for a dead-time-only process (equations (32)).[105] To capture twilight pulsing, p_a can be made a function of λ.

The relations (2.43) to (2.46) are an exact model of the point process defined by (2.25). As the definition is rather simple, the model can be conveniently verified using a Monte Carlo simulation. If the model was extended, for example by considering the temporal distribution of afterpulses as in (2.23), analytical solution would not be possible in such a simple and concise form as above. The most feasible approach then is Monte Carlo.

2.3.4 Counting simulation

A brief review of the simulation method will be provided. A Monte-Carlo approach to simulating SPAD detections was used by Stipčević and Gauthier,[103] but it presumed negative-exponential afterpulsing. The approach presented here works with the afterpulsing distribution obtained from data, incorporates twilight pulsing and handles photon detections and afterpulsing as independent processes.

A procedural program written in C was used for all simulations. Multithreading provides a very useful speed-up on CPUs with several cores. Using the library `pthread.h`, one simulation can be run in each thread. For random number generation, there are several options of various degrees of sophistication available. A satisfactory solution is provided by the GNU C Library, which provides a thread-safe BSD pseudo-random number generator (PRNG) `random_r`.

The main caveat is not to use only one PRNG. In one cycle, there are multiple points that need a purely random number, but some of them are conditioned on others. For example, a random number is generated only if the previous random number was lower than a certain value. This poses a more strict requirement on the randomness of the PRNG, which needs to be maintained even among conditioned values. The simulations revealed that the algorithm of `random_r` does not satisfy this property. The solution is to use multiple PRNGs, one for each random number in the cycle.

In the following pseudo-code, a uniform number between zero and one is returned by `random(0,1)`, the mean incident rate is `rate`, the constant afterpulse probability is `P_AFTERPULSE`, and the twilight pulse probability (proportional to the mean rate) is `p_twilight`. The temporal distribution of afterpulses is governed by function `APTime()`. The width of the detection window is `WINDOW`.

One cycle of the simulation changes the variable `time` to the time of the next detection event. The detection event counter is incremented and if needed, the count histogram is updated.

A single cycle is then

```
time += deadTime
r1 = random(0,1)
// only increment time if there is no twilight pulse
if (r1 > p_twilight)
    r1 -= p_twilight
    r2 = random(0,1)
    // sampling the negative exponential
    radiationDetTime = -log(r2)/rate
    if (r1 < P_AFTERPULSE)
        r3 = random(0,1)
        afterpulseDetTime = APTime(r3)
        // which came first
        if (afterpulseDetTime < radiationDetTime)
            time += afterpulseDetTime
        else
            time += radiationDetTime
        end
    else  // no twilight or afterpulsing, only radiation
        time += radiationDetTime
    end
end
// now 'time' holds the arrival time of the detection to be recorded
// check if the detection happens inside the current time window
while (time > WINDOW)
    time -= WINDOW // go to next window
    incrementHistogram(detectionEvents) // record detections until now
    detectionEvents = 0
end
detectionEvents += 1
```

The above pseudo-code provides one sample of a detection event. It is written in a general form to simulate the process established in section 2.3.2, but it can be simplified or expanded depending on how complex the detection model is. The random numbers `r1` to `r3` are intentionally distinguished to emphasize that they are generated using separate buffers representing separate PRNGs.

The number of runs for modelling the data in section 4 was 10^9 for each incident rate, and for the verification of relations (2.43) to (2.46), the number was 10^{11}.

2.4 Numerical and statistical methods

2.4.1 Fourier transforms

This section elaborates on the mathematical details used in section 2.2.4. Let the Fourier transform $\mathcal{F}$ of function f and its inverse be defined as

$$F(\xi) = \mathcal{F}(f) \coloneqq \int_{-\infty}^{\infty} f(x) e^{-2\pi i \xi x} \,\mathrm{d}x, \tag{2.49}$$

$$f(x) = \mathcal{F}^{-1}(F) \coloneqq \int_{-\infty}^{\infty} F(\xi) e^{2\pi i \xi x} \,\mathrm{d}\xi. \tag{2.50}$$

The integrals can be approximated using a discrete Fourier transform with the advantage of some efficient computing algorithms such as Fast Fourier Transform. The discrete Fourier transform of an N-element array f_n is defined as

$$F_m = \mathrm{DFT}(f) \coloneqq \sum_{n=0}^{N-1} f_n e^{-2\pi i m n/N}, \tag{2.51}$$

$$f_n = \mathrm{DFT}^{-1}(F) \coloneqq \frac{1}{N} \sum_{m=0}^{N-1} F_m e^{2\pi i m n/N}, \tag{2.52}$$

where both arrays f and F have N elements and the indices m, n go from zero to $N-1$.

The simplest case is considering the integral (2.49) finite and discrete by sampling x in uniform steps δx so that $f_n = f(x_n) = f(n \cdot \delta x)$. Then $\int \ldots \mathrm{d}x \to \sum_n \ldots \delta x$. This discrete transformation is then equivalent to applying the DFT (2.51) with discrete sampling $\delta\xi = (N \cdot \delta x)^{-1}$ of the conjugate variable ξ:

$$F(\xi_m) \approx \mathrm{DFT}(f) \cdot \delta x, \quad \xi_m = \frac{m}{N \cdot \delta x}, \tag{2.53}$$

$$f(x_n) \approx \mathrm{DFT}^{-1}(F) \frac{1}{\delta x}, \quad x_n = n \cdot \delta x. \tag{2.54}$$

Although the expressions above were obtained in an algebraically straightforward way, the correct scaling needs further discussion. Due to the periodicity of complex exponentials, the results of the transformations can be chained. In other words, $F_m = F_{m+kN}$, $k \in \mathbb{Z}$ is valid for (2.53) and identically for f in (2.54). That means that the sampling ranges $X = N \cdot \delta x$, $\Xi = 1/\delta x$ are also the repetition periods of the results. For DFT (2.51), discrete sampling at x_n of the complex exponential $e^{-2\pi i \xi x}$ yields the same numbers as sampling of other exponentials $e^{-2\pi i (\xi \pm \Xi) x}$, because $\Xi x = n$ and the added phase is a multiple of 2π.

From the point of view of DFT being a discrete approximation of the continuous Fourier transform, the sum approximates the integral well only if the functions inside are slow enough relative to the sampling. This needs to be valid for the input function and the Fourier kernel as well. The consideration then resolves the periodicity and the ambiguous question which frequency ξ should the value F_m be assigned to.

As ξ represents the frequency of the Fourier kernel, its samples ξ_m mean that for $m = 0, 1, 2, \ldots$, the period of the kernel is $X, X/2, X/3, \ldots$. Figure 2.11 illustrates that for higher frequencies, the DFT actually better represents frequencies that are lower and of opposite sign. This means that instead of ξ going from 0 to Ξ, it is more faithful for it to span the interval $(-\Xi/2, \Xi/2)$.

An additional modification is needed if the input data are sampled with a certain offset $\overline{x}$ so that $x_n = n \cdot \delta x + \overline{x}$. This creates only an extra phase term that can be factored out of the transform. Particularly, the HOM data in section 2.2.4 are sampled symmetrically around zero, which results in the extra exponential in (2.8).

In section 2.2.4, cross-correlation is inverted using a Fourier transform. An explicit discussion of this step is presented here. A common property of a cross-correlation $f \star g \coloneqq \int f(x')^* g(x' + x)\,\mathrm{d}x'$ is

$$\mathcal{F}(f \star g) = \mathcal{F}(f)^* \cdot \mathcal{F}(g). \tag{2.55}$$

That means if f is real and

$$c(x) = \int_{-\infty}^{\infty} f(x') f(x' + x)\,\mathrm{d}x', \tag{2.56}$$

$$C(\xi) = |F(\xi)|^2. \tag{2.57}$$

In our case, $f(x)$ is expected to be a real and even function, so its Fourier transform $F(\xi)$ is also real and even. An inversion of (2.57) is therefore possible. In real data, the cross-correlation $c(x)$ is not even. In the case of the HOM dip, statistical and systematic errors are the cause. As a consequence, $C(\xi)$ will not be purely real or positive. That is why the inversion in step (2.9) requires an absolute value as a corrective measure. The inversion builds on the assumption that the input data are reasonably symmetric like an ideal cross-correlation should be. The result presented in Figure 2.9 assumes that the small structures on the side are the artefacts of the errors and that the spectral amplitude is real, even though the numerical result is not. The fact that this result predicts the shape of the HOM dip in Figure 2.8 rather accurately is evidence that these assumptions did not distort the inversion process too much.

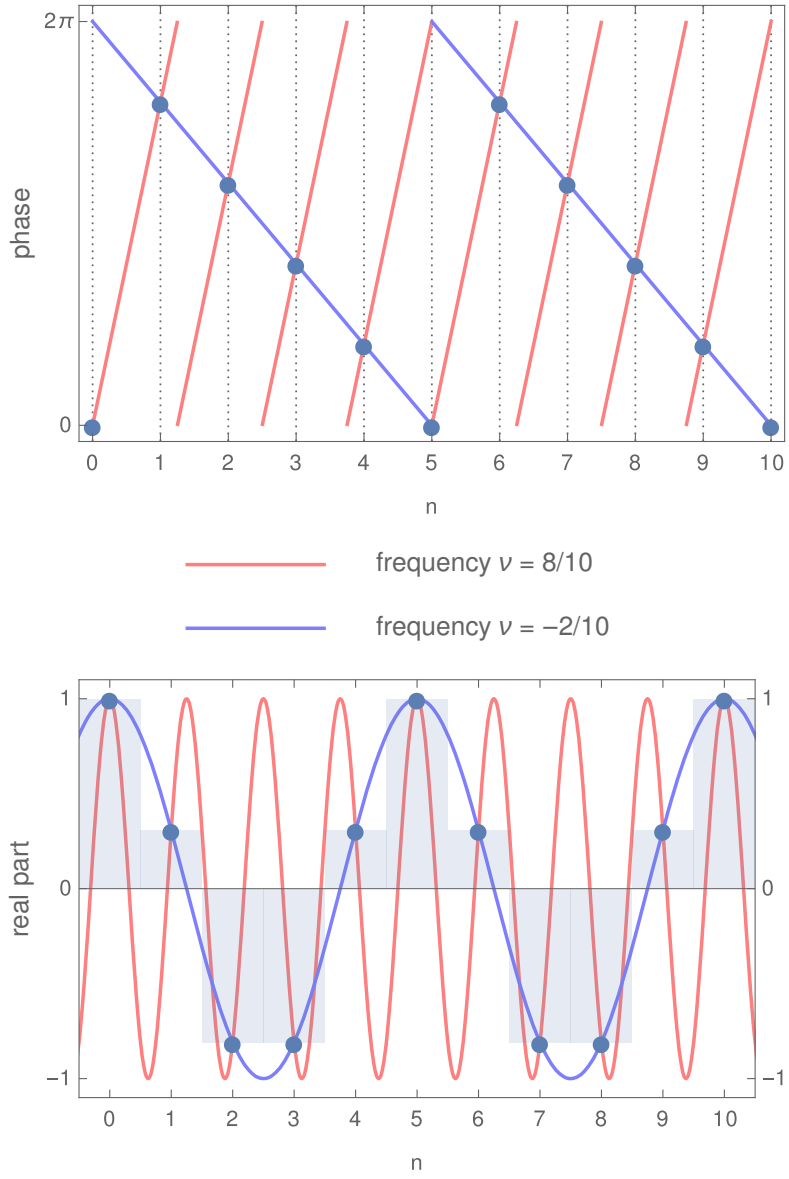

Figure 2.11: Illustration of the phase $\phi = 2\pi\nu n$ (top) and of the real part of $\exp(2\pi i\nu n)$ (bottom) for two different frequencies. The difference between the frequencies is the reverse of the sampling step (one in this case). Blue points are the common samples and the coloured lines represent continuous interpolation. Light blue squares at the bottom show the integral contribution of the point samples in the DFT sum. This matches the continuous integral of the slower blue curve much better than the red. Analogous argument can be made for the imaginary part and so for the complex exponential. Therefore, the DFT serves as the best approximation of the continuous Fourier transform for the frequencies of lowest absolute value.

2.4.2 Statistical errors

Throughout the thesis, error bars are computed by error propagation from basic statistical error of the data. The data are usually governed by either Poisson or binomial distribution. The conventional way of treating these errors is to approximate these discrete probability distributions by a normal distribution. Its standard deviation σ is calculated based on what distribution it is and given as the uncertainty of the measurement. This approach is valid only when normality can be assumed. In such cases, both frequentist and Bayesian definitions of measurement uncertainty converge into the same value that can be calculated from the stochastic model of the data, which is usually known.

The most common example is obtaining a count value $n = n_m$ as a result of a Poissonian process with the mean value μ. The standard deviation of the count variable n is $\sqrt{\mu}$. As the most likely mean value is $\mu = n_m$, the uncertainty is commonly given as $n_m \pm \sqrt{n_m}$. However, this is only valid for $n_m \gg 1$.

Statistical inference offers multiple ways of defining confidence intervals.[123] If the real unknown variable is θ, let the probability of obtaining the measured value X be $P(X|\theta)$. As more values are obtained, the resulting histogram of X approaches $P(X|\theta)$. However, the real value θ is unknown and needs to be inferred based on measured values X.

The common frequentist definition is based on the Neyman band construction.[124,B8] In the two-dimensional space of θ and X, for each θ one charts the interval of confidence probability P_c based on $P(X|\theta)$ that is known. This creates a 'confidence band'. If a value X_m is measured as a realization of $P(X|\theta)$, slicing the confidence region along $X = X_m$ results in a confidence interval. It has the property of containing the real value θ with probability P_c. Explicitly, if a confidence interval is constructed this way for every measurement, it is going to contain θ with a probability P_c. This is valid even if θ keeps changing its value. The advantage of this approach is that it does not require any additional expectations about the real value θ, as opposed to Bayesian approaches that need a prior distribution. The disadvantage is that the property of 'containing the real value with probability P_c' is tied to the *method* of constructing confidence intervals, not their size or position. There is also an ambiguity of where to position the P_c band.

However, the main problem comes with discrete variables. In a Poisson or binomial process, θ is continuous and the results X are discrete. Therefore one cannot construct a Neyman band of confidence P_c, because for every θ, there are only discrete values of P_c achievable – the cumulative probability distribution is discrete. Consequently, the definition needs to be adjusted to 'the confidence interval contains the real value θ with a probability *at least* P_c'. For low discrete values of θ, where the non-normality of $P(X|\theta)$ manifests the most, the construc-

tion of the Neyman band is subject to great ambiguity. Therefore this approach is not used in the thesis.

Another frequentist approach is to evaluate likelihood ratios. Likelihood is by definition $\mathcal{L}(\theta, X) = P(X|\theta)$. If the measured value is X_m and we estimate the real value to be $\theta = X_m$, then the ratio $\mathcal{L}(\theta, X_m)/\mathcal{L}(X_m, X_m)$ signifies how much more (less) probable it is to obtain X_m if θ was the real value, as opposed to getting X_m if X_m was the real value. The likelihood ratio test is best suited for discrete testing, such as comparing two hypotheses. The interpretation in such a case is limiting the probability of getting a false positive given that the reality is negative. For continuous estimation, it is suitable for constructing Neyman bands or regions with similar interpretation.

The Bayesian approach quantifies the answer to a different question: how does a measurement influence our expectation of the real value? The approach therefore requires an additional assumption about the prior expected distribution of the real value θ. Assuming a doubly stochastic measurement would be repeated many times with a given distribution $P(\theta)$ and considering only cases where X_m is measured, one can obtain a posterior probability distribution $P(\theta|X_m)$ from a known likelihood $P(X_m|\theta)$ using the Bayes' theorem

$$P(\theta|X_m) = \frac{P(X_m|\theta)\,P(\theta)}{\int P(X_m|\theta)\,P(\theta)\,\mathrm{d}\theta}. \tag{2.58}$$

The terminology arises from the following reasoning. Before the experiment, one has a *prior* expectation about θ in the form of the distribution $P(\theta)$. After the experiment, one obtains a *posterior* expectation $P(\theta|X_m)$ that is influenced by how *likely* it was to obtain the result X_m given θ.

The posterior offers various ways of constructing confidence intervals.[123] The border values of the interval $[\theta_1, \theta_2]$ clearly need to fulfil $\int_{\theta_1}^{\theta_2} P(\theta|X_m)\,\mathrm{d}\theta = P_c$. The additional condition was elected to be $P(\theta_1|X_m) = P(\theta_2|X_m)$, which for hill-shaped distributions means that the probability density outside of the confidence interval will never be higher than inside, selecting only the most probable values.

This consideration is applied to the data in Figures 3.3, 3.6. The error probabilities are proportional to error counts that can be very low. If the number of counts N_m was measured, it is assumed to be a realization of a Poisson process with an unknown mean $\langle N \rangle = \theta$. This assumption is based on known properties of the signal (SPDC or attenuated laser).

The prior is considered to be uniform so that the confidence interval contains no prior expectations about the measured value. So, for a Poisson process

$$P(\theta|N_m) = \lim_{U\to\infty} \left(\frac{\frac{\theta^{N_m}}{N_m!} e^{-\theta} \cdot \frac{1}{U}}{\int_0^U \frac{\theta^{N_m}}{N_m!} e^{-\theta} \cdot \frac{1}{U}\,\mathrm{d}\theta} \right) = \frac{\theta^{N_m}}{N_m!} e^{-\theta}. \tag{2.59}$$

For normally distributed variables, P_c is usually chosen to cover one standard deviation. The same values is chosen here, so $P_c := (2\pi)^{-1/2} \int_{-1}^{1} e^{-t^2/2} \approx 0.68$. In the special case when $N_m = 0$, the confidence interval is $\theta_1 = 0$ and $\theta_2 = -\ln(1 - P_c)$. Otherwise, numerical solution is needed for the equations

$$Q(N_m + 1, \theta_1) - Q(N_m + 1, \theta_2) = P_c, \tag{2.60}$$

$$\theta_2 - \theta_1 + N_m(\ln \theta_1 - \ln \theta_2) = 0, \tag{2.61}$$

where $Q(n, x)$ is the regularized upper incomplete Gamma function (or cumulative Poisson distribution) also used previously in section 2.3.3. In the approximation of $N_m \gg 1$ and $P_c = 0.68$,

$$\theta_{1,2} \sim N_m \pm \sqrt{N_m} \tag{2.62}$$

The Bayesian approach offers very convenient results; the posterior probability distribution is a direct answer to the question: 'given the result X_m, what would happen if I repeated the experiment many times?' However, it is *an* answer – a different prior would yield a different answer. Sometimes, it is hard to quantify the prior expectation of the real value, because it may be subjective. In the case of Poissonian counts, there is usually some expectation about the order of magnitude. Therefore, it may seem unjustified that the prior is uniform over all values, including the ones that were considered very unlikely before the experiment. Fortunately, the posterior distribution does not depend very much on the expectation of highly unlikely scenarios. This means that one does not have to argue about any borders between likely and unlikely values, and may safely take a uniform distribution over the whole space.

The reason to include this section in the thesis is to explicitly discuss error estimation, which is usually left unmentioned in the field of quantum optics. One often encounters results that exclusively use the formula (2.62) even in cases where it is ill-defined. For example, references 125 and 126 present standard $g^{(2)}(0)$ measurements using the formula (2.22), where the main source of error is always the highest-order-coincidence rate. Presented symmetric confidence intervals like 3 ± 1.5 suggest that, most likely, 4 events were detected and a square root taken. In the second article, confidence intervals span several orders of magnitude, which is hard to believe for any error bar definition. Even intuitively, it is hard to justify expecting a mean value three orders of magnitude lower than what was actually measured, as the probability of obtaining the measurement result would be 10^{-3} at best. In this regard, the error bars in 126 - Figure 2b suggest that this approach was used even for counts averaged over several measurements so that formally $N_m < 0.01$. Admittedly, some of the intervals in reference A1 are of the same kind with $N_m \sim 1$ (corrected here in Figure 3.3).

Chapter 3

Quantum non-Gaussian light

3.1 Introduction

Experimental control over the number of photons is a key issue in quantum optics and quantum information processing.[B9] Namely, photonic Fock states[B10] represent an essential resource that allows harnessing the quantum properties of light. There are several quantum characteristics that such states possess that can be experimentally recognized. Nonclassical states, by definition, go beyond the description of classical optical theory. Any state that cannot be expressed as a statistical mixture of coherent states (displaced vacuum states) is nonclassical.[127,128] One can go a step further and consider a convex mixture of Gaussian states (squeezed and displaced vacuum states). A quantum state incompatible with any such mixture is quantum non-Gaussian.[22] Another common quantum threshold is the negativity of the Wigner function.[21] Fock states exhibit all these properties.

A prominent case is generating a single-photon state $|1\rangle$. Depending on its qualities, a realistic single-photon source will produce a state exhibiting at least one quantum property. The necessary and sufficient condition for nonclassicality is represented by an infinite hierarchy of criteria.[19,129,130] For single photons, the most common and established approach is measuring simultaneous detections after splitting the signal onto two detectors.[20] This approximates to the intensity autocorrelation $g^{(2)}(\tau)$.[B6] A common proof that single photons are generated is $g^{(2)}(0) < 1/2$, where the value is typically close to zero. However, this quantity in itself does not represent a measure of quality, so a lower value does not equal better performance in single-photon applications. To optimize experimental generation, one therefore needs to look for additional quantum features.

Another standard property evaluates the negativity of the Wigner function.[31] As a quantum harmonic oscillator, the radiation field exhibits certain probability

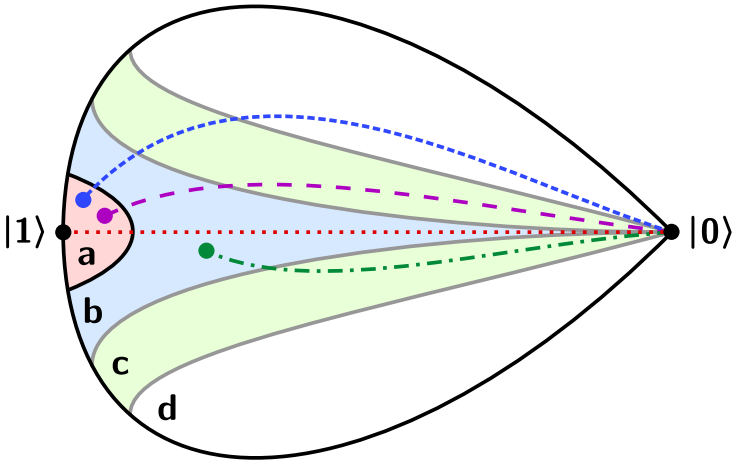

Figure 3.1: The classification of quantum state sets used in the discussion, where **a** ⊂ **b** ⊂ **c** ⊂ **d**. **a** is the set of states with negative Wigner function. All states in the set **b** are guaranteed to be quantum non-Gaussian (QNG). Likewise, all states in the set **c** are nonclassical (NC). The set **d** contains all states in general. Equivalently, all classical states are contained in the complement $\bar{\mathbf{c}}$ and all Gaussian mixtures are in $\bar{\mathbf{b}}$. The borders of **b** and **c** therefore represent QNG and NC witnesses.
The points and non-solid lines represent various realistic quantum states and their respective paths under attenuation. These quantum states can approach vacuum inside different sets. An ideal single-photon state ($P_0\,|0\rangle\langle 0| + P_1\,|1\rangle\langle 1|$, red dotted line) is an extremal case of an infinitely robust QNG state. Other realistic states may exhibit infinite NC depth or leave nonclassical states altogether (dashed lines). The green dot-dashed line represents realistic single-photon states with a positive Wigner function, as generated experimentally.

distributions in canonical variables. The Wigner function represents a global quasi-distribution that, if negative, goes beyond the classical-mechanical view of a phase-space distribution. Naturally, such states are nonclassical as well. The negativity of the Wigner function is a fragile property that will always be lost if optical loss exceeds 50 %; and added noise only further deteriorates the quality. In terms of practical variables like noise, loss or efficiency, there is a significant difference between the border of the Wigner function negativity and the border of nonclassicality. This leaves certain ambiguity in experimental optimization where no particular protocol is specified, especially if reconstructing the whole Wigner function is not possible. In 2011, Filip and Mišta proposed a new property called quantum non-Gaussianity,[22] which can be recognized using the same split-detector setup used for $g^{(2)}$ measurements.[2] Such states are nonclassical, but may possess positive Wigner function. A schematic illustration of the nonclassical sets is shown in Figure 3.1. It was suggested by Lasota, Filip and Usenko[131] that

this property can guarantee quantum key distribution over noisy channels. The following sections report on the works exploring the properties of quantum non-Gaussianity in relation to physical platform, number of photons, optical loss, and excess noise.[A1,A2,A4]

3.2 Single-photon states

This chapter is based on the publication by Straka and colleagues (2014).[A1]

When evaluating the quality of single-photon states, the employed measure is determined by a choice of an application or protocol. Here, a protocol-independent approach is considered, where the main goal is to preserve the quantum properties of ideal single-photon states. Any optical application inevitably includes losses that have significant impact on the results.[132–135] Therefore, it is suitable to quantify maximum tolerable loss in terms of depth. For example, nonclassicality depth is defined as the maximum attenuation of a nonclassical state, at which the state is still able to preserve the nonclassicality.[136,137] To evaluate this definition, one would require a complete homodyne tomography of the state[31] to reconstruct its density matrix in all populated modes.[B11] However, many single-photon states exhibit multi-mode structure, especially heralded single photons are temporally multi-mode due to finite temporal resolution of the detectors. Furthermore, multi-photon noise is present that extends the dimensional requirements of the Hilbert space. Consequently, full reconstruction is practically unfeasible due to its scope.

For contemporary sources of single-photon states, non-classicality (NC) is commonly witnessed by $g^{(2)}(0) \ll 1$.[20,B6] For such states, nonclassicality depth is infinite, because $g^{(2)}$ does not change with attenuation. On the other hand, the depth of the negativity of the Wigner is always very limited. Even an ideal single-photon requires overall loss to be below 50 %. As a consequence, many single photon sources that are characterized using room-temperature photonic detectors cannot reach evidence of this property.

Quantum non-Gaussianity (QNG) is a quantum property that can be recognized in single photons that exhibit a positive Wigner function. There are several ways of witnessing this property[2,22,27,28,138,139] and it has been positively recognized using a number of physical systems.[2,23–25] This work follows the experimental proof by Ježek and colleagues[2] by exploring the properties of QNG depth for various physical platforms. Single photons were produced by frequency conversion of continuous and pulsed light, and recombination of excitons in a semiconductor quantum dot. The split-detector approach allows estimation of a lower bound on the QNG depth. Since the QNG witness works as a sufficient condition, any quantum state beyond the witness may or may not possess QNG. Therefore

the QNG depth is higher or equal to the value corresponding to the witness border.

3.2.1 QNG witnessing

In this subsection, a brief overview will be given of the QNG witness approximation formulated by Lachman and Filip.[A1] In the Fock basis, let P_n denote the probability of n photons. A single-photon state could be considered ideal, if $P_n \equiv 0$ for $n > 1$. So, let $P_{2+} = 1 - P_0 - P_1$ quantify the undesirable multi-photon contribution. If $P_{2+} = 0$, the quantum state would be conclusively QNG. The idea of the QNG witness is to conservatively estimate P_1 and P_{2+} so that they unequivocally prove QNG by passing extremal values of Gaussian mixtures.[2] Such a threshold can be expressed parametrically,[2] but in the limit of a lossy, high-quality single photon sources $P_{2+} \ll P_1 \lesssim 0.1$ an approximation can be used,[26]

$$P_{2+} < \frac{2}{3} P_1^3. \tag{3.1}$$

A nonclassicality condition in the same approximation is $P_{2+} < \frac{1}{2} P_1^2$, which is less strict.[130] To analytically evaluate the QNG depth, let us model a high-quality single-photon state by

$$\rho \approx (1 - P_1 - P_{2+}) \, |0\rangle\langle 0| + P_1 \, |1\rangle\langle 1| + P_{2+} \, |2\rangle\langle 2| \,, \tag{3.2}$$

with the approximation $P_{2+} \ll P_1$. Under these assumptions, the subsequent transmittance necessary to preserve QNG is bounded by

$$T > \frac{3}{2} \frac{P_{2+}}{P_1^3}. \tag{3.3}$$

This proves to be a good estimate for the QNG depth for realistic single photon sources, as evident from the presented data. This figure can be also directly measured using attenuation in the experiment.

3.2.2 Results

In this work, three different systems were used to generate single-photon states. Of these, two were based on spontaneous parametric down-conversion (SPDC) in a nonlinear crystal. The third system was an InAs/GaAs single quantum dot.

The first SPDC source (located in Olomouc) was based on a 2-mm-thick BBO crystal in a type-II collinear configuration that was operated in the continuous-wave (cw) regime. Here, the pump power was 90 mW while its wavelength was

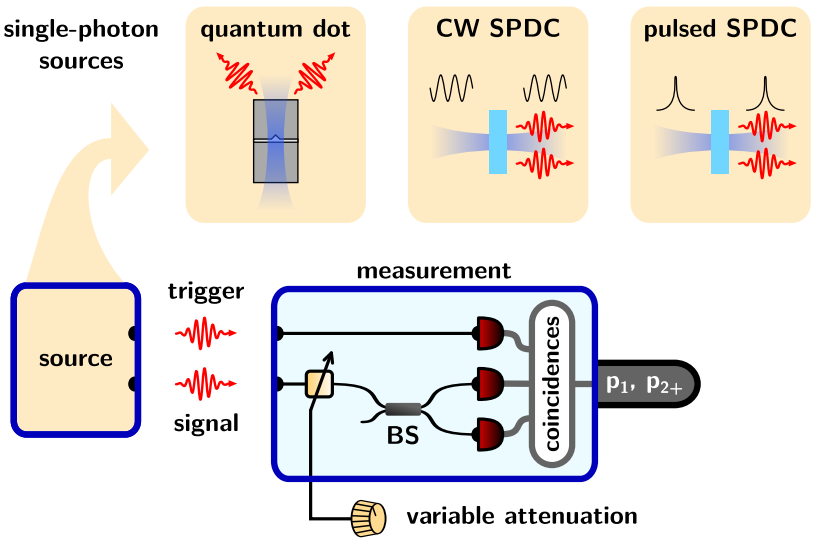

Figure 3.2: The autocorrelation measurement scheme. A single-photon state is heralded by the trigger photon and subjected to attenuation. p_1 and p_{2+} are estimated using the Hanbury Brown–Twiss setup.[2]

405 nm. Correlated photons were spectrally filtered to a bandwidth of 2.7 nm.[1,2] The second SPDC source (located in Innsbruck) produced entangled photon pairs. It contained a 15-mm-long type-II ppKTP nonlinear crystal embedded in a Sagnac-type interferometer loop.[140] This source was pumped by a 2-ps pulsed laser light of 404 nm wavelength and 80 μW power per loop direction. The quantum dot sample contained low density self-assembled InAs/GaAs quantum dots embedded in a planar microcavity. The excitation light was derived from a tunable Ti:sapphire laser that could be operated in picosecond-pulsed (82 MHz repetition rate) or continuous-wave mode.[141] Two data sets were generated with this system, one in resonant two-photon excitation using the pulsed mode and the other in above-band continuous-wave mode.

The measurement scheme was a triggered autocorrelation shown in Figure 3.2. Variable attenuation was introduced by moving a blade in the beam. Data acquisition was carried out by a time-to-digital converter which stored arrival times of every detection event. The trigger detector conditioned the detections in the signal arm: any detection within a coincidence time window centred around a trigger detection was considered a coincidence. From these, the probabilities p_0, p_1, p_{2+} were calculated, which are estimators of P_0, P_1, P_{2+}.[2] These parameters allow constructing the witnesses for NC and QNG states.

In Figure 3.3, the measurement results obtained from all three single-photon sources are compared. Here, the nonclassicality witness $p_{2+} < \frac{1}{2}p_1^2$ is shown

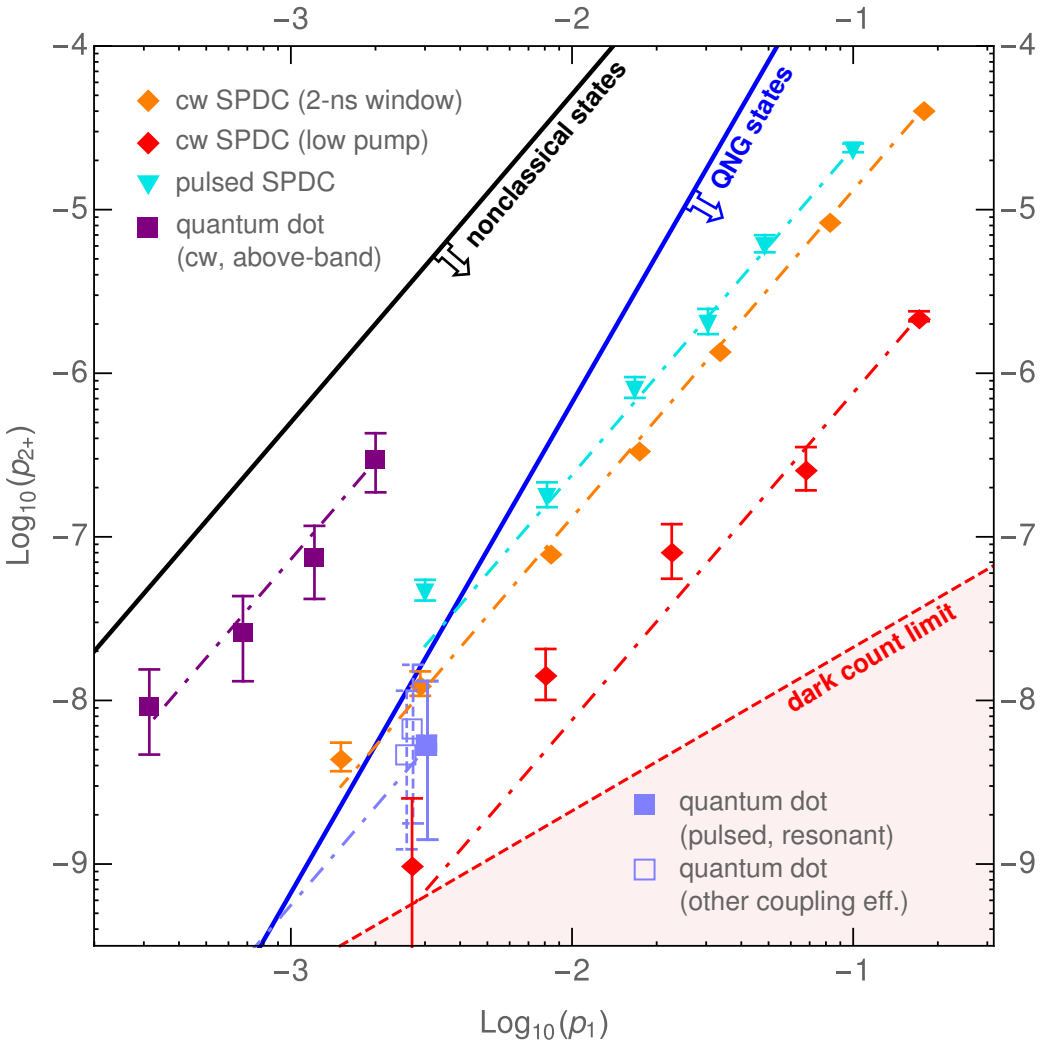

Figure 3.3: Estimated probabilities of heralded single-photon states on a log-log scale. Each series represents various attenuations of a particular state. Full diamonds denote the cw SPDC source: orange – coincidence window 2 ns; red – low pump, coincidence window 2 ns. Cyan triangles denote the pulsed SPDC source. Square markers denote the quantum dot: purple squares – above-band excitation, cw pump; blue squares – resonant excitation, pulsed pump. The dot-dashed lines represent theoretical prediction of attenuation from the initial point. The dashed red line is the limit of dark counts for the red attenuation data. The solid black and blue lines represent NC and QNG witnesses, respectively. Error bars in this figure have been slightly changed with respect to the presentation in reference A1, where a naïve approach was mistakenly used. The change is, however, cosmetic and the results remain unchanged. Here, error bars represent Bayesian 68%-confidence intervals stemming from statistical counting errors. Horizontal error bars are smaller than plot points.

as a solid black line while the QNG witness $p_{2+} < \frac{2}{3}p_1^3$ as a solid blue line. For each single-photon source, the results were obtained under systematically varied attenuation given in units of $10\log_{10}(1-T)$ dB. Additionally, a theoretical model of the induced losses is given (dot-dashed lines). These models served to evaluate the theoretical value of the QNG depth for each source, as given by Eq. (3.3). In addition, experimental confirmation of the QNG character of the states was done by subjecting them to a certain maximum attenuation that is the experimentally proven QNG depth. Since it is challenging to experimentally attenuate the state until it is placed exactly on the border of Gaussian mixtures, the proven QNG depth is always lower than the theoretical prediction.

For the pulsed SPDC source (cyan triangles) the estimated QNG depth is 14.5 dB; the experimentally confirmed value is 10.8 dB. The cw SPDC source measured with 2-ns coincidence window (orange diamonds) yields a theoretical depth of 19.6 dB and a proven depth of 17.9 dB. Red diamonds also stand for the cw SPDC, but with reduced pump power to bring down multi-pair contributions to a level comparable with the quantum dot source. The expected depth is 31.8 dB while the measured value is 18 dB. The most attenuated state also visibly approaches the dark count limit of the detectors and so, further attenuation would be meaningless. The state generated by a quantum dot excited above-band (purple squares) shows only nonclassicality and cannot be well compared to SPDC states. With resonant pulsed excitation (blue square), the quantum dot state exhibits QNG character and the theoretical depth is 5.6 dB. Empty blue squares show additional quantum dot states measured with different collection efficiencies.

3.2.3 Discussion

A prominent feature of the attenuation paths in Figure 3.3 is that both the theoretical models and the directions of the experimental points are parallel to the NC border. In particular, the results demonstrate that even with 2 orders of magnitude of attenuation, the data points exhibit no trend of approaching the NC border. This is due to the identical scaling of the NC witness and respective probabilities under loss, where the higher contributions of $P_{n>2}$ are negligible. Incidentally, these lines also represent the scale of identical $g^{(2)}(0) \approx 2P_2/P_1^2$. This means that all of the presented data remain NC regardless of the attenuation. It also reveals the new scope of QNG depth, which exhibits significant differences in recognizability of quantum properties among states that otherwise have the same $g^{(2)}(0)$. This demonstrates the important aspect of witnesses. Even though $g^{(2)}(0)$ conveniently quantifies the multiphoton error—and is thus widely recognized as a standard of quality for single-photon sources—so does QNG depth.

Therefore, this work offers an alternate approach which evaluates recognizability of quantum features instead of minimizing a certain witness. For conventional single-photon states, NC is routinely recognizable and arbitrarily resilient to optical loss. QNG, however, exhibits a finite depth.

Optimization of the QNG depth can be achieved via certain experimental parameters, depending on the source. These parameters include pump power, the width of the coincidence window, SPDC efficiency and loss. Optical loss in the experimental setup decreases QNG depth for all types of sources. Optimization of the coupling or collection efficiencies is therefore essential, as well as high quantum efficiency of the detectors.

Generally, SPDC QNG depth increases with lower pump power and conversion efficiency. For the cw pump, the coincidence window has an optimum width depending on the detector time resolution. For the pulsed pump, the coincidence window is upper bounded by repetition rate and lower bounded by the photon lifetime and detector time resolution. Moreover, when considering a cw source and a comparable pulsed source, the cw source intrinsically yields higher QNG depth. Single-photon-emitting systems such as semiconductor quantum dots contain no systematic noise, but may suffer from poor coupling efficiency. Increasing this efficiency promises to improve the QNG depth without the need to decrease generation rate, as is the case for SPDC.

3.2.4 SPDC gain

First, SPDC parameters will be discussed. Two regimes were used – pulsed and cw pumping. The statistical model for two-mode SPDC gives the probability of m and n photons $\mathcal{P}(m,n) = \delta_{mn}(1-\gamma)\gamma^n$,[B1] where δ is the Kronecker delta and γ is the overall gain. The gain is responsible for the systematically generated component in the heralded single-photon state, since $p_{2+} \propto \gamma$ for $\gamma \ll 1$. Since the QNG condition dictates $p_{2+} < \frac{2}{3}p_1^3$ and the depth is thus estimated as $T_{\min} = \frac{3}{2}\frac{p_{2+}}{p_1^3}$, γ needs to be minimal. However, the temporal width of the measured state is given by the coincidence window τ. In the cw regime it means that a large number of modes is detected collectively (see section 2.1), resulting in an effective Poisson statistic, where the effective gain is proportional to τ. It follows that the coincidence window needs to be optimized, too. Its width is lower-bounded by the resolution time of the detectors. If the coincidence window is reduced below that limit, it effectively introduces a loss to the state and decreases the QNG depth. On the other hand, if the coincidence window is excessively large, the higher p_{2+} contribution decreases the QNG depth as well. Therefore, there is an optimum coincidence window that maximizes the QNG depth.

3.2.5 Coincidence window

The dependence of measured probabilities on coincidence window depends on the temporal characteristic of each detector. The following analysis assumes a cw pump and identical properties of all detectors. Let us model the jitter of each detector (see section 2.3) by a zero-mean temporal probability distribution $j(t)$ governing the difference between the registered time of detection and the expected time (assuming a highly localised signal). If we consider that a photon in the signal arm is heralded by a detection in the trigger arm, then the time uncertainty is given by a convolution $J(t) = j * j$. Then, given a coincidence window τ, we can express the portion of coincidences that are not lost due to jitter as $\eta_2(\tau) = \int_{-\tau/2}^{\tau/2} J(t)\,\mathrm{d}t$. As a result, $p_1 \propto \eta_2(\tau)$. The main mechanism behind three-fold coincidences contributing to p_{2+} is a photon-pair detection followed by a random background detection on the remaining detector. As the background has uniform occurrence density, the probability of a background detection is proportional to the coincidence window. Overall, $p_{2+} \propto \tau \cdot \eta_2(\tau)$. The experimental dependence of these probabilities is shown in Figure 3.4.

The analysis of the minimum transmittance (3.3), determining the QNG depth, yields $T_{\min} \propto \tau/\eta_2(\tau)^2$. If we assume a symmetric $J(t)$, we may express the extremal condition $J(\tau/2) \cdot \tau = \int_0^{\tau/2} J(t)\,\mathrm{d}t$. If we assume Gaussian jitter with variance $\mathrm{Var}(j) = \sigma^2$, we obtain the optimum for $\tau \approx 4\sigma$.

The data in Figure 3.4 show the cw SPDC for various coincidence windows. The simple analysis assuming Gaussian jitter predicts the value of 0.89 ns. The maximum depth is reached for $\tau = 0.73$ ns, which can be explained by the jitter not being exactly Gaussian and the detection unit having non-uniform clock ticks in the order of 0.1 ns.

The coincidence window plays a minor role in the pulsed regime. There, it has a negligible effect on p_{2+}, assuming the coincidence window is not shorter than the lifetime of the photons and not longer than the delay between pulses. Thus, there is a fixed pump energy contributing in each coincidence window. Analogously to the CW regime, if the coincidence window is shorter than the detector resolution time, the effective loss decreases the QNG depth. Therefore, as long as the coincidence window remains within the aforementioned limits, it has no effect on the QNG depth.

3.2.6 Comparison of cw and pulsed regimes

Let us consider two cases: a cw and a pulsed single-photon source with an identical frequency of heralded state generation – a heralding rate. Let both sources have identical average pump power $\bar{S}$, the same overall conversion effi-

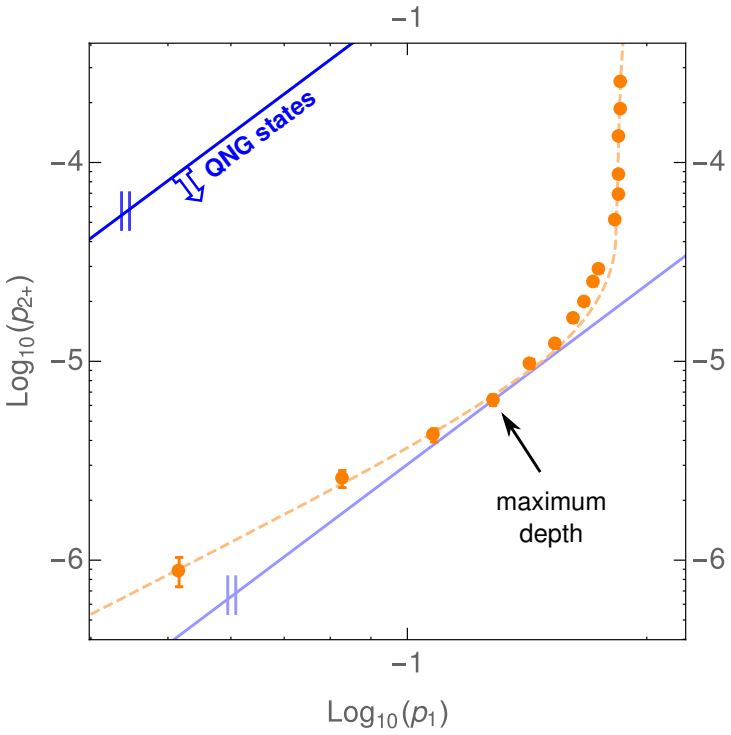

Figure 3.4: Measurement of a cw SPDC single-photon state depending on the coincidence window. Orange points represent the data and the dashed orange line represents a theoretical expectation. Note two asymptotic behaviours – for very small windows, $\eta_2 \propto \tau$ and the state behaves effectively as under attenuation, while for wide windows, $\eta_2 \approx 1$ and only the noise portion increases, $p_{2+} \propto \tau$. The maximum QNG depth is a tangent point.

ciency, number of modes and effective loss in the setup. In the low-gain approximation $g \ll 1$, such two sources would have similar heralding rate and p_1, but different p_{2+}. Namely, the $p_{2+}^{\mathrm{CW}} \approx \mu \bar{S} \tau$ and $p_{2+}^{\mathrm{pul}} \approx \mu \frac{\bar{S}}{\nu}$, where ν is the repetition rate of the pulsed pump, τ is the width of the coincidence window, and μ a common proportionality constant. Since the QNG depth of the heralded state is given by $T_{\mathrm{min}} = \frac{3}{2}\frac{p_{2+}}{p_1^3}$, the ratio of the minimum transmittances $T_{\mathrm{min}}^{\mathrm{CW}}/T_{\mathrm{min}}^{\mathrm{pul}} \approx \tau\nu$. The coincidence window can be minimized to the limit of the detector resolution, typically $\sim 10^{-9}$ s. The repetition rate of the pump laser is not a very flexible parameter ($\sim 10^7$ s^{-1}) and cannot be routinely adjusted. That gives a significant difference in the QNG depth in favor of cw-pumped SPDC sources, assuming similar heralding rates. Furthermore, the cw source often has significantly more modes than the pulsed, which can effectively lead to an additional factor of $\sim \frac{1}{2}$ in $T_{\mathrm{min}}^{\mathrm{CW}}/T_{\mathrm{min}}^{\mathrm{pul}}$. There are ways for pulsed sources to effectively increase

the repetition rate and decrease the p_{2+} contribution.[55] However, for repetition rates approaching detector resolution, the pulsed source would approach the cw source, but would never yield a larger QNG depth.

3.2.7 Quantum dot

A brief discussion of the quantum dot system follows. This part of the experiments was built and measured by the group in Innsbruck (Tobias Huber, Ana Predojević, Gregor Weihs) with samples manufactured by the group of Glenn Solomon.

Quantum dots generate fundamentally different states of light than SPDC. They rely on formation of an electron-hole pair and subsequent recombination that results in photon emission. Specifically, the recombination of the biexciton gives rise to two spectrally distinct photons emitted in a time-ordered cascade. In the presented measurements, the first photon of the cascade serves as a trigger for the second photon. In the case of a resonant excitation by a picosecond laser, only the transition between the vacuum state and a single biexciton is possible. The decay time of the biexciton is two orders of magnitude longer than the pump pulse. Therefore, the probability to systematically generate a multiphoton state by a single pulse is very low. This is an extremely valuable asset, which potentially makes quantum dots much closer to an ideal single-photon source than SPDC.

In practice, however, there is always some background noise present in the measurement, that is responsible for the p_{2+} contribution. The quantum dot state in Figure 3.3 (blue square) shows that this noise is stronger than the noise of an attenuated SPDC single photon (red diamond) operated in the cw regime. The QNG depth can be improved by increasing the collection efficiency.[142,143] As a result, one can expect an increase in p_1 with p_{2+} remaining constant. The three blue-square points in Figure 3.3 show measured states with various degrees of efficiency. If the collection efficiency improves by a factor of 9, the quantum dot would yield states with higher QNG depth than the cw SPDC state. The results presented by Dousse and colleagues[142] indicate that by embedding the quantum dot in a micropillar cavity, one can reach a factor of 16 improvement. For such collection efficiency, the QNG depth may exceed 40 dB and surpass the QNG depth of the SPDC.

3.3 Multiphoton states

This section is based on the publication by Straka, Lachman, and colleagues (2018).[A2]

The QNG criterion discussed in the previous chapter is universal for all quantum states, however it is suitable primarily for recognizing QNG in single-photon states. In this chapter, a multichannel detection scheme will be used to conveniently recognize QNG in multiphoton states.

So far, single-mode multiphoton states have been produced with the maximum of 3 photons in sufficient quality, which was measured in terms of the Wigner function and its negativity.[14,15] Since both cited approaches use optical frequency conversion, the dominant limits here are technical – imperfect optical and detection efficiencies leading both to optical loss and excessive noise present in the quantum state. In contrast to this low number, nonclassical states have been demonstrated up to 50 photons, also using frequency conversion.[144] This work demonstrates QNG states for up to 9 heralded photons, which represents an intermediate tolerance of loss and noise in regard to the cases above.

The two-detector scheme of witnessing QNG proves to be less suitable for higher Fock states due to limited loss tolerance.[30] Therefore, QNG criteria were derived by Lachman and Filip directly for multi-channel detectors.[A2,30] This allows experimental testing of how often n heralded photons are split into $n+1$ detection channels. The result is a hierarchy of criteria formulated for detection probabilities as opposed to estimating photon-number probabilities. The advantage of this approach is that no tomographic or reconstruction techniques are required. Same as before, the additional resilience to loss (QNG depth) of the measured states can be conveniently calculated.

3.3.1 Multiphoton witnesses

This section will briefly define the QNG criteria derived by Lachman and Filip.[A2,30]

The idea of multi-channel detection based on binary detectors is widely applicable in many laboratories.[61,99,101] The detector splits incoming light evenly to multiple separate single-photon binary detectors, as depicted in Figure 3.5. The detector has $n+1$ channels, from which n particular channels are selected. Let us denote the probability of coincident detections on these channels R_n. The probability of all channels registering photons is R_{n+1}. Thus, it is possible to directly witness whether the measured R_n, R_{n+1} are incompatible with any mixture of Gaussian states of light. Such detection technique is not sensitive to phase properties of light and Monte-Carlo simulations suggest that multimode structures of light follow similar extrema (see the supplemental material of reference A2).

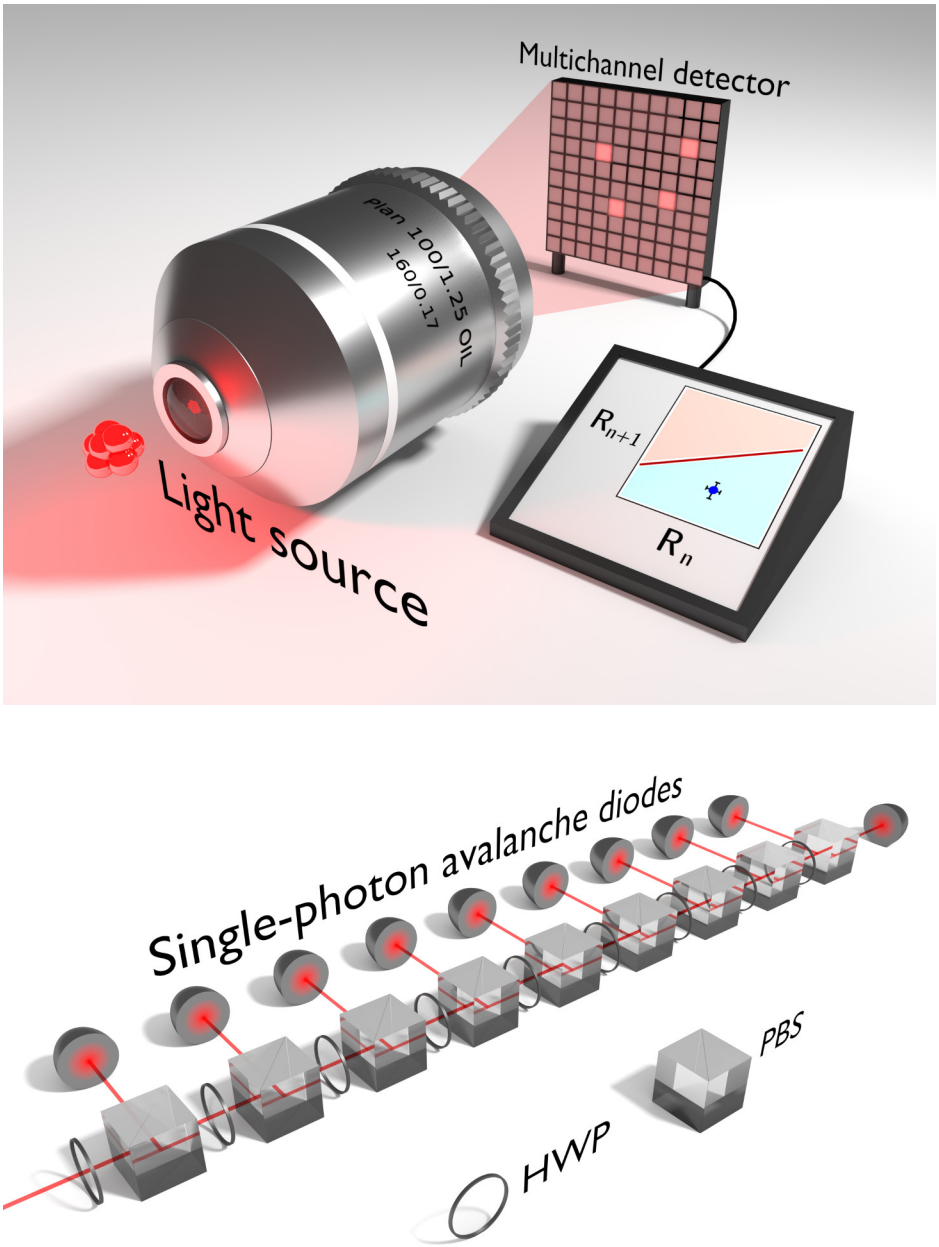

Figure 3.5: A general proposal of the experimental QNG witness. **Top:** multiphoton light is collected and brought to a balanced multichannel detector, where coincidences R_n, R_{n+1} are compared to the QNG threshold. **Bottom:** the detector consists of 10 silicon single-photon avalanche diodes (SPAD) and a balanced array of polarizing beam splitters (PBS) and half-wave plates (HWP) to control the splitting ratio. The half-wave plates can be adjusted to split the light equally to any number of selected channels, so there is no need to physically add or remove SPADs.

Extremal values of R_n, R_{n+1} for Gaussian mixtures can be found numerically.[A2] For light with small mean number of photons, the thresholds can be approximated by an analytical formula

$$(R_n)^{n+2} > H_n^4(x)\left[\frac{R_{n+1}}{2(n+1)^3}\right]^n, \tag{3.4}$$

where $H_n(x)$ is the maximum value of a Hermite polynomial among such values of $x : H_{n+1}(x) = 0$.

3.3.2 Experimental Results

Experimentally, it is very challenging to generate a multi-photon quantum state that would be sufficiently close to a Fock state. Previous efforts have succeeded in generating heralded sub-Poissonian states with a high mean-photon-number.[144–147] However, QNG requires much more than sub-Poissonian light. For such heralded states, the main issue are systematic high-photon-number contributions coupled with optical loss in the trigger channel. The overall efficiency required to generate QNG light would have to be very close to 100 % and thus beyond current technical capabilities. Multi-mode states can overcome these limitations, and still the same QNG criteria apply – if the measurement gives a certain detection statistics, the QNG criterion gives identical results regardless of the number of modes measured. This generalization to multi-mode states can be checked empirically using Monte Carlo simulations (see the supplemental material of reference A2). Multi-mode states were generated that exhibit inherent systematic noise that is weak enough for the states to posses QNG. Single-mode states with the same detection statistics would represent the missing link on the way to Fock states; between nonclassicality and Wigner function negativity.

To achieve this, multiphoton states were produced by mixing n single-photon states together incoherently using time multiplexing. As an additional advantage, this approach simulates incoherent mixing of signals from a cluster of n identical single-photon emitters in separate modes. This is a very relevant topic, because recognizing nonclassical properties of such clusters or simply counting these emitters is subject to ongoing research, which offers limited accuracy.[148–152]

The source of single photons (see section 2.2) was based on collinear type-II spontaneous parametric down-conversion in a periodically poled KTP crystal, which was pumped by a narrow-band continuous-wave laser diode at 405 nm. The heralding rate was set to about 650 kHz, which corresponds to the maximum data flow allowed by the coincidence electronics. It was already shown that such sources generate very high-quality heralded single-photon states.[A1] n successive time windows were taken, in which a single photon was heralded, and were

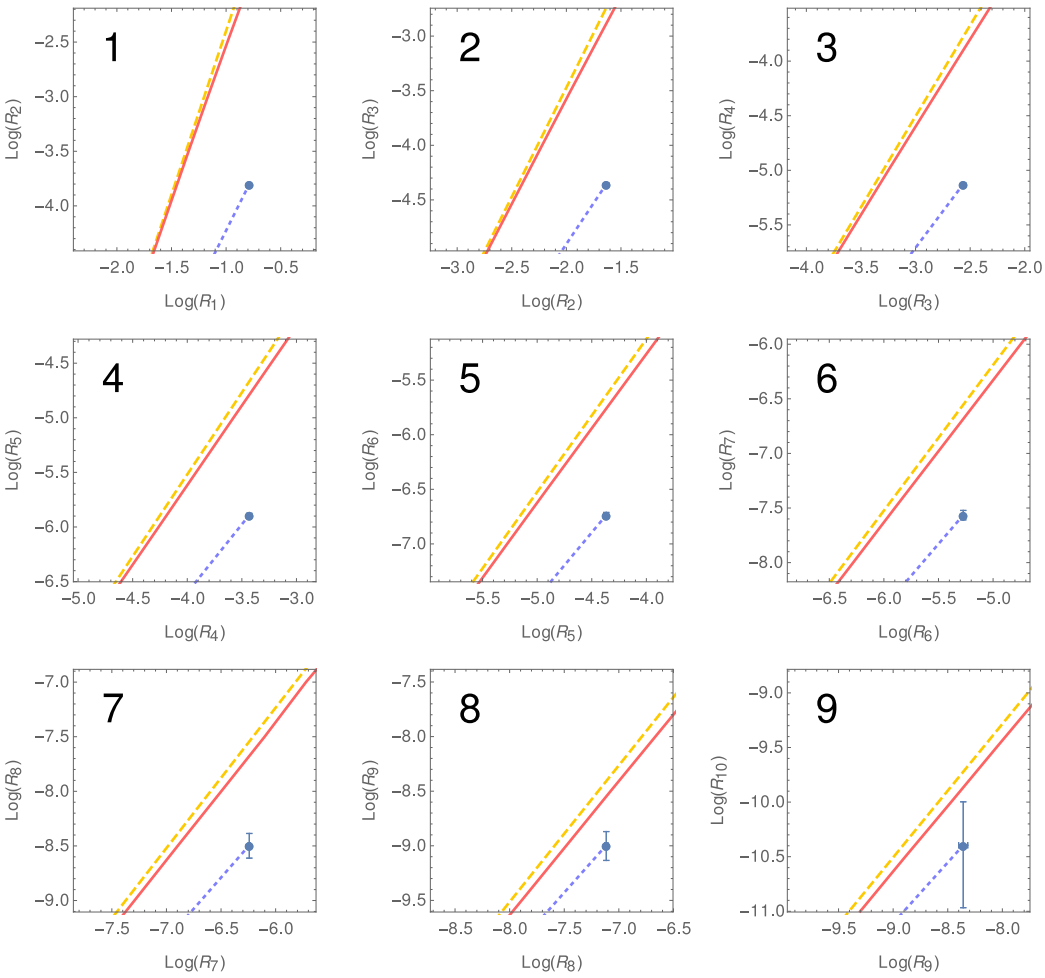

Figure 3.6: QNG thresholds with experimental data for heralded 1-9 photons. The probabilities R_n and R_{n+1} for generated n-photon states were measured on a balanced $(n+1)$-channel detector (blue points for $n = 1-9$). Solid red lines represent the respective QNG criteria, while dashed orange lines are an approximation (Eq. 3.4). Dotted blue lines represent the path of the points if the states become further attenuated. Both vertical and horizontal error bars are shown for all data points; in some cases they are smaller than point size. They represent Bayesian 68%-confidence intervals. These data are also presented in Figure 3.7 with focus on QNG depth. QNG depth values are given in Figure 3.8.

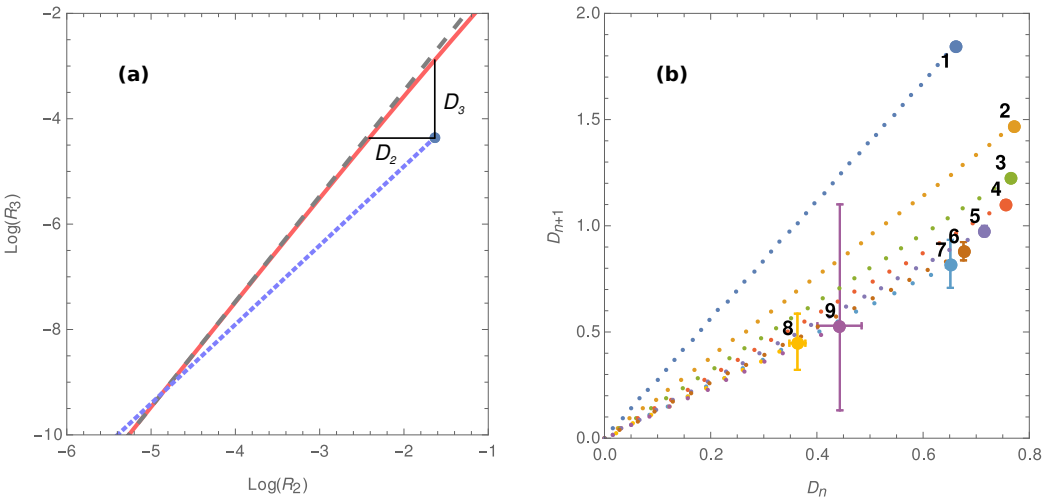

Figure 3.7: QNG tests for heralded 1-9 photons. **(a)** Example for $n = 2$. Red line represents the QNG criterion, while dashed grey line is its approximation (3.4). The blue point represents the measured state and the dotted blue line is the path of the point if the state becomes further attenuated. For the sake of visualising attenuation for all data, let us denote D_n, D_{n+1} as the horizontal and vertical log-distances between a measured point and the QNG threshold. **(b)** The distances D_n and D_{n+1} are plotted for measured points as well as for predicted attenuations. Reaching the point of origin at zero means that QNG is no longer recognizable. Dotted paths represent attenuation with steps of 0.5 dB per dot. Note that these steps are not the same size for all n. The number of steps on each path is proportional to QNG depth. For QNG depth values, see Figure 3.8.

joined into a single temporal detection unit. The positions of these respective time windows were heralded by a detector in one of the SPDC modes. This is equivalent to collecting light from n independent single-photon emitters in n modes. Additionally, the detection statistic of this state is the same as for a single-mode state with equivalent photodistribution. This only requires that all SPADs work in binary mode. To achieve this, if a SPAD registers detections in multiple coincidence windows that are part of one detection mode, it is considered as a single detection only.

A multichannel detector was built by Josef Hloušek; a network of polarizing beam splitters and half-wave plates to construct a balanced 1-to-$(n + 1)$ splitter. The design is equivalent to the one depicted in Figure 3.5, but a tree structure was used instead of a linear one. In each arm, a silicon single-photon avalanche diode (SPAD) was placed as a detector. Even though each SPAD has different efficiency, it is sufficient to adjust the beam splitter network so that the responses of all detectors are balanced. This way, the measured state is merely subjected to additional loss, but that does not create any false positives in QNG witness-

ing.[2] The total number of channels was 10; one SPAD was additionally used as a heralding detector.

Data acquisition employed two time-to-digital converters, each having 8 channels with the resolution of 81 ps/time bin. Since 11 channels were needed in total, two modules were used and synchronized with a shared periodic signal at 100 kHz. This frequency was chosen to compensate the measured relative clock drift 10^5 time bins/second.

The estimated mean numbers of photons were up to 5, if the detector efficiency is taken into account, which was $\approx$ 50%. However, no correction has been done in the data, and the results represent direct witnessing of QNG using a lossy detector. In this regime, witnessing the negativity of the Wigner function would not be possible.

The measured states are very robust against optical loss, withstanding up to 5-20 dB of attenuation before their QNG character becomes undetectable. In previous work, it was demonstrated that this QNG depth can be precisely predicted.[A1] In Figure 3.8, QNG depths of various multi-photon states are shown, as measured using multiple QNG criteria. Here, each multi-photon state is positively detected with at least one order of the QNG criterion.

3.3.3 Discussion

As per (3.4) and shown in Figure 3.6, the QNG borders are approximately linear on a log-log scale with a slope of $(n+2)/n$; the approximation being low mean number of photons. Attenuation paths behave similarly with a slope of $(n+1)/n$, assuming low realistic noise in the sense of fast-decaying photodistribution of the measured state $P_n \gg P_{n+1} \gg \sum_{k=n+2}^{\infty} P_k$. Because the QNG slope is always greater, the two dependencies eventually intersect and quantum states have typically some finite QNG depth. The robustness observed in the data is due to low multiphoton contributions in the single-photon states. When combining n of them, the photodistribution becomes almost binomial with a weak systematic noise, $P_{\leq n} \gg P_{>n}$, and consequently, $R_n \gg R_{n+1}$ for experimental rates. This sharp contrast is necessary for QNG and was the reason for the choice of using multimode heralded single-photon states. These properties are illustrated on detection statistics presented in Figure 3.9.

Generally, if the criterion order is lower than the number of merged single photons (white area in Figure 3.8), the dominant contributions to R_n, R_{n+1} arise from probabilities of heralded generation of $n, n+1$ photons, respectively. These results have a very low uncertainty, but mostly fail to pass the QNG criterion; chiefly due to optical loss.[30] If the criterion order is higher than the number of single photons, these coincidences are always caused by noise with very low de-

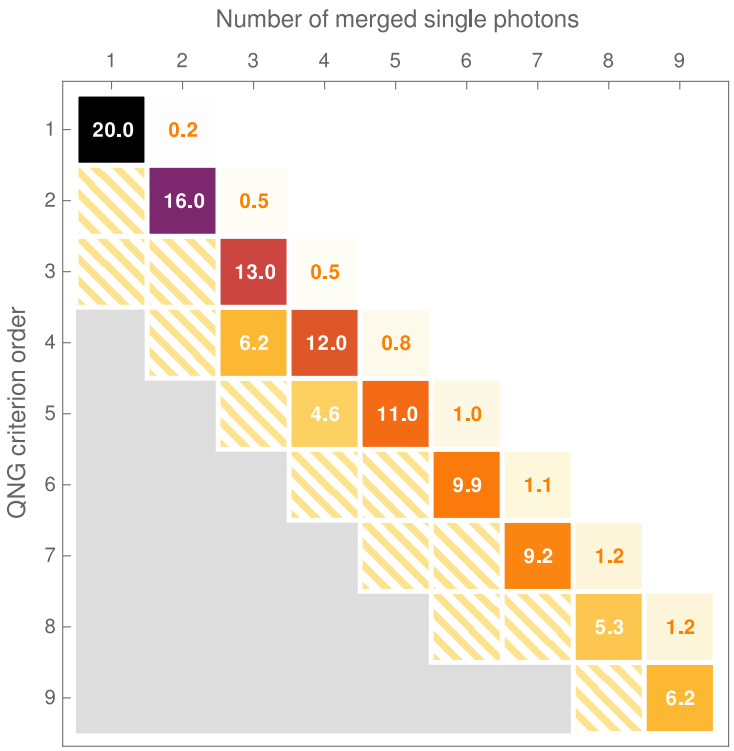

Figure 3.8: Table of QNG depths (in dB). The horizontal axis shows the number of single-photon states that comprise the measured state. The vertical axis represents the order of the QNG criterion used to measure the state (n in equation (3.4)). The diagonal represents the data being shown in Figures 3.6 and 3.7. Solid-colored tiles represent points with positively measured QNG despite statistical uncertainties. For points above the diagonal, the depth estimates are conservative and lower than the actual QNG depth, because R_{n+1} is no longer caused solely by noise. The upper white region represents combinations of measured states and criteria that did not show QNG. Orange stripes denote measurements where statistical uncertainty intersects with the QNG criterion border, making the result inconclusive. Data in the grey region contain no detections at all.

tection rates. Those cases are mostly inconclusive, unless measured for excessively longer periods of time. In between, there is always an optimal criterion that recognizes QNG for the widest range of potential optical loss (the diagonal in Figure 3.8).

This complies well with the initial motivation to test how often n photons cause detections among n and $n + 1$ detectors. Practically, if we consider the measured quantum states as a simulated collective emission from n identical single-photon emitters radiating with the same efficiency, these optima offer a potential way to count the emitters based only on their emission. This hypothesis

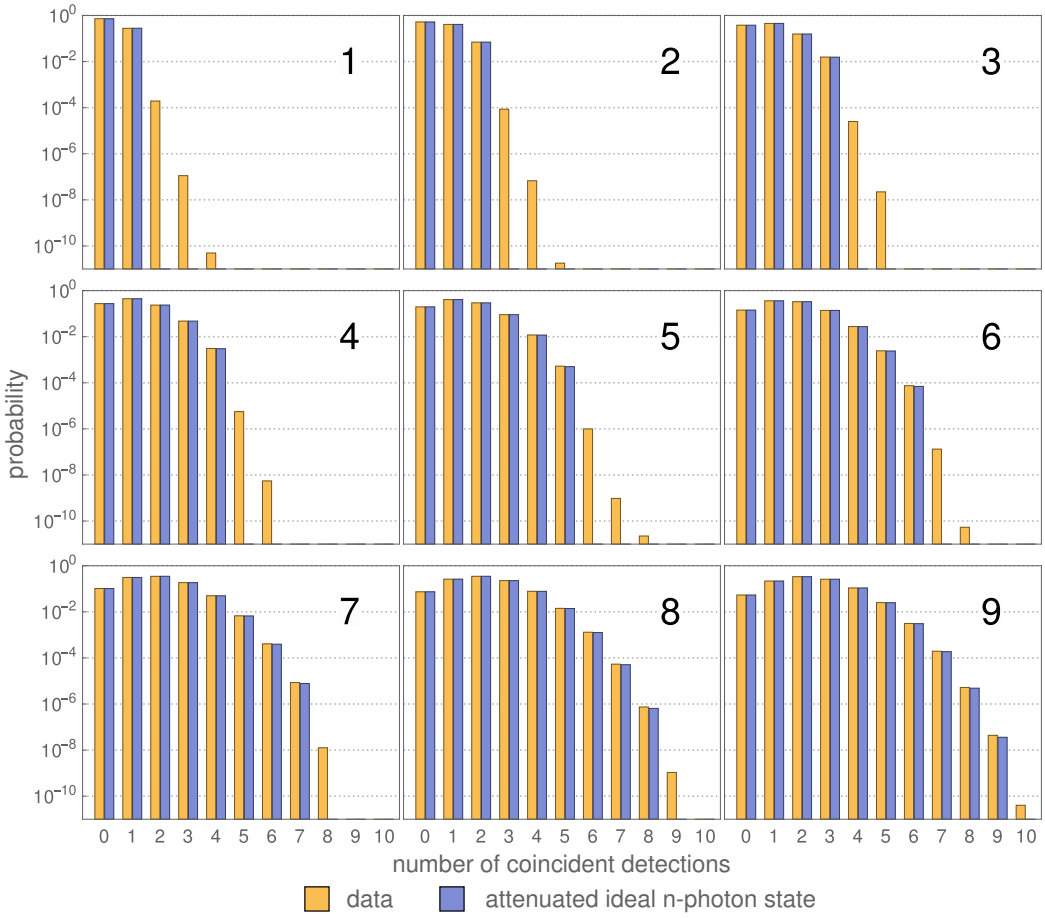

Figure 3.9: Results of measuring multiphoton states on a 10-channel detector. For each heralded number of photons, the probabilities of simultaneous detections are plotted. The measured data are compared to a theoretical model of n photons subjected to optical loss estimated to be 72 %. Thus, the blue data represent the detector response to an ideal binomial distribution. The solitary orange columns represent extra noise caused by small multiphoton contributions present in each constituent single-photon state. This noise is orders of magnitude weaker than the rest of the distribution, which is needed to witness QNG.

would heavily depend on the quality of the single-photon emitters, but the data show that, at least in the presented simulation, QNG depth is capable of accurate distinction for a high number of emitters. Current methodology for counting or resolving individual single-photon emitters also uses multichannel detectors, but has limited accuracy. Results have been published for fluorescent dye molecules[148–150] and for quantum dots.[151,152] It is possible that future measurements will explore this approach further using emission from physical samples.

3.4 Genuine QNG

This section summarizes the results reported by Lachman, Straka, and colleagues (2018).[A4]

So far, quantum non-Gaussian states have borne distinction from Gaussian transformations of vacuum; Gaussian transformations meaning displacement (D) and squeezing (S).[B12] Namely, a QNG state $\rho_{\mathrm{QNG}} \neq \int P(\alpha,\xi)\,|\psi\rangle\langle\psi|_{\alpha,\xi}$, where P is a probability distribution and $|\psi\rangle = S(\xi)D(\alpha)\,|0\rangle$ is a Gaussian state. In section 3.3, a hierarchy of criteria served to distinguish this single property. In contrast, a newly proposed *genuine* n-photon quantum non-Gaussianity – GQNG(n) – represents a hierarchy of quantum properties that rule out any mixtures of Gaussian-transformed superpositions of Fock states up to $n-1$.[A4] Namely, the property of the n^{th} order states that $\rho_n \neq \int P(\psi_n)\,|\psi_n\rangle\langle\psi_n|$, where $|\psi_n\rangle = S(\xi)D(\alpha)\sum_{k=0}^{n-1} c_k\,|k\rangle$.

An important property of GQNG is that it can be both more strict or more lenient than negativity of the Wigner function. In other words, negativity is not sufficient nor necessary for GQNG; and even quantum states with a positive Wigner function may exhibit this property. In fact, using the detection approach from section 3.3, sufficient criteria were formulated for GQNG as well by Lachman and Filip.[A4] They can be found numerically, while for low number of photons the approximation of the n^{th} order reads[A4]

$$R_{n+1} \lesssim \frac{(1+n)^{2n}(2+n)^2(1+n)!R_n^3}{18n^2(n!)^3}. \tag{3.5}$$

The following example illustrates the fine distinction that can be recognized by the GQNG hierarchy. Let us compare three quantum states. The first is an ideal Fock state $|3\rangle$ subjected to optical transmission $T = 0.22$. Such state is GQNG(1,2,3) by definition. The second state, a three-photon state, is a mixture of three high-quality single-photon states, each exhibiting photon-number probabilities $p_1 = 0.22$, $p_2 = 2.4\times10^{-6}$, $p_0 = 1 - p_1 - p_2$. Higher contributions are quickly decaying and can be neglected in this example. This state is modeled

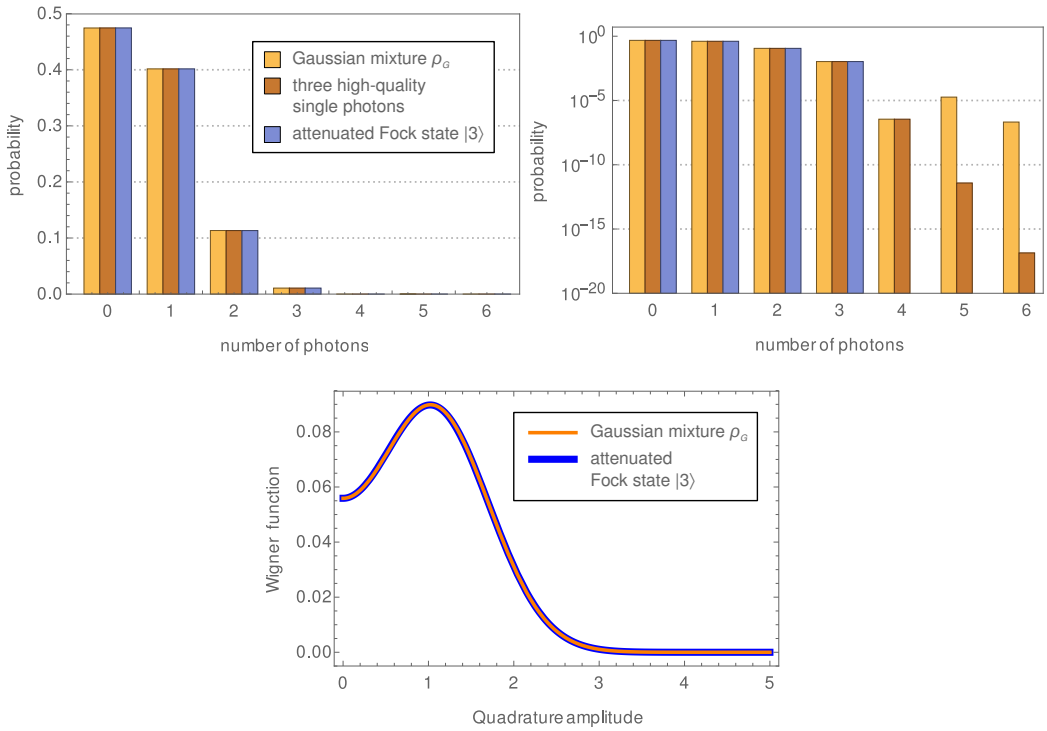

Figure 3.10: Comparison of a Gaussian mixture and genuine quantum non-Gaussian states.

after the data in Figure 3.12 and also exhibits GQNG(1,2,3). The third state is a single-mode Gaussian mixture of $|0\rangle$, $|1\rangle$ and $|2\rangle$, so that the state is *not* GQNG(3) by definition. It is defined by taking $|\phi\rangle = S(\beta)D(\alpha)|2\rangle$ with $\alpha = 0.16747\, e^{i\phi}$ and $\beta = 0.014044\, e^{i\phi}$, randomizing its phase ϕ and mixing it with lower Fock states:

$$\rho_G = 0.47425 \times |0\rangle\langle 0| + 0.39519 \times |1\rangle\langle 1| + 0.13056 \times \frac{1}{2\pi} \int_0^{2\pi} |\phi\rangle\langle\phi|\, \mathrm{d}\phi. \tag{3.6}$$

Figure 3.10 illustrates the differences and similarities among these states. Figures in the top row show the photon-number distributions. The dominant contributions are almost identical. It is the logarithmic plot (top-right sub-figure) that reveals higher contributions, where the difference can be finally seen. Note that the Fock state (blue) is represented by a perfect binomial distribution, while the three-photon state (darker brown) has certain quickly decaying noise contributions.

Their Wigner functions are almost identical as well. This is illustrated in the bottom sub-figure, which is a radial plot of the Wigner function of the attenuated Fock state and the Gaussian mixture. There is a difference between them in the order of $\sim 10^{-4}$. The three-photon state can be presumed to be multimode and therefore cannot be represented by a univariate Wigner function.

The main point of this comparison is that the Gaussian mixture ρ_G is extremely close to a GQNG(3) state in the first five elements of the statistics. It is all the higher contributions that matter, but the difference is very small. This difference serves to witness genuine quantum non-Gaussianity. GQNG can indeed classify quantum states that have been created in entirely different ways, even though their photon statistics and Wigner functions are almost identical. In the presented work, the witness is formulated in terms of detection statistics instead of photon statistics, so it can be measured directly and more reliably.

To witness this property, a multi-mode approach based on SPDC was used, as described in section 3.3. In addition, the sensitivity of genuine QNG to incoherently added noise was explored, which was supplied by an external laser diode. The schematic of the measurement is depicted in Figure 3.11.

The results shown in Figure 3.12 exhibit genuine QNG up to order $n = 3$. This was achieved by reducing SPDC gain (pump power) to a point where multiphoton contributions are sufficiently low, but the overall rate allows measuring statistically significant results over the course of a few hours. While 16 hours of data acquisition were needed for $n = 3$, several months would be needed for $n = 4$. This is because reducing pump power simultaneously decreases the portion of error events and overall generation rate. Such unfavourable scaling of measurement time represents the experimental limit here. Further improvement could be reached by using single-photon detectors with lower jitter, which would decrease the error contribution without affecting generation rate.

The results also provide an insight of how other multiphoton states fare in criteria that do not correspond to their heralded number of photons. In the data, only states with the number of photons higher than the order of the criterion provided statistically significant results. All of these states (numbered points in Figure 3.12) are located outside the genuine QNG witness region.

The results additionally show the effect of an incoherently added noise. In a communication line, such noise could be coupled from external sources and would decrease the recognizability of quantum properties. The noise signal was provided by an attenuated laser diode coupled by an imbalanced beam splitter into the experiment. By controlling the intensity, the portion of additional noise was varied, resulting in a shift along the vertical axis in Figure 3.12. The shift of the points in the horizontal axis is caused by unwanted back-reflections in the optical setup resulting in noise leakage into the heralding arm.

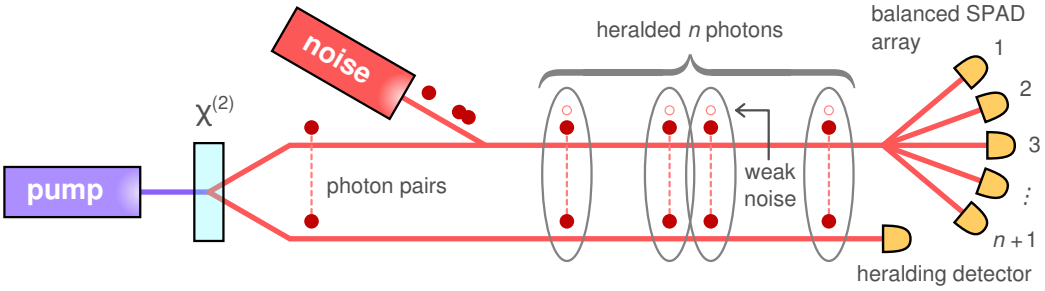

Figure 3.11: A schematic of the measurement. Temporally correlated photon pairs are produced by SPDC in a nonlinear crystal. An attenuated laser beam is incoherently mixed into one of the arms and serves as a source of excess noise. n time windows with heralded single photons are collected and measured on a balanced multichannel detector.

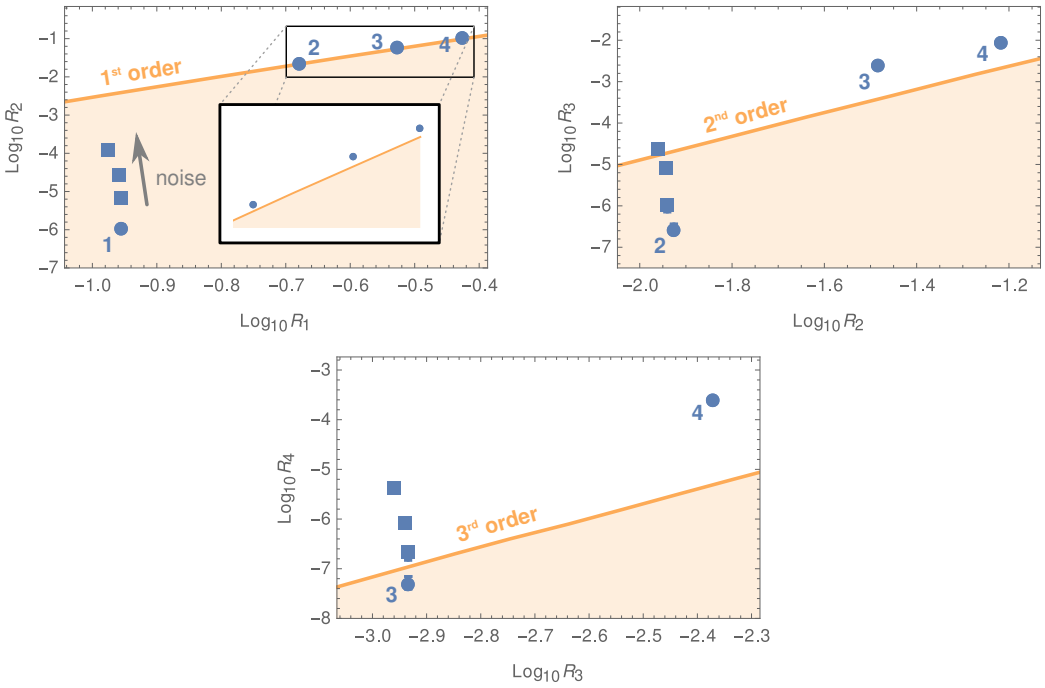

Figure 3.12: Data measured for various number of heralded photons (blue circles) with respect to three orders of genuine QNG (orange regions). All points were measured with identical SPDC parameters, meaning identical single-photon states that constituted the multiphoton states. Estimated depth of genuine QNG for 1–3 heralded photons are respectively 36 dB, 6.3 dB and 0.6 dB. Square points represent added Poissonian noise with mean number of photons $\overline{n} = 4 \times 10^{-5}, 2 \times 10^{-4}, 1 \times 10^{-3}$.

Chapter 4

Generating arbitrary classical photon statistics

This chapter is based on the publication by Straka and colleagues (2018).[A3]

The following work introduces a device based on acousto-optical modulation that can be programmed to perform arbitrary intensity modulation. This can be used as a source of light with programmable photon statistics and also for simulation of transmission fluctuations in communication channels.[71,153–155] Additionally, a new method is proposed to obtain the distribution of optical intensity from an arbitrary photon-number distribution. An experimental demonstration is given, covering several statistics including Poisson, various super-Poisson, thermal, log-normal, bimodal, and uniform distributions. The generated statistics are characterized using a time-multiplexed photon-number-resolving detector and compared with theoretical expectations. Among the demonstrated features are faithful tail behaviour of photon statistics and producing highly bunched light. The proposed generator is also readily extensible to the pulsed regime or other techniques of modulation.

4.1 Photon statistics

Photon statistics in a light beam of constant power follows a Poisson point process.[B1,57] Let us consider a stochastic variable: the number of photons n in a time window of length T, while $\mathcal{P}$ is a constant optical power and E the energy of one photon. It follows that the mean number of photons $\langle n \rangle = \mathcal{P} \cdot T/E$. Also, n follows the Poisson probability distribution $p_n = e^{-\langle n \rangle} \cdot \langle n \rangle^n / n!$. If the optical power $\mathcal{P}$ is a stochastic variable as well, typically changing in time, one has to consider an integrated optical intensity $W(t) \coloneqq \int_t^{t+T} \mathcal{P}(t)/E \, \mathrm{d}t$, a dimensionless

quantity that is governed by a certain probability density $P(W)$. The probability distribution p_n of the number of photons then follows a weighted mixture of Poisson distributions, given by Mandel's formula[57]

$$p_n = \int_0^\infty \frac{W^n}{n!} e^{-W} P(W)\,\mathrm{d}W. \tag{4.1}$$

Mandel's formula covers all possible photon statistics for classical states of light. Generating such statistics can be useful if one needs to simulate classical states with no regard to optical phase. Good examples could be found in practical quantum networks – simulation of optical channels or characterization of single-photon detectors.

In principle, equation (4.1) enables engineering photon statistics p_n by modulating W using a corresponding $P(W)$. This principle is employed by the proposed device based on an acousto-optical modulator (AOM) driven by a harmonic signal, the amplitude/power of which can be digitally controlled (see Figure 4.1). An attenuated continuous optical beam passes through, while the first diffraction order is collected. The system therefore works effectively as a programmable attenuator with a dynamic range exceeding 30 dB and 128 discrete levels of attenuation. These parameters enable spanning a wide range of W with sufficient sampling to generate a wide variety of user-defined photon statistics (see section 4.4).

4.2 Calculating the intensity distribution

If a photon statistics p_n is given instead of the intensity distribution $P(W)$, Mandel's formula needs to be inverted. There are several different approaches found in the literature,[82,84,85,156] but here full inversion to this ill-posed problem is not needed. Both spans for n and W are infinite, but covering infinite ranges is experimentally impossible both on detection and generation side. Therefore, the photon statistics to be generated is always specified up to a certain $n_{\max}$. Because the number of discrete values of intensity W_i is $N_W = 128$ in the experiment, Mandel's formula becomes a linear matrix transformation

$$\sum_{i=1}^{N_W} A_{ni} P_i = p_n \tag{4.2}$$

with $P_i = P(W_i)$ being the probability vector and $A_{ni} = e^{-W_i} W_i^n / n!$ a known transformation matrix. If the right side p_n is given, the task is to find the solution vector P_i.

Let us discuss the properties and dimensions of the problem. There are two additional constraints, the non-negativity of probabilities $P_i \geq 0$ and summing to unity $\sum_i P_i = 1$. The unity condition can be simply added as an additional equation, extending A and p. A strict fulfilment of this equation may be maintained by applying a large weight factor to both sides so that a relatively small residuum contributes significantly to the overall error. The existence of a non-negative solution P is not guaranteed, even though the system of equations is typically underdetermined. In the presented case, the dimensions of the matrix A, including normalization, are $(n_{\max} + 2) \times 128$, where $n_{\max}$ is set between 10 and 15. This formally leads to a highly multi-dimensional sub-space of solutions, where non-negativity may appear like a weak restriction, but it actually intersects the solution sub-space with one orthant of the whole space ($1/2^{128}$). Whether or not there is an intersection is neither likely nor trivial to evaluate for high dimensions. To illustrate the geometry, one can imagine intersecting one octant in a three-dimensional space with a plane, a line or a point, which would depend on their orientation and position and is by no means likely even for a hyperplane. Solution depends on the choice of p_n and the character of the transformation A. There is, however, an available degree of freedom in scaling the intensity levels W_i. Experimentally, these are a product of the intensity at the input and the attenuation levels of the AOM system. Although the attenuation levels are fixed, the input power is a free parameter, expressed by the maximum available intensity $W_{\max}$, which is user-scalable and all other intensity levels derive from it. To summarize, the problem has a form

$$\begin{pmatrix} A_{0,1} & \dots & A_{0,N_W} \\ \vdots & \ddots & \vdots \\ A_{n_{\max},1} & \dots & A_{n_{\max},N_W} \\ 1 & \dots & 1 \end{pmatrix} \begin{pmatrix} P_1 \\ P_2 \\ \vdots \\ P_{N_W} \end{pmatrix} = \begin{pmatrix} p_0 \\ p_1 \\ \vdots \\ p_{n_{\max}} \\ 1 \end{pmatrix}, \; P_i \geq 0 \; \forall i. \tag{4.3}$$

The question now is whether finding an approximate solution is sufficient in the case when the precise solution does not exist or cannot be found. In that case, one would have to choose a statistical metric that would define the optimal solution. Later in this work, total-variation distance is used for quantifying the agreement between model and data, but for the generation itself, a physical argument is needed in order to define what constitutes 'the closest photon statistics'. To avoid this ambiguity, only precise solutions are considered. In practical terms, this means an upper limit on $n_{\max}$ and classical photon statistics.

In order to solve a linear system, a Python-implemented non-negative least squares (NNLS) algorithm was used, as published by Lawson and Hanson.[B13] This proved to be an efficient method of finding a precise solution. When defining the photon statistics, $n_{\max}$ was always kept sufficiently low and $W_{\max}$ chosen such

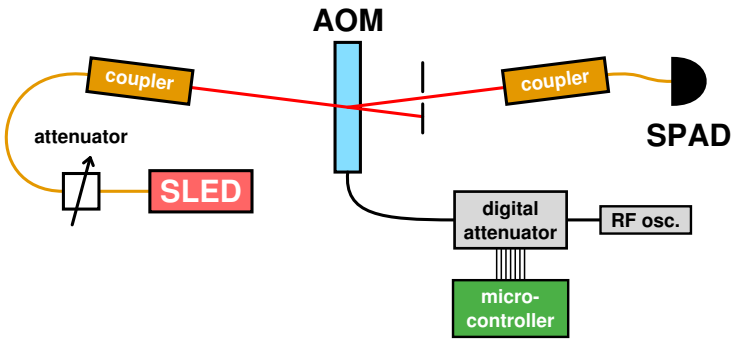

Figure 4.1: The scheme of the generator. Light from a superluminescent diode (SLED) is sent through an acousto-optical modulator (AOM), and the first diffraction order is coupled into a single-mode fibre and detected on a silicon single-photon avalanche diode (SPAD). The AOM is fed from a harmonic signal generator through a programmable attenuator with a parallel 7-bit interface connected to a microcontroller board.

that the solution would be exact within machine precision. Because the matrix rank is $n_{\max} + 2$, the solution vector P_i typically exhibits the same number of non-zero elements. If the condition of precise solutions is relaxed, $n_{\max}$ can be extended at the expense of error. However, in that case minimizing the sum of square differences would have to be justified as a viable metric.

4.3 Experimental implementation

The experimental setup (see Figure 4.1) employed a superluminescent diode due to its long-term power stability better than 10^{-4} (QPhotonics QSDM-810-2). It was centred around 810 nm and coupled to a single-mode fibre. Light was decoupled into free space and sent through an AOM (Brimrose TEM-125-10-800). The first diffraction order was collected into a single-mode fibre and measured. The AOM was driven by a 125-MHz harmonic signal generated in a harmonic signal generator and passed through a digital step attenuator (Mini-Circuits ZX76-31R75PP+). The attenuator was controlled by an ARM microcontroller (Arduino Due) through a 7-bit parallel interface.[157] There were 128 attenuation levels separated by 0.25 dB with a switching speed below 0.5 µs. The specified responses are 300 ns for the attenuator and 150 ns for the AOM. The diffracted optical intensity was approximately linear with respect to the RF signal power.

Detection was performed by a silicon single-photon avalanche diode (SPAD, Excelitas SPCM CD3543H). The width of the detection window T was 10 µs, which is much larger than the recovery time of the SPAD (23 ns), so that the SPAD can distinguish the number of photons incident during the detection win-

dow. Data were collected using an electronic time-to-digital converter with a timing resolution of 156 ps (UQDevices UQD-Logic-16).

The intensity modulation was a stepwise sequence of intensity levels and fully controlled by the microcontroller. The sequence was random with a user-specified statistical distribution implemented by an integrated hardware random number generator. The modulation period was 1 ms, which is much longer than the detection window. Together with fast level switching, the optical intensity in each detection window can be considered constant so that the response of the detector can be modelled. The overall model of the data is then a statistical mixture of constant-intensity models with weights specified by P_i, just like the intensity itself.

The detection model has to take into account all relevant imperfections of the detector.[B3] Some have no impact on the measurement. Finite detection efficiency is simply included in the overall attenuation. Background counts are very low and contribute to an offset in intensity, which is accounted for in calibration. However, the effects of recovery time and afterpulsing have a measurable effect on the detection statistics. The model used here is discussed in section 2.3.2.

All of these effects can be measured, simulated for each intensity W_i and the result compared to measured data. It was found that for constant intensities (Poisson light), the measured photon statistics differs from the predicted model by less than $6 \cdot 10^{-4}$ for each p_n. All of the data that use NNLS inversion have accuracy comparable to this systematic error (for details, see section 4.5).

4.4 Results

Figures 4.2 and 4.3 present various generated photon statistics. Bose-Einstein statistics was chosen for its physical significance; it is the statistics of a single mode of light, which is in thermal equilibrium with its environment. The second important statistics is the log-normal. In this case, the log-normal distribution applies to optical intensity. Such light can occur in turbulent optical channels as the result of log-normal fluctuations of transmittance.[71,154] Finally, some more complex forms of light were chosen – bimodal distributions and a uniform distribution – to demonstrate the variety of statistics that can be realized.

One approach is to take a specified photon statistics p_n and perform the NNLS inversion to obtain an intensity distribution. This inversion-approach is universal and does not require any prior knowledge or decomposition of $P(W)$. The other method (intensity-approach) is simply implementing a given intensity distribution. In that case, both limited dynamic range and finite sampling need to be accounted for. The data show that both approaches can lead to accurate results (see Figures 4.2, 4.3 and Table 4.1). For comparison and more detailed

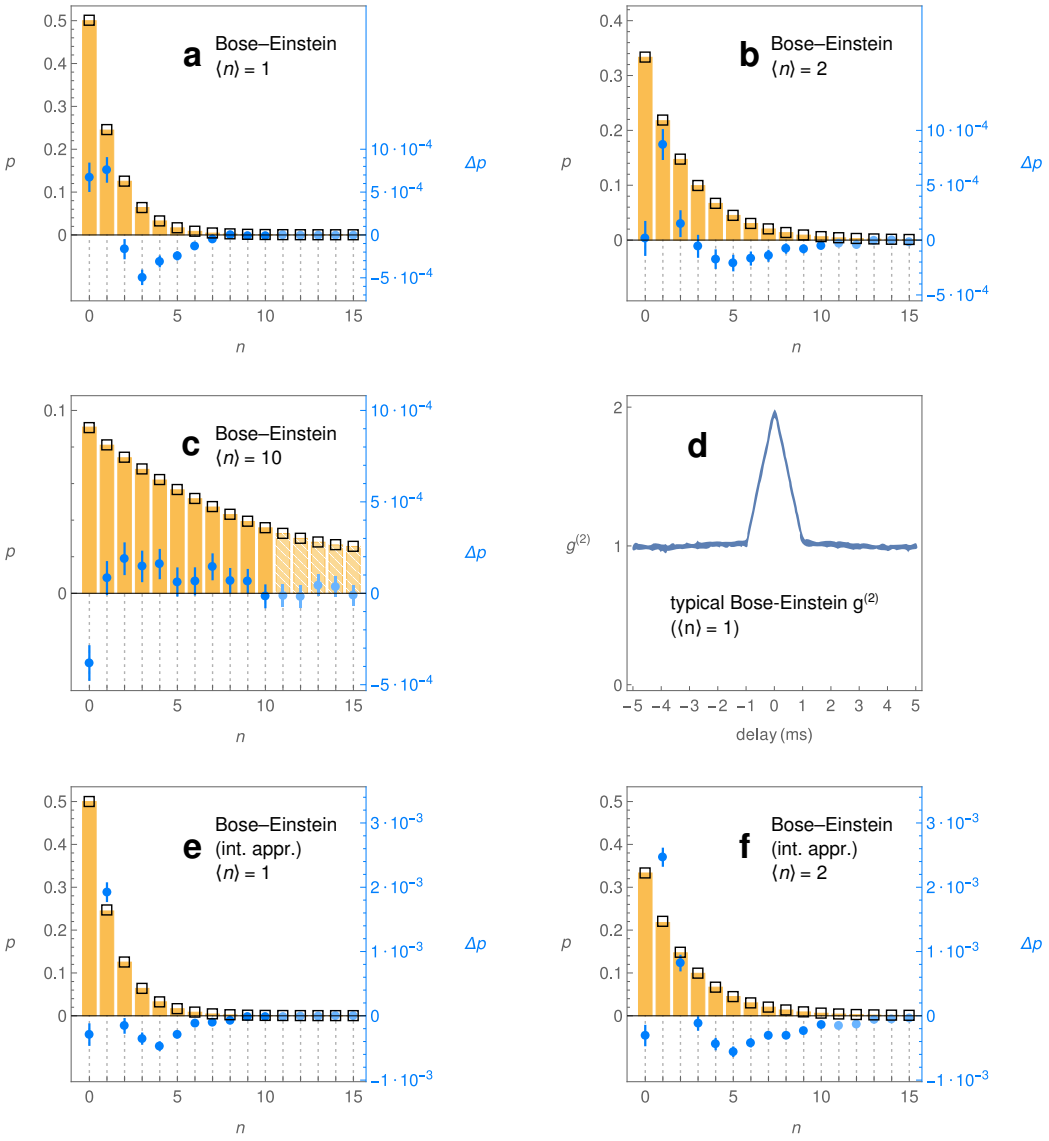

Figure 4.2: Generated Bose-Einstein statistics. Additional information in Table 4.1. Orange bars represent the expected model. Note that the model is not strictly equal to theoretical p_n, because it includes SPAD recovery time and afterpulses. Squares represent measured data. The difference between them, $\delta p = p_{\text{data}} - p_{\text{model}}$, is represented by blue points on a magnified scale. Lighter points and striped bars represent values beyond $n_{\max}$. **a – c:** Bose-Einstein statistics. NNLS was used to calculate $P(W)$. **d:** typical shape of the autocorrelation function $g^{(2)}$. **e, f:** Bose-Einstein statistics. Intensity was modulated with negative exponential distribution.

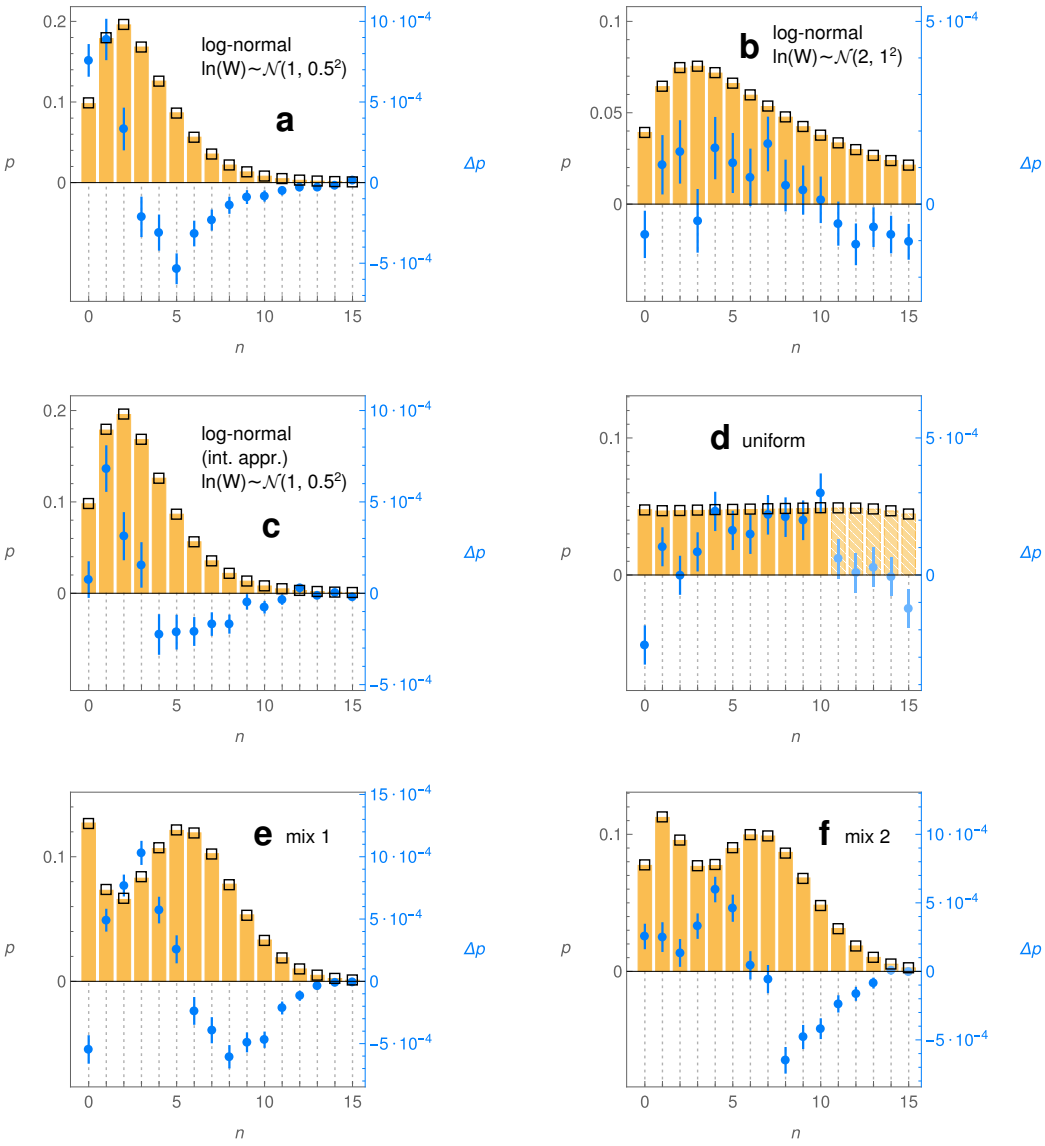

Figure 4.3: Miscellaneous generated photon statistics (continuing from Figure 4.2). Additional information in Table 4.1. For brevity, a normally distributed variable X with mean X_0 and variance σ^2 is denoted as $X \sim \mathcal{N}(X_0, \sigma^2)$. **a, b:** desired statistics are based on log-normal intensity distributions. NNLS inversion was used to calculate $P(W)$. **c:** same as **a**, but using log-normal modulation in intensity. **d:** a uniform distribution $p = 1/21$. NNLS inversion used. **e:** a mixture of 1/4 Bose-Einstein statistics with $\langle n \rangle = 1$ and 3/4 normally convoluted Poisson statistics ($W \sim \mathcal{N}(6, 0.5^2)$). NNLS inversion used. **f:** a mixture of two convoluted Poisson statistics, $W \sim 2/3\ \mathcal{N}(1.5, 0.25^2) + 1/3\ \mathcal{N}(7, 0.25^2)$. NNLS inversion used.

considerations, see section 4.5.

For the measured data, the accuracy of the generated photon statistics needs to be evaluated. A detection model is employed that arises from the intensity statistics $P(W)$ and models the SPAD response to any intensity W. If $P(W)$ was obtained by the inversion-approach, which provides exact solutions up to $n_{\max}$, accurate photon statistics is expected only up to $n_{\max}$. Beyond that, high accuracy of the model is achieved if the photons statistics has already been covered enough, that is if $\sum_{n=0}^{n_{\max}} p_n \to 1$.

To show the difference between model and data, individual differences δp_n are plotted in Figures 4.2 and 4.3. For quantification of the overall difference between the two probability distributions, a very conservative definition was chosen: total-variation distance Δ. It is defined as the maximum difference between probabilities of any possible set of samples $\{n\} \subseteq \mathbb{N}^0$ (for details, see section 4.5). The distances for most photon statistics, and therefore maximal deviations in generated probabilities, are in the order of $\Delta \sim 10^{-3}$ (see Table 4.1).

The first distribution that was measured was the Bose–Einstein distribution: $p_n = \langle n \rangle^n / (\langle n \rangle + 1)^{n+1}$. In theory, it can be generated through negative exponential modulation of the optical intensity $P(W) = \exp(-W/\langle n \rangle)/\langle n \rangle$. For mean values 1 and 2 both approaches were successfully employed. For mean value of 10 and $W_{\max} = 20$, the intensity approach fares much worse due to unfavourable scaling of the intensity range required for optimal modulation (see section 4.5).

Bose-Einstein distribution is also well-known for its photon bunching, as commonly measured by the intensity autocorrelation function $g^{(2)}$. Its value can be calculated from the photon statistics, but also measured using a Hanbury Brown–Twiss setup. The data for one such measurement are shown in Figure 4.2(d). The coincidence window was 10 ns, although this choice does not influence the result as long as the window is much shorter than the modulation period. The $g^{(2)}$ half-width of 1 ms corresponds to the period of modulation and the measured values at zero for both generation methods are within 1.98 ± 0.02 for distributions with $\langle n \rangle = 1, 2$, which are reasonably well covered by the modulation range. For the mean number 10, $g^{(2)}$ drops to 1.6, because too much probability for n beyond $n_{\max}$ is not covered in the NNLS inversion.

The second distribution, the log-normal, is given by $P(W) = \exp[-(\ln W - \Omega)^2/(2\sigma^2)]/(\sqrt{2\pi}\sigma W)$, where $\ln(W)$ is normally distributed with mean Ω and variance σ^2. The corresponding photon statistics can be numerically calculated by applying Mandel's formula (4.1). Here, again, both approaches were used for the mean value $\Omega = 1$.

To demonstrate that complex distributions can be generated, as long as they are classical, two concave and one uniform photon statistics were chosen. The first was given by a combination of Bose–Einstein statistics and normally convo-

luted Poisson statistics. The second is a combination of two convoluted Poisson statistics with two distinct peaks. The third one is a uniform distribution with $\langle n \rangle = 10$, which is peculiar for its apparent non-classicality. Indeed, if specified in full range, $p_{n\leq 20} = 1/21, p_{n>20} = 0$, the distribution is non-classical. However, if uniformity is restricted only to the first 11 elements, the result is a classical photon statistics that is partially uniform with a falling tail for $n > 10$.

Finally, Figure 4.4 shows a log-normal statistics in a scope up to 500 photons with total-variation distance $\Delta = 1.5 \cdot 10^{-2}$. The goal was not to achieve as high precision for all p_n as in previous results, but to demonstrate heavy-tailed scaling of the statistics by comparing measured data to the log-normal. Log-normal modulation was employed in intensity and directly compared the measured photon statistics to the theoretical distribution. The detector response was not accounted for; instead, the detection window was extended to avoid too much saturation.

statistics	quantity	$n_{\max}$	$W_{\max}$	Δ [$\times 10^{-3}$]
B–E(1)	n	10	15	1.4
B–E(1)	W	–	13	1.9
B–E(2)	n	10	15	1.0
B–E(2)	W	–	20	3.3
B–E(10)	n	10	20	0.6
log-$\mathcal{N}(1, 0.5^2)$	n	15	20	2.0
log-$\mathcal{N}(1, 0.5^2)$	W	–	30	1.3
log-$\mathcal{N}(2, 1^2)$	n	15	30	1.4
log-$\mathcal{N}(2, 1^2)$	W	–	500	14.7
$\frac{1}{4}$B–E(1) + $\frac{3}{4}\mathcal{N}(6, 0.5^2)$	n	15	15	3.1
$\frac{1}{3}\mathcal{N}(1.5, 0.25^2) + \frac{2}{3}\mathcal{N}(7, 0.25^2)$	n	13	15	2.1
uniform(0, 20)	n	10	20	1.9

Table 4.1: Results for generated photon statistics. Data shown in Figs. 4.2, 4.3 and 4.4. Quantity denotes the physical quantity specified. For number of photons n, NNLS inversion was used to obtain $P(W)$, and for intensity W, distribution $P(W)$ was given directly. $n_{\max}$ represents the upper limit on the given probability space and $W_{\max}$ is the maximum intensity. Δ is the total-variation distance. Definitions of statistical notations follow. B–E($\langle n \rangle$): Bose–Einstein photon statistics or negative exponential intensity distribution, where $\langle n \rangle = \langle W \rangle$. $\mathcal{N}(\langle W \rangle, \sigma^2)$: normally distributed intensity with mean $\langle W \rangle$ and variance σ^2, or the corresponding photon statistics. log-$\mathcal{N}(\langle \ln W \rangle, \sigma^2)$: log-normal distribution of intensity or the corresponding photon statistics. The moment parameters are the same as for the normal distribution, except here they pertain to $\ln(W)$. uniform(n_1,n_2): uniform photon statistics $p_n = 1/(n_2 - n_1 + 1)$ for $n_1 \leq n \leq n_2$.

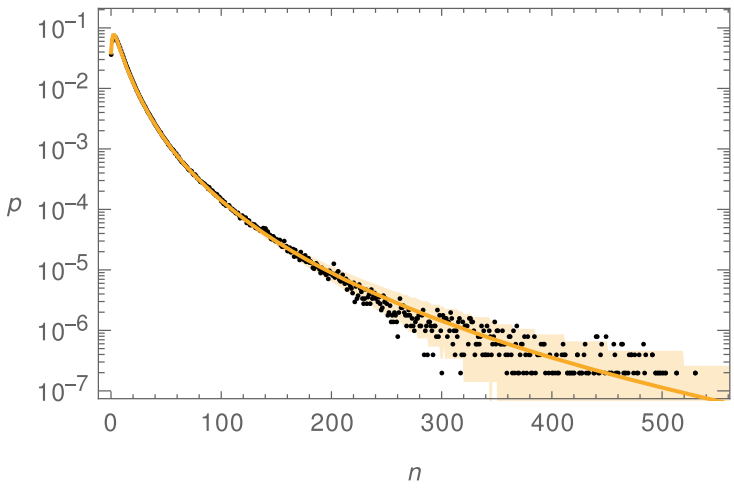

Figure 4.4: Measured log-normal distribution log-$\mathcal{N}(2, 1^2)$ with pronounced heavy-tailed behaviour. Black points denote experimental data and the orange curve is the theoretical expectation. Orange area denotes statistical confidence region of 2σ, so approximately 95 % of all data should be within. For this measurement, the modulation period was 2 ms. The detection window was extended to 200 µs to avoid detector saturation for high photon numbers. Measurement time was 1000 s.

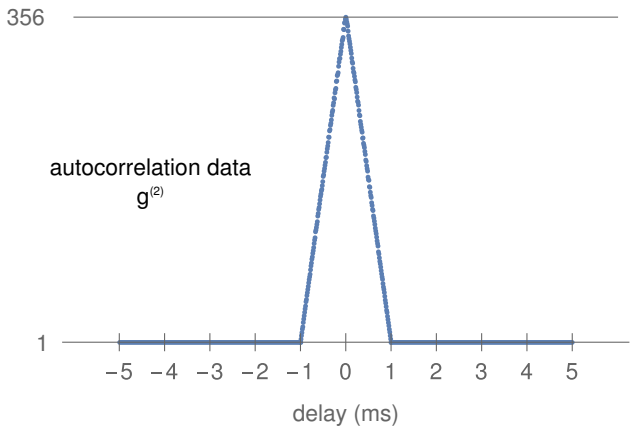

Figure 4.5: The maximum measured autocorrelation value that is achievable using the device in its present form; the result of a two-detector coincidence measurement. Blue curve represents data for a coincidence window of 10 ns, delay values were sampled by 10 µs and the uncertainty is lower than the thickness of the curve. The shape corresponds to stepwise intensity modulation with 1-ms period. The signal was a random mixture of two intensities with count rates on each detector approximately 3 Mcps (probability $p = 6.6 \cdot 10^{-4}$) and 2 kcps (probability $1 - p$). The intensities were chosen such that dark counts and recovery time of the detector would have the smallest effect on the superbunching.

4.5 Discussion and methods

Detector counting model

For SPAD calibration, attenuated light of constant intensity emitted by the SLED was used. The data were analysed using a time-tagging module. Recovery time $\tau_R = 23$ ns was directly obtained from interarrival histograms. Afterpulsing probability was obtained for different count rates by subtracting Poisson background from the histograms.[89] The resulting dependence on rate λ was fitted by $P_{\mathrm{AP}}(\lambda) = a + \alpha\lambda$ with the result $a = 0.0235, \alpha = 2$ ns. These values were then used in the model given in section 2.3.2. Figure 4.6 presents the comparison of measured data relative to the model. The systematic deviations beyond statistical confidence can be explained by intensity fluctuations during the measurement. For higher rates, they could also be explained by the actual value of recovery time being lower than what was measured directly from interarrival histograms. This could be caused by variable tardiness of electronic pulses put out by the operating SPAD.[158]

The model of the SPAD assumes only such processes take place in the detector, that depend on the time of only the most recent count event. Apart from recovery time, the effect of afterpulses is covered, including their temporal characteristic and their component that grows linearly with count rate.[B3] This turns out to be accurate in the order of $\delta p \sim 10^{-4}$. It is important to note that no data fitting was performed. All parameters were established by an independent measurement beforehand to create a unified detection model. The outcomes of the model for various statistical distributions were then compared to the respective raw data.

Scope and extensions

The proposed method works with arbitrary form of intensity modulation. Other modulators like electro-optical, electro-absorption or micromechanical can be used. The advantage of the AOM is its stability, repeatability, high dynamic range and relatively fast response. The estimate is that AOMs can reach at least 40 dB of dynamic range and a modulation speed up to several hundred MHz. The repeatability and stability are so high that they are indistinguishable from SLED and coupling stability. Such parameters could not be simultaneously reached using other modulation techniques.

The response speed itself can be further improved by using electro-optical modulation or electro-absorption modulation. Particularly, an early version of the modulation experiment employed an electro-optical integrated Mach-Zehn-

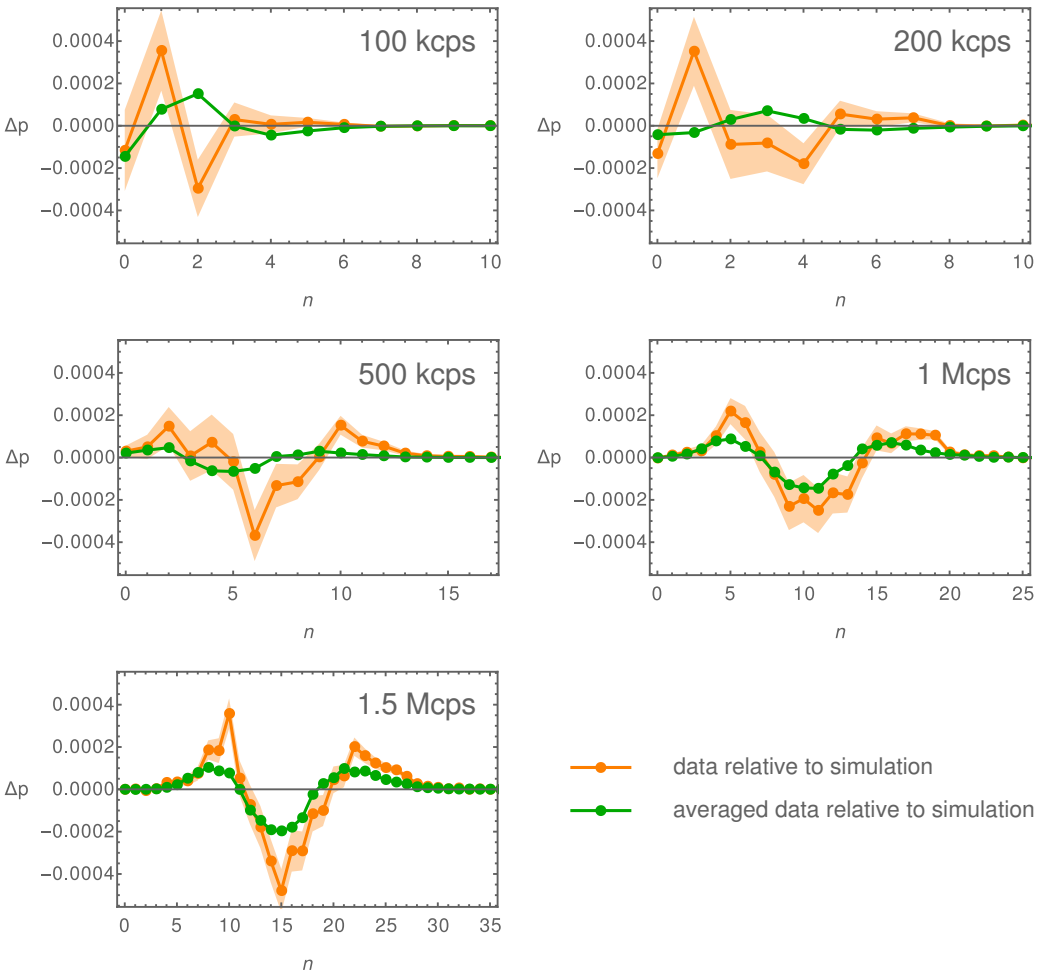

Figure 4.6: The detector model compared to measured data for a constant intensity. The differences in photon-number probabilities between data and a numerical simulation of model (2.23) are plotted in orange including statistical errors of the data. Green points represent simulated data that share the same interarrival time statistics with the measured data. This averages out any fluctuations and for a homogeneous point process, both curves should be identical. However, green points are generally closer to zero than orange points, which suggests the presence of fluctuations either in the signal or in the behaviour of the detector. The parameters of the model were $\tau_R = 23$ ns, $a = 0.0235$, $\alpha = 2$ ns, and λ was taken so that the mean number of detections was the same as in the data. The model is shown to be accurate with deviations in the order of 10^{-4}.

der amplitude modulator.[3] Compared to acousto-optics, this technology offers very high modulation speeds up to 40 GHz, but typically has only about 20 dB of range and poor long-term stability due to interferometric phase drift. However, an active phase lock can be implemented to solve this issue. That would increase modulation speeds necessary for shorter temporal modes.

In the employed generator, dynamic range is limited by the electronics driving the AOM, which can be in principle improved upon. Generally, dynamic range can be augmented using multiple modulators in a sequence. This would enable considerable scaling, increasing the range of the generated photon statistics ($n_{\max}$) by orders of magnitude.

Pulsed regime

The proposed scheme would work the same for pulsed light. Wide wavelength spectrum of the pulsed signal does not represent an issue, as the implemented generator uses a superluminescent diode with 20-nm-wide spectrum. On the detection side, a pulsed-domain photon-number-resolving detector would be required.

In this work, the continuous-wave regime was chosen to demonstrate the accuracy of the proposed generator. This enabled the use of photon-number resolution in time using one SPAD detector, which is accurate and available. Such an approach offers easily scalable detection range up to hundreds of photons with well-understood imperfections like afterpulsing, recovery time, detection efficiency, and dark counts. These either bear no effect or can be directly measured and taken into account. This detection technique can demonstrate the quality of generated statistics, but the same quality can be reached in the pulsed regime.

Speed and timing

There are several important timing parameters: the recovery time τ_R, the temporal width T of the measurement mode, the period of the modulation T_m, and the overall measurement time T_O. They need to be ascending by orders of magnitude, $\tau_R \ll T \ll T_m \ll T_O$. The recovery time is given by the detector, $\tau_R = 23$ ns. $T = 10$ µs was chosen so that the SPAD can recognize the number of detections without too much saturation. The period $T_m = 1$ ms so that the integral intensity $W(t)$ is influenced only by the given modulation statistics $P(W)$ and does not get distorted by modulation transitions too much. The overall measurement time $T_O = 100$ s to gather enough statistical data. During this time, the fluctuations in the input power were not greater than during calibration and are therefore a part of overall systematic error. For pulsed light and fast photon-number-resolving detectors, the sub-500-ns modulation transition limits the pos-

sible repetition rate to 2 MHz, provided pulse-to-pulse-independent statistics is required.

Systematic errors

The systematic errors in the data are caused by systematic errors of the SPAD model and by systematic errors in photon statistics on the generation side. For the inversion-approach, generated p_n are precise, because the intensity levels W_i could be measured directly. Thus, the systematic error is virtually on the detection/calibration side. Consequently, the proposed generator could be potentially used for measuring the response of photon-number-resolving detectors to various photon statistics.

For the approach, where $P(W)$ is given directly on an infinite scale, finite dynamic range of the modulation and discrete sampling do not permit a precise execution, and both sources of systematic error combine. The errors in the respective data conform to this explanation.

Total-variation distance

When measuring the number of photons n, the set of possible outcomes is $\mathbb{N}^0 = \{0, 1, 2, \dots\}$. A photon-number distribution assigns a probability to each individual outcome $n \in \mathbb{N}^0$, and by extension to all sets of outcomes $\{n\} \subseteq \mathbb{N}^0$. The idea is to compare two probability distributions in the broadest possible terms, which means for every set of outcomes. For a certain worst-case set $\{n\}_\Delta$, the difference between probabilities is maximal and thus defined as the total-variation distance Δ. If the individual differences are $\delta p_n = p_{n,\mathrm{data}} - p_{n,\mathrm{model}}$, it follows from additivity of p_n that the maximum difference can be obtained by summing all the positive or all negative differences. These positive and negative sums are equal, because $\sum_n \delta p_n = 0$ due to probability normalization. Therefore, the total variation distance is a simple sum $\Delta = \frac{1}{2}\sum_n |\delta p_n|$. This quantification was chosen because it is a standard statistical measure, it has a straightforward definition and a conservative upper-bound character.

Intensity scaling

For the intensity-approach, there is a degree of freedom in the scale of W within a constant dynamic range. There is an optimum $W_{\max}$ that gives the best match in p_n, and it may vary depending on the definition of statistical distance, but only slightly. The optimal $W_{\max}$ increases with the mean intensity $\langle W \rangle$ much faster than it does for inversion-approach. This is an interesting advantage of

the inversion-approach as compared to explicitly given modulation, because it permits photon statistics engineering for intensities where the detector is less saturated. When using the same $W_{\max}$, the inversion approach gives much better results for higher mean values.

Photon-number correlations

An important insight is provided by splitting the generated light on a balanced beam splitter and evaluating the photon-number correlations between both outputs.[159] Examples of measured correlation coefficients are < 0.001 for Poissonian light, 0.48 for Bose-Einstein light (0.50 in theory), and 0.45 for log-normal light (0.46 in theory). The measured values depend on mean number of photons, beamsplitter balance and detection efficiencies. In theory, the correlation parameter for classical light intensity with mean μ and variance σ^2 is $C = 1/(1 + 2\mu/\sigma^2)$, assuming balanced detection.

Another well-known correlation metric is the autocorrelation function $g^{(2)}$ that can be calculated from the photon-number distribution or directly measured using the same two-way-splitting scheme and evaluating coincidence detections. Using the aforementioned intensity moments, $g^{(2)}(0) = 1 + (\sigma/\mu)^2$. The highest achievable value stems from the dynamic range of the modulation $d = W_{\max}/W_{\min}$, and is then $g^{(2)}(0) = (1 + d)^2/4d$. It can be generated using a statistical mixture of the minimum and maximum intensity. The presented generator was able to reach $g^{(2)}(0) > 350$ (see Figure 4.5).

It should be noted that the finite number of modulation samples (T_O/T_M) introduces a sampling error in the $g^{(2)}(t)$ autocorrelation. For delays $t > T_M$, the correlation should be $g^{(2)}(t) = 1$. However, due to the limited number of samples, the measured value fluctuates. For extremely bunched light, the fluctuations can be significant. For example, in Figure 4.5 the line appears to be at 1, but it is actually below 0.8. Upon zooming in on this region and extending the plotting range to dozens of milliseconds, one would observe frequent triangular fluctuations between significantly different values like 0.8 and 2. Their average value is, however, unity.

Chapter 5

Conclusion

The thesis covers generation of photonic quantum states in two main areas: producing a heralded number of photons and generating arbitrary photon statistics. The results furthermore address detection and characterization of the photonic states by witnessing quantum non-Gaussianity, verifying generated photon statistics and modelling the counting response of single-photon avalanche diodes.

First, multiple single-photon sources were subjected to QNG analysis. The results show very different values of QNG depths among states that are all nonclassical. Although the statistical differences between single-photon states generated by various platforms are known, the results offer new insight into fundamental importance of such differences. The QNG depth offers a way to quantify how resilient these states are in optical applications that involve loss. The resilience is considered in regard to QNG, which is a fundamental quantum property of all Fock states that needs to be maintained among experimentally generated states of sufficient quality. This motivation concerns multiphoton states as well. The results show that multi-mode states generated by SPDC exhibit QNG despite the systematic noise and optical losses present in both generation and detection. The detected photon statistics was found to be very similar to statistics of attenuated Fock states; the extra noise however still limited the recognizability of quantum non-Gaussian properties.

The QNG results were analyzed in terms of experimental parameters. For SPDC, continuous-wave pump was shown to produce lower multiphoton noise than pulsed. There is also an optimal heralding time window maximizing QNG depth that depends on detector characteristics. When compared to a quantum dot, SPDC can generate much more robust states at present, but its noise is fundamentally unavoidable. Additionally, reducing the noise simultaneously reduces the generation rate. Quantum dots are not limited by this trade-off and further improvement of the technical aspects of quantum dot sources could lead to single-photon states more robust than those generated by SPDC.

Heralded multiphoton states were also shown to exhibit genuine n-photon quantum non-Gaussianity, which is tied to a certain maximum number of photons enveloped by Gaussian transformations. Although these states might possess positive Wigner function due to excess optical loss, they exhibit quantum properties that actually go beyond the negativity of the Wigner function. In fact, the presented methodology is capable of recognizing very subtle differences that distinguish vastly dissimilar quantum states like attenuated Fock states $|n\rangle$ and $(n-1)$-photon Gaussian mixtures.

The thesis furthermore presented a generator of arbitrary classical photon statistics than can be fully programmed by the user. Various statistics were generated including Poissonian, super-Poissonian, thermal, and log-normal. Very high generation accuracy $\delta p_n < 10^{-3}$ was reached, which corresponds to the accuracy of the detection mechanism employed. An efficient inversion method was proposed to turn an arbitrary photon statistics into an optical intensity distribution. The concept of the generator can be extended to any form of intensity modulation with possible increases in speed and range of generated statistics by orders of magnitude. The generator can also be straightforwardly used in a pulsed regime to produce single-mode states with given statistics. Another use is stochastic loss modulation to simulate realistic transmission channels. As a purely experimental advance, the proposed method of modulation is capable of putting out bunched light with much higher intensity than the conventional rotating glass approach.

In the course of solving these projects, experimental methods were developed and described in Chapter 2. A source of correlated photon pairs was constructed, characterized and used for the QNG measurements. The counting response of silicon single-photon avalanche diodes was theoretically modelled both analytically and in simulation.

In conclusion, the presented results contribute to methods of generating and characterizing both non-classical and classical light. QNG and genuine QNG witnessing can aid with experimental development of single- and multiphoton sources, where the current state-of-the-art easily satisfies nonclassicality, but is still significantly limited in terms of the Wigner function negativity. The arbitrary-photon-statistics methodology currently represents the most accurate and tunable engineering of photon statistics and can be used to simulate communication channels, calibrate the response of photon-number-resolving detectors, or probe physical phenomena sensitive to photon statistics. The SPAD counting models extend the currently published counting models that are used to predict the measured number of detections as a function of the incident rate. This could also advance detector calibration and inferring the properties of the optical signal based on the measured data.

References

Articles covering the presented results

A1 I. Straka, A. Predojević, T. Huber, L. Lachman, L. Butschek, M. Miková, M. Mičuda, G. S. Solomon, G. Weihs, M. Ježek, and R. Filip:
'Quantum non-Gaussian depth of single-photon states',
Physical Review Letters **113**, 223603 (2014).

A2 I. Straka, L. Lachman, J. Hloušek, M. Miková, M. Mičuda, M. Ježek, and R. Filip:
'Quantum non-Gaussian multiphoton light',
npj Quantum Information **4**, 1 (2018).

A3 I. Straka, J. Mika, and M. Ježek:
'Generator of arbitrary classical photon statistics',
Optics Express **26**, 8998–9010 (2018).

A4 L. Lachman, I. Straka, J. Hloušek, M. Ježek, and R. Filip:
'Faithful hierarchy of genuine n-photon quantum non-Gaussian light',
arXiv:1810.02546 (2018).

Books

B1 L. Mandel and E. Wolf:
Optical coherence and quantum optics,
(Cambridge University Press, 1995).

B2 R. H. Hadfield and G. Johansson:
Superconducting devices in quantum optics,
(Springer, Cham, 2016).

B3 A. Migdall, S. V. Polyakov, J. Fan, and J. C. Bienfang:
Single-photon generation and detection,
(Academic Press, 2013).

B4 R. Boyd:
Nonlinear optics,
Third Edition (Academic Press, 2008).

B5 M. Fox:
Quantum optics: an introduction,
(Oxford University Press, 2006).

B6 R. Loudon:
The quantum theory of light,
Third Edition (Oxford University Press, 2000).

B7 D. L. Snyder and M. I. Miller:
Random point processes in time and space,
(Springer-Verlag New York, 1991).

B8 G. Bohm and G. Zech:
Introduction to statistics and data analysis for physicists,
(Deutsches Elektronen-Synchrotron, 2010).

B9 P. Kok and B. W. Lovett:
Introduction to optical quantum information processing,
(Cambridge University Press, 2010).

B10 D. F. Walls and G. J. Milburn:
Quantum optics,
Second Edition (Springer-Verlag, 2008).

B11 M. Paris and J. Řeháček:
Quantum state estimation,
(Springer-Verlag Berlin Heidelberg, 2004).

B12 A. Ferraro, S. Olivares, and M. G. A. Paris:
Gaussian states in quantum information,
(Bibliopolis, Napoli, 2005).

B13 C. Lawson and R. Hanson:
Solving least squares problems,
Classics in Applied Mathematics (Society for Industrial and Applied Mathematics, 1995).

Articles, proceedings and theses

1 I. Straka:
'Optical frequency conversion and non-classical light generation',
master's thesis (Faculty of Science, Palacký University, Olomouc, 2012).

2 M. Ježek, I. Straka, M. Mičuda, M. Dušek, J. Fiurášek, and R. Filip:
'Experimental test of the quantum non-Gaussian character of a heralded single-photon state',
Physical Review Letters **107**, 213602 (2011).

3 J. Mika:
'Preparing arbitrary statistics of light by intensity modulation',
master's thesis (Faculty of Science, Palacký University, Olomouc, 2017).

4 E. Knill, R. Laflamme, and G. J. Milburn:
'A scheme for efficient quantum computation with linear optics',
Nature **409**, 46 (2001).

5 R. Horodecki, P. Horodecki, M. Horodecki, and K. Horodecki:
'Quantum entanglement',
Reviews of Modern Physics **81**, 865–942 (2009).

6 C. H. Bennett, G. Brassard, C. Crépeau, R. Jozsa, A. Peres, and W. K. Wootters:
'Teleporting an unknown quantum state via dual classical and Einstein-Podolsky-Rosen channels',
Physical Review Letters **70**, 1895–1899 (1993).

7 D. Bouwmeester, J.-W. Pan, K. Mattle, M. Eibl, H. Weinfurter, and A. Zeilinger:
'Experimental quantum teleportation',
Nature **390**, 575 (1997).

8 A. K. Ekert:
'Quantum cryptography based on Bell's theorem',
Physical Review Letters **67**, 661–663 (1991).

9 T. Jennewein, C. Simon, G. Weihs, H. Weinfurter, and A. Zeilinger:
'Quantum cryptography with entangled photons',
Physical Review Letters **84**, 4729–4732 (2000).

10 N. Sangouard, C. Simon, H. de Riedmatten, and N. Gisin:
'Quantum repeaters based on atomic ensembles and linear optics',
Reviews of Modern Physics **83**, 33–80 (2011).

11 I. Afek, O. Ambar, and Y. Silberberg:
'High-NOON states by mixing quantum and classical light',
Science **328**, 879–881 (2010).

12 A. N. Boto, P. Kok, D. S. Abrams, S. L. Braunstein, C. P. Williams, and J. P. Dowling:
'Quantum interferometric optical lithography: exploiting entanglement to beat the diffraction limit',
Physical Review Letters **85**, 2733–2736 (2000).

13 E. Bimbard, N. Jain, A. MacRae, and A. I. Lvovsky:
'Quantum-optical state engineering up to the two-photon level',
Nature Photonics **4**, 243 (2010).

14 M. Cooper, L. J. Wright, C. Söller, and B. J. Smith:
'Experimental generation of multi-photon Fock states',
Optics Express **21**, 5309–5317 (2013).

15 M. Yukawa, K. Miyata, T. Mizuta, H. Yonezawa, P. Marek, R. Filip, and A. Furusawa:
'Generating superposition of up-to three photons for continuous variable quantum information processing',
Optics Express **21**, 5529–5535 (2013).

16 M. Khoshnegar, T. Huber, A. Predojević, D. Dalacu, M. Prilmüller, J. Lapointe, X. Wu, P. Tamarat, B. Lounis, P. Poole, G. Weihs, and H. Majedi:
'A solid state source of photon triplets based on quantum dot molecules',
Nature Communications **8**, 15716 (2017).

17 M. Lasota, R. Filip, and V. C. Usenko:
'Robustness of quantum key distribution with discrete and continuous variables to channel noise',
Physical Review A **95**, 062312 (2017).

18 E. Knill:
'Quantum computing with realistically noisy devices',
Nature **434**, 39 (2005).

19 T. Richter and W. Vogel:
'Nonclassicality of quantum states: a hierarchy of observable conditions',
Physical Review Letters **89**, 283601 (2002).

20 P. Grangier, G. Roger, and A. Aspect:
'Experimental evidence for a photon anticorrelation effect on a beam splitter: a new light on single-photon interferences',
Europhysics Letters **1**, 173 (1986).

21 G. Nogues, A. Rauschenbeutel, S. Osnaghi, P. Bertet, M. Brune, J. M. Raimond, S. Haroche, L. G. Lutterbach, and L. Davidovich:
'Measurement of a negative value for the Wigner function of radiation',
Physical Review A **62**, 054101 (2000).

22 R. Filip and L. Mišta:
'Detecting quantum states with a positive Wigner function beyond mixtures of Gaussian states',
Physical Review Letters **106**, 200401 (2011).

23 M. Ježek, A. Tipsmark, R. Dong, J. Fiurášek, L. Mišta, R. Filip, and U. L. Andersen:
'Experimental test of the strongly nonclassical character of a noisy squeezed single-photon state',
Physical Review A **86**, 043813 (2012).

24 A. Predojević, M. Ježek, T. Huber, H. Jayakumar, T. Kauten, G. S. Solomon, R. Filip, and G. Weihs:
'Efficiency vs. multi-photon contribution test for quantum dots',
Optics Express **22**, 4789–4798 (2014).

25 C. Baune, A. Schönbeck, A. Samblowski, J. Fiurášek, and R. Schnabel:
'Quantum non-Gaussianity of frequency up-converted single photons',
Optics Express **22**, 22808–22816 (2014).

26 L. Lachman and R. Filip:
'Robustness of quantum nonclassicality and non-Gaussianity of single-photon states in attenuating channels',
Physical Review A **88**, 063841 (2013).

27 C. Hughes, M. G. Genoni, T. Tufarelli, M. G. A. Paris, and M. S. Kim:
'Quantum non-Gaussianity witnesses in phase space',
Physical Review A **90**, 013810 (2014).

28 J. Park and H. Nha:
'Demonstrating nonclassicality and non-Gaussianity of single-mode fields: Bell-type tests using generalized phase-space distributions',
Physical Review A **92**, 062134 (2015).

29 L. Happ, M. A. Efremov, H. Nha, and W. P. Schleich:
'Sufficient condition for a quantum state to be genuinely quantum non-Gaussian',
New Journal of Physics **20**, 023046 (2018).

30 L. Lachman and R. Filip:
'Quantum non-Gaussianity from a large ensemble of single photon emitters',
Optics Express **24**, 27352–27359 (2016).

31 A. I. Lvovsky, H. Hansen, T. Aichele, O. Benson, J. Mlynek, and S. Schiller:
'Quantum state reconstruction of the single-photon Fock state',
Physical Review Letters **87**, 050402 (2001).

32 L. J. Wang, C. K. Hong, and S. R. Friberg:
'Generation of correlated photons via four-wave mixing in optical fibres',
Journal of Optics B: Quantum and Semiclassical Optics **3**, 346–352 (2001).

33 L. Podhora, P. Obšil, I. Straka, M. Ježek, and L. Slodička:
'Nonclassical photon pairs from warm atomic vapor using a single driving laser',
Optics Express **25**, 31230–31238 (2017).

34 O. Benson, C. Santori, M. Pelton, and Y. Yamamoto:
'Regulated and entangled photons from a single quantum dot',
Physical Review Letters **84**, 2513–2516 (2000).

35 D. Huber, M. Reindl, S. F. Covre da Silva, C. Schimpf, J. Martín-Sánchez, H. Huang, G. Piredda, J. Edlinger, A. Rastelli, and R. Trotta:
'Strain-tunable GaAs quantum dot: a nearly dephasing-free source of entangled photon pairs on demand',
Physical Review Letters **121**, 033902 (2018).

36 N. Somaschi, V. Giesz, L. De Santis, J. C. Loredo, M. P. Almeida, G. Hornecker, S. L. Portalupi, T. Grange, C. Antón, J. Demory, C. Gómez, I. Sagnes, N. D. Lanzillotti-Kimura, A. Lemaítre, A. Auffeves, A. G. White, L. Lanco, and P. Senellart:
'Near-optimal single-photon sources in the solid state',
Nature Photonics **10**, 340 (2016).

37 C. Kurtsiefer, S. Mayer, P. Zarda, and H. Weinfurter:
'Stable solid-state source of single photons',
Physical Review Letters **85**, 290–293 (2000).

38 D. B. Higginbottom, L. Slodička, G. Araneda, L. Lachman, R. Filip, M. Hennrich, and R. Blatt:
'Pure single photons from a trapped atom source',
New Journal of Physics **18**, 093038 (2016).

39 B. Lounis and W. E. Moerner:
'Single photons on demand from a single molecule at room temperature',
Nature **407**, 491 (2000).

40 S. E. Harris, M. K. Oshman, and R. L. Byer:
'Observation of tunable optical parametric fluorescence',
Physical Review Letters **18**, 732–734 (1967).

41 C. K. Hong, Z. Y. Ou, and L. Mandel:
'Measurement of subpicosecond time intervals between two photons by interference',
Physical Review Letters **59**, 2044–2046 (1987).

42 P. G. Kwiat, K. Mattle, H. Weinfurter, A. Zeilinger, A. V. Sergienko, and Y. Shih:
'New high-intensity source of polarization-entangled photon pairs',
Physical Review Letters **75**, 4337–4341 (1995).

43 P. G. Kwiat, E. Waks, A. G. White, I. Appelbaum, and P. H. Eberhard:
'Ultrabright source of polarization-entangled photons',
Physical Review A **60**, R773–R776 (1999).

44 S. Tanzilli, H. De Riedmatten, H. Tittel, H. Zbinden, P. Baldi, M. De Micheli, D. B. Ostrowsky, and N. Gisin:
'Highly efficient photon-pair source using periodically poled lithium niobate waveguide',
Electronics Letters **37**, 26–28 (2001).

45 K. Sanaka, K. Kawahara, and T. Kuga:
'New high-efficiency source of photon pairs for engineering quantum entanglement',
Physical Review Letters **86**, 5620–5623 (2001).

46 T. Kim, M. Fiorentino, and F. N. C. Wong:
'Phase-stable source of polarization-entangled photons using a polarization Sagnac interferometer',
Physical Review A **73**, 012316 (2006).

47 A. Fedrizzi, T. Herbst, A. Poppe, T. Jennewein, and A. Zeilinger:
'A wavelength-tunable fiber-coupled source of narrowband entangled photons',
Optics Express **15**, 15377–15386 (2007).

48 M. Fiorentino, S. M. Spillane, R. G. Beausoleil, T. D. Roberts, P. Battle, and M. W. Munro:
'Spontaneous parametric down-conversion in periodically poled KTP waveguides and bulk crystals',
Optics Express **15**, 7479–7488 (2007).

49 Y.-H. Kim and W. P. Grice:
'Measurement of the spectral properties of the two-photon state generated via type II spontaneous parametric downconversion',
Optics Letters **30**, 908–910 (2005).

50 W. P. Grice, A. B. U'Ren, and I. A. Walmsley:
'Eliminating frequency and space-time correlations in multiphoton states',
Physical Review A **64**, 063815 (2001).

51 P. G. Evans, R. S. Bennink, W. P. Grice, T. S. Humble, and J. Schaake:
'Bright source of spectrally uncorrelated polarization-entangled photons with nearly single-mode emission',
Physical Review Letters **105**, 253601 (2010).

52 M. Hendrych, M. Mičuda, and J. P. Torres:
'Tunable control of the frequency correlations of entangled photons',
Optics Letters **32**, 2339–2341 (2007).

53 T. Lutz, P. Kolenderski, and T. Jennewein:
'Demonstration of spectral correlation control in a source of polarization-entangled photon pairs at telecom wavelength',
Optics Letters **39**, 1481–1484 (2014).

54 W. P. Grice and I. A. Walmsley:
'Spectral information and distinguishability in type-II down-conversion with a broadband pump',
Physical Review A **56**, 1627–1634 (1997).

55 M. A. Broome, M. P. Almeida, A. Fedrizzi, and A. G. White:
'Reducing multi-photon rates in pulsed down-conversion by temporal multiplexing',
Optics Express **19**, 22698–22708 (2011).

56 G. J. Mendoza, R. Santagati, J. Munns, E. Hemsley, M. Piekarek, E. Martín-López, G. D. Marshall, D. Bonneau, M. G. Thompson, and J. L. O'Brien:
'Active temporal and spatial multiplexing of photons',
Optica **3**, 127–132 (2016).

57 L. Mandel:
'Fluctuations of photon beams and their correlations',
Proceedings of the Physical Society **72**, 1037 (1958).

58 P. Diament and M. C. Teich:
'Photoelectron-counting distributions for irradiance-modulated radiation',
Journal of the Optical Society of America **60**, 682 (1970).

59 A. Schreiber, A. Gábris, P. P. Rohde, K. Laiho, M. Štefaňák, V. Potoček, C. Hamilton, I. Jex, and C. Silberhorn:
'A 2D quantum walk simulation of two-particle dynamics',
Science **336**, 55–58 (2012).

60 A. Luis and L. L. Sánchez-Soto:
'Complete characterization of arbitrary quantum measurement processes',
Physical Review Letters **83**, 3573–3576 (1999).

61 J. S. Lundeen, A. Feito, H. Coldenstrodt-Ronge, K. L. Pregnell, C. Silberhorn, T. C. Ralph, J. Eisert, M. B. Plenio, and I. A. Walmsley:
'Tomography of quantum detectors',
Nature Physics **5**, 27–30 (2009).

62 G. Harder, C. Silberhorn, J. Řeháček, Z. Hradil, L. Mořka, B. Stoklasa, and L. L. Sánchez-Soto:
'Local sampling of the Wigner function at telecom wavelength with loss-tolerant detection of photon statistics',
Physical Review Letters **116**, 133601 (2016).

63 Y. Qu and S. Singh:
'Photon correlation effects in second harmonic generation',
Optics Communications **90**, 111 (1992).

64 K. Y. Spasibko, D. A. Kopylov, V. L. Krutyanskiy, T. V. Murzina, G. Leuchs, and M. V. Chekhova:
'Multiphoton effects enhanced due to ultrafast photon-number fluctuations',
Physical Review Letters **119**, 223603 (2017).

65 A. Jechow, M. Seefeldt, H. Kurzke, A. Heuer, and R. Menzel:
'Enhanced two-photon excited fluorescence from imaging agents using true thermal light',
Nature Photonics **7**, 973 (2013).

66 S. M. H. Rafsanjani, M. Mirhosseini, O. S. Magaña-Loaiza, B. T. Gard, R. Birrittella, B. E. Koltenbah, C. G. Parazzoli, B. A. Capron, C. C. Gerry, J. P. Dowling, and R. W. Boyd:
'Quantum-enhanced interferometry with weak thermal light',
Optica **4**, 487 (2017).

67 Y. Zhai, F. E. Becerra, J. Fan, and A. Migdall:
'Direct measurement of sub-wavelength interference using thermal light and photon-number-resolved detection',
Applied Physics Letters **105**, 101104 (2014).

68 G. Harder, D. Mogilevtsev, N. Korolkova, and C. Silberhorn:
'Tomography by noise',
Physical Review Letters **113**, 070403 (2014).

69 R. S. Bennink, S. J. Bentley, and R. W. Boyd:
'Two-photon coincidence imaging with a classical source',
Physical Review Letters **89**, 113601 (2002).

70 A. Gatti, E. Brambilla, M. Bache, and L. A. Lugiato:
'Ghost imaging with thermal light: comparing entanglement and classical correlation',
Physical Review Letters **93**, 093602 (2004).

71 I. Capraro, A. Tomaello, A. Dall'Arche, F. Gerlin, R. Ursin, G. Vallone, and P. Villoresi:
'Impact of turbulence in long range quantum and classical communications',
Physical Review Letters **109**, 200502 (2012).

72 M. Marconi, J. Javaloyes, P. Hamel, F. Raineri, A. Levenson, and A. M. Yacomotti:
'Far-from-equilibrium route to superthermal light in bimodal nanolasers',
Physical Review X **8**, 011013 (2018).

73 W. Martienssen and E. Spiller:
'Coherence and fluctuations in light beams',
American Journal of Physics **32**, 919–926 (1964).

74 A. Valencia, G. Scarcelli, M. D'Angelo, and Y. Shih:
'Two-photon imaging with thermal light',
Physical Review Letters **94**, 063601 (2005).

75 S. Kuhn, S. Hartmann, and W. Elsäßer:
'Photon-statistics-based classical ghost imaging with one single detector',
Optics Letters **41**, 2863–2866 (2016).

76 Y. Zhou, F.-l. Li, B. Bai, H. Chen, J. Liu, Z. Xu, and H. Zheng:
'Superbunching pseudothermal light',
Physical Review A **95**, 053809 (2017).

77 B. Bai, J. Liu, Y. Zhou, H. Zheng, H. Chen, S. Zhang, Y. He, F. Li, and Z. Xu:
'Photon superbunching of classical light in the Hanbury Brown–Twiss interferometer',
Journal of the Optical Society of America B **34**, 2081–2088 (2017).

78 Y. Zhou, S. Luo, Z. Tang, H. Zheng, H. Chen, J. Liu, F.-l. Li, and Z. Xu:
'Experimental observation of three-photon superbunching with classical light in a linear system',
Journal of the Optical Society of America B **36**, 96–100 (2019).

79 T. Mehringer, S. Oppel, and J. von Zanthier:
'An optical multimode fiber as pseudothermal light source',
Applied Physics B **123**, 200 (2017).

80 H. E. KONDAKCI, A. F. ABOURADDY, and B. E. A. SALEH:
'A photonic thermalization gap in disordered lattices',
Nature Physics **11**, 930 (2015).

81 H. E. KONDAKCI, A. SZAMEIT, A. F. ABOURADDY, D. N. CHRISTODOULIDES, and B. E. A. SALEH:
'Sub-thermal to super-thermal light statistics from a disordered lattice via deterministic control of excitation symmetry',
Optica **3**, 477 (2016).

82 G. BÉDARD:
'Analysis of light fluctuations from photon counting statistics',
Journal of the Optical Society of America **57**, 1201 (1967).

83 C. L. BYRNE, B. M. LEVINE, and J. C. DAINTY:
'Stable estimation of the probability density function of intensity from photon frequency counts',
Journal of the Optical Society of America A **1**, 1132–1135 (1984).

84 C. BYRNE, D. HAUGHTON, and T. JIANG:
'High-resolution inversion of the discrete Poisson and binomial transformations',
Inverse Problems **9**, 39 (1993).

85 J. C. EARNSHAW and D. HAUGHEY:
'Inversion of the Poisson transform using proportionally spaced cubic B-splines',
Review of Scientific Instruments **67**, 4387–4391 (1996).

86 C. J. CHUNNILALL, I. P. DEGIOVANNI, S. KÜCK, I. MÜLLER, and A. G. SINCLAIR:
'Metrology of single-photon sources and detectors: a review',
Optical Engineering **53**, 081910 (2014).

87 S. V. POLYAKOV and A. L. MIGDALL:
'High accuracy verification of a correlated-photon-based method for determining photon-counting detection efficiency',
Optics Express **15**, 1390–1407 (2007).

88 L. COHEN, Y. PILNYAK, D. ISTRATI, N. M. STUDER, J. P. DOWLING, and H. S. EISENBERG:
'Absolute calibration of single-photon and multiplexed photon-number-resolving detectors',
Physical Review A **98**, 013811 (2018).

89 G. HUMER, M. PEEV, C. SCHAEFF, S. RAMELOW, M. STIPČEVIĆ, and R. URSIN:
'A simple and robust method for estimating afterpulsing in single photon detectors',
Journal of Lightwave Technology **33**, 3098–3107 (2015).

90 A. W. ZIARKASH, S. K. JOSHI, M. STIPČEVIĆ, and R. URSIN:
'Comparative study of afterpulsing behavior and models in single photon counting avalanche photo diode detectors',
Scientific Reports **8**, 5076 (2018).

91 M. A. ITZLER, X. JIANG, and M. ENTWISTLE:
'Power law temporal dependence of InGaAs/InP SPAD afterpulsing',
Journal of Modern Optics **59**, 1472–1480 (2012).

92 D. B. Horoshko, V. N. Chizhevsky, and S. Y. Kilin:
'Afterpulsing model based on the quasi-continuous distribution of deep levels in single-photon avalanche diodes',
Journal of Modern Optics **64**, 191–195 (2017).

93 F.-X. Wang, W. Chen, Y.-P. Li, D.-Y. He, C. Wang, Y.-G. Han, S. Wang, Z.-Q. Yin, and Z.-F. Han:
'Non-Markovian property of afterpulsing effect in single-photon avalanche detector',
Journal of Lightwave Technology **34**, 3610–3615 (2016).

94 M. A. Wayne, J. C. Bienfang, and S. V. Polyakov:
'Simple autocorrelation method for thoroughly characterizing single-photon detectors',
Optics Express **25**, 20352 (2017).

95 M. A. Wayne, A. Restelli, J. C. Bienfang, and P. G. Kwiat:
'Afterpulse reduction through prompt quenching in silicon reach-through single-photon avalanche diodes',
Journal of Lightwave Technology **32**, 4097–4103 (2014).

96 M. Stipčević, B. G. Christensen, P. G. Kwiat, and D. J. Gauthier:
'Advanced active quenching circuit for ultra-fast quantum cryptography',
Optics Express **25**, 21861–21876 (2017).

97 P. Eraerds, M. Legré, A. Rochas, H. Zbinden, and N. Gisin:
'SiPM for fast photon-counting and multiphoton detection',
Optics Express **15**, 14539–14549 (2007).

98 E. Pomarico, B. Sanguinetti, R. Thew, and H. Zbinden:
'Room temperature photon number resolving detector for infared wavelengths',
Optics Express **18**, 10750–10759 (2010).

99 D. Achilles, C. Silberhorn, C. Śliwa, K. Banaszek, and I. A. Walmsley:
'Fiber-assisted detection with photon number resolution',
Optics Letters **28**, 2387–2389 (2003).

100 J. Řeháček, Z. Hradil, O. Haderka, J. Peřina, and M. Hamar:
'Multiple-photon resolving fiber-loop detector',
Physical Review A **67**, 061801 (2003).

101 M. J. Fitch, B. C. Jacobs, T. B. Pittman, and J. D. Franson:
'Photon-number resolution using time-multiplexed single-photon detectors',
Physical Review A **68**, 043814 (2003).

102 J. Hloušek, M. Dudka, I. Straka, and M. Ježek:
'Accurate detection of arbitrary photon statistics',
arXiv:1812.02262 (2018).

103 M. Stipčević and D. J. Gauthier:
'Precise Monte Carlo simulation of single-photon detectors',
arXiv:1411.3663 (2014).

104 V. G. Kornilov:
'A statistical description of the non-linearity of photon counts',
Astronomy Reports **52**, 70–78 (2008).

105 J. W. Müller:
'Dead-time problems',
Nuclear Instruments and Methods **112**, 47–57 (1973).

106 C. K. Hong and L. Mandel:
'Theory of parametric frequency down conversion of light',
Physical Review A **31**, 2409–2418 (1985).

107 P. G. Kwiat, P. H. Eberhard, A. M. Steinberg, and R. Y. Chiao:
'Proposal for a loophole-free Bell inequality experiment',
Physical Review A **49**, 3209–3220 (1994).

108 G. D. Boyd and D. A. Kleinman:
'Parametric interaction of focused Gaussian light beams',
Journal of Applied Physics **39**, 3597–3639 (1968).

109 R. S. Bennink:
'Optimal collinear Gaussian beams for spontaneous parametric down-conversion',
Physical Review A **81**, 053805 (2010).

110 J. A. Armstrong, N. Bloembergen, J. Ducuing, and P. S. Pershan:
'Interactions between light waves in a nonlinear dielectric',
Physical Review **127**, 1918–1939 (1962).

111 M. Yamada, N. Nada, M. Saitoh, and K. Watanabe:
'First-order quasi-phase matched LiNbO3 waveguide periodically poled by applying an external field for efficient blue second-harmonic generation',
Applied Physics Letters **62**, 435–436 (1993).

112 M. Neset:
'Design and characterization of entangled photon sources', Czech,
bachelor's thesis (Faculty of Science, Palacký University, Olomouc, 2018).

113 K. Kato and E. Takaoka:
'Sellmeier and thermo-optic dispersion formulas for KTP',
Applied Optics **41**, 5040–5044 (2002).

114 S. Emanueli and A. Arie:
'Temperature-dependent dispersion equations for KTiOPO4 and KTiOAsO4',
Applied Optics **42**, 6661–6665 (2003).

115 M. Fiorentino, C. E. Kuklewicz, and F. N. C. Wong:
'Source of polarization entanglement in a single periodically poled KTiOPO4 crystal with overlapping emission cones',
Optics Express **13**, 127–135 (2005).

116 K. Burns, K. B. Adams, and J. Longwell:
'Interference measurements in the spectra of neon and natural mercury',
Journal of the Optical Society of America **40**, 339–344 (1950).

117 M. Miková:
'Quantum optical experiments focused on quantum information processing',
Ph.D. thesis (Faculty of Science, Palacký University, 2017).

118 R.-B. Jin and R. Shimizu:
'Extended Wiener–Khinchin theorem for quantum spectral analysis',
Optica **5**, 93–98 (2018).

119 R. Hanbury Brown and R. Q. Twiss:
'A test of a new type of stellar interferometer on Sirius',
Nature **178**, 1046 (1956).

120 S. Cova, M. Ghioni, A. Lacaita, C. Samori, and F. Zappa:
'Avalanche photodiodes and quenching circuits for single-photon detection',
Applied Optics **35**, 1956–1976 (1996).

121 V. Kornilov:
'Effects of dead time and afterpulses in photon detector on measured statistics of stochastic radiation',
Journal of the Optical Society of America A **31**, 7–15 (2014).

122 B. I. Cantor and M. C. Teich:
'Dead-time-corrected photocounting distributions for laser radiation',
Journal of the Optical Society of America **65**, 786–791 (1975).

123 R. D. Cousins:
'Why isn't every physicist a Bayesian?',
American Journal of Physics **63**, 398 (1998).

124 J. Neyman:
'Outline of a theory of statistical estimation based on the classical theory of probability',
Philosophical Transactions of the Royal Society of London A **236**, 333–380 (1937).

125 L. Schweickert, K. D. Jöns, K. D. Zeuner, S. F. Covre da Silva, H. Huang, T. Lettner, M. Reindl, J. Zichi, R. Trotta, A. Rastelli, and V. Zwiller:
'On-demand generation of background-free single photons from a solid-state source',
Applied Physics Letters **112**, 093106 (2018).

126 L. Hanschke, K. A. Fischer, S. Appel, D. Lukin, J. Wierzbowski, S. Sun, R. Trivedi, J. Vučković, J. J. Finley, and K. Müller:
'Quantum dot single-photon sources with ultra-low multi-photon probability',
npj Quantum Information **4**, 43 (2018).

127 R. J. Glauber:
'Coherent and incoherent states of the radiation field',
Physical Review **131**, 2766–2788 (1963).

128 H. J. Kimble, M. Dagenais, and L. Mandel:
'Photon antibunching in resonance fluorescence',
Physical Review Letters **39**, 691–695 (1977).

129 T. Kiesel, W. Vogel, V. Parigi, A. Zavatta, and M. Bellini:
'Experimental determination of a nonclassical Glauber-Sudarshan P function',
Physical Review A **78**, 021804 (2008).

130 R. Filip and L. Lachman:
'Hierarchy of feasible nonclassicality criteria for sources of photons',
Physical Review A **88**, 043827 (2013).

131 M. Lasota, R. Filip, and V. C. Usenko:
'Sufficiency of quantum non-Gaussianity for discrete-variable quantum key distribution over noisy channels',
Physical Review A **96**, 012301 (2017).

132 R. URSIN, F. TIEFENBACHER, T. SCHMITT-MANDERBACH, H. WEIER, T. SCHEIDL, M. LINDENTHAL, B. BLAUENSTEINER, T. JENNEWEIN, J. PERDIGUES, P. TROJEK, B. ÖMER, M. FÜRST, M. MEYENBURG, J. RARITY, Z. SODNIK, C. BARBIERI, H. WEINFURTER, and A. ZEILINGER:
'Entanglement-based quantum communication over 144 km',
Nature Physics **3**, 481 (2007).

133 A. FEDRIZZI, R. URSIN, T. HERBST, M. NESPOLI, R. PREVEDEL, T. SCHEIDL, F. TIEFENBACHER, T. JENNEWEIN, and A. ZEILINGER:
'High-fidelity transmission of entanglement over a high-loss free-space channel',
Nature Physics **5**, 389 (2009).

134 E. BIMBARD, R. BODDEDA, N. VITRANT, A. GRANKIN, V. PARIGI, J. STANOJEVIC, A. OURJOUMTSEV, and P. GRANGIER:
'Homodyne tomography of a single photon retrieved on demand from a cavity-enhanced cold atom memory',
Physical Review Letters **112**, 033601 (2014).

135 J.-I. YOSHIKAWA, K. MAKINO, S. KURATA, P. VAN LOOCK, and A. FURUSAWA:
'Creation, storage, and on-demand release of optical quantum states with a negative Wigner function',
Physical Review X **3**, 041028 (2013).

136 C. T. LEE:
'Measure of the nonclassicality of nonclassical states',
Physical Review A **44**, R2775–R2778 (1991).

137 C. T. LEE:
'Moments of p functions and nonclassical depths of quantum states',
Physical Review A **45**, 6586–6595 (1992).

138 M. G. GENONI, M. L. PALMA, T. TUFARELLI, S. OLIVARES, M. S. KIM, and M. G. A. PARIS:
'Detecting quantum non-Gaussianity via the Wigner function',
Physical Review A **87**, 062104 (2013).

139 B. KÜHN and W. VOGEL:
'Quantum non-Gaussianity and quantification of nonclassicality',
Physical Review A **97**, 053823 (2018).

140 A. PREDOJEVIĆ, S. GRABHER, and G. WEIHS:
'Pulsed Sagnac source of polarization entangled photon pairs',
Optics Express **20**, 25022–25029 (2012).

141 H. JAYAKUMAR, A. PREDOJEVIĆ, T. HUBER, T. KAUTEN, G. S. SOLOMON, and G. WEIHS:
'Deterministic photon pairs and coherent optical control of a single quantum dot',
Physical Review Letters **110**, 135505 (2013).

142 A. DOUSSE, J. SUFFCZYŃSKI, A. BEVERATOS, O. KREBS, A. LEMAÎTRE, I. SAGNES, J. BLOCH, P. VOISIN, and P. SENELLART:
'Ultrabright source of entangled photon pairs',
Nature **466**, 217 (2010).

143 O. GAZZANO, S. MICHAELIS DE VASCONCELLOS, C. ARNOLD, A. NOWAK, E. GALOPIN, I. SAGNES, L. LANCO, A. LEMAÎTRE, and P. SENELLART:
'Bright solid-state sources of indistinguishable single photons',
Nature Communications **4**, 1425 (2013).

144 G. Harder, T. J. Bartley, A. E. Lita, S. W. Nam, T. Gerrits, and C. Silberhorn:
'Single-mode parametric-down-conversion states with 50 photons as a source for mesoscopic quantum optics',
Physical Review Letters **116**, 143601 (2016).

145 M. N. O'Sullivan, K. W. C. Chan, V. Lakshminarayanan, and R. W. Boyd:
'Conditional preparation of states containing a definite number of photons',
Physical Review A **77**, 023804 (2008).

146 J. Laurat, T. Coudreau, N. Treps, A. Maître, and C. Fabre:
'Conditional preparation of a quantum state in the continuous variable regime: generation of a sub-Poissonian state from twin beams',
Physical Review Letters **91**, 213601 (2003).

147 T. S. Iskhakov, V. C. Usenko, U. L. Andersen, R. Filip, M. V. Chekhova, and G. Leuchs:
'Heralded source of bright multi-mode mesoscopic sub-Poissonian light',
Optics Letters **41**, 2149–2152 (2016).

148 K. D. Weston, M. Dyck, P. Tinnefeld, C. Müller, D. P. Herten, and M. Sauer:
'Measuring the number of independent emitters in single-molecule fluorescence images and trajectories using coincident photons',
Analytical Chemistry **74**, 5342–5349 (2002).

149 A. Kurz, J. J. Schmied, K. S. Grußmayer, P. Holzmeister, P. Tinnefeld, and D.-P. Herten:
'Counting fluorescent dye molecules on DNA origami by means of photon statistics',
Small **9**, 4061–4068 (2013).

150 H. Ta, J. Keller, M. Haltmeier, S. K. Saka, J. Schmied, F. Opazo, P. Tinnefeld, A. Munk, and S. W. Hell:
'Mapping molecules in scanning far-field fluorescence nanoscopy',
Nature Communications **6**, 7977 (2015).

151 B. D. Mangum, Y. Ghosh, J. A. Hollingsworth, and H. Htoon:
'Disentangling the effects of clustering and multi-exciton emission in second-order photon correlation experiments',
Optics Express **21**, 7419–7426 (2013).

152 Y. Israel, R. Tenne, D. Oron, and Y. Silberberg:
'Quantum correlation enhanced super-resolution localization microscopy enabled by a fibre bundle camera',
Nature Communications **8**, 14786 (2017).

153 V. C. Usenko, B. Heim, C. Peuntinger, C. Wittmann, C. Marquardt, G. Leuchs, and R. Filip:
'Entanglement of Gaussian states and the applicability to quantum key distribution over fading channels',
New Journal of Physics **14**, 093048 (2012).

154 D. Vasylyev, A. A. Semenov, and W. Vogel:
'Atmospheric quantum channels with weak and strong turbulence',
Physical Review Letters **117**, 090501 (2016).

155 M. Bohmann, R. Kruse, J. Sperling, C. Silberhorn, and W. Vogel:
'Probing free-space quantum channels with laboratory-based experiments',
Physical Review A **95**, 063801 (2017).

156 J. Peřina and L. Mišta:
'Reformulation of the optical equivalence theorem in terms of the Laguerre polynomials',
Annalen der Physik **477**, 372–382 (1969).

157 R. Hošák and M. Ježek:
'Arbitrary digital pulse sequence generator with delay-loop timing',
Review of Scientific Instruments **89**, 045103 (2018).

158 M. Ware, A. Migdall, J. C. Bienfang, and S. V. Polyakov:
'Calibrating photon-counting detectors to high accuracy: background and deadtime issues',
Journal of Modern Optics **54**, 361–372 (2007).

159 A. Allevi and M. Bondani:
'Direct detection of super-thermal photon-number statistics in second-harmonic generation',
Optics Letters **40**, 3089–3092 (2015).